Construction Materials and Engineering

Reinforced Concrete

Design, Performance and Applications

Sharon Robinson
Editor

NOVA

CONSTRUCTION MATERIALS AND ENGINEERING

REINFORCED CONCRETE

DESIGN, PERFORMANCE AND APPLICATIONS

CONSTRUCTION MATERIALS AND ENGINEERING

Additional books in this series can be found on Nova's website under the Series tab.

Additional e-books in this series can be found on Nova's website under the e-books tab.

CONSTRUCTION MATERIALS AND ENGINEERING

REINFORCED CONCRETE

DESIGN, PERFORMANCE AND APPLICATIONS

SHARON ROBINSON
EDITOR

nova science publishers
New York

Library of Congress Cataloging-in-Publication Data

Names: Robinson, Sharon.
Title: Reinforced concrete : design, performance and applications / editor, Sharon Robinson.
Other titles: Reinforced concrete (Nova Science Publishers)
Description: Hauppauge, New York : Nova Science Publishers, Inc., [2017] |
Series: Construction materials and engineering | Includes bibliographical references and index.
Identifiers: LCCN 2016057906 (print) | LCCN 2016058191 (ebook) |
ISBN 9781536107524 (Hardcover) | ISBN 9781536107531 (ebook) | ISBN 9781536107531 (eBook)
Subjects: LCSH: Reinforced concrete--Mechanical properties. | Concrete--Deterioration.
Classification: LCC TA444 .R387 2017 (print) | LCC TA444 (ebook) | DDC 624.1/8341--dc23
LC record available at https://lccn.loc.gov/2016057906

Published by Nova Science Publishers, Inc. † New York

CONTENTS

PREFACE

Concrete is one of the most used materials in the construction industry. In structural systems, the combination of concrete and steel reinforcement bars gives rise to reinforced concrete (RC), which is widely applied in the civil engineering field due to its adequate mechanical strength, durability, and fire resistance. Steel-rebar reinforced structures are subjected to structural deterioration when subjected to extreme loadings such as earthquake, fire, impact loadings and cyclic loading, consequently reducing the expected life and performance of structures. To enhance the structural performance, the RC structures are usually retrofitted or strengthened. This book reviews design, performance and applications of reinforced concrete.

Chapter 1 – Fibre reinforced polymer (FRP) is used extensively nowadays in construction industry to reinforce and strengthen reinforced concrete (RC) structures to enhance the structural performance of the structures under various loading conditions. Finite element analysis is an efficient and accurate method for modelling the structural behavior of FRP strengthened RC structures especially under extreme loadings such as cyclic loading. For accurate numerical modelling of the structural behavior of FRP strengthened RC beams, appropriate material models of each component and bond behavior are essential. In this chapter, the developed materials models for concrete, FRP, steel rebar and adhesive and the bond stress-slip models for FRP/adhesive/concrete interfaces are reviewed. In addition the developed finite element models for analysis of FRP strengthened RC beams under static and cyclic load are also reviewed.

Chapter 2 – The nonlinear behavior of reinforced concrete (RC) structures can be represented using the continuum damage models. The goal of this approach is the description of the processes of mechanical damage and the subsequent implementation in structural analysis programs. In continuum damage models, the damage evaluation is carried out across the entire structural domain, which significantly increases the computational effort. Alternatively, lumped damage mechanics allows for an accurate mechanical modeling of non-linear behavior of concrete without representing damage over the total structural area. This theory combines concepts of fracture mechanics with the plastic hinge idea and it can be used accurately in one-dimensional structural elements. In this chapter, this theory is applied to the mechanical analysis of one RC beam and one RC frame. The results are compared with numerical and experimental responses available in the literature. Good agreement is observed among the results shown in the references and those obtained by the lumped damage model.

Chapter 3 – This study aims the mecano-probabilistic modelling of reinforced concrete structures subjected to reinforcements' corrosion. The corrosion time initiation due to the carbonation or the chloride penetration is assessed by diffusion approaches. The tree of failure is utilized for determining the probability of individual and global failure modes. The structural mechanical resistance is evaluated according to the Brazilian design code NBR 6118/2014. The penalizations over the reinforcements' cross section area and over its yield stress, both caused by the corrosion process, are accounted. The loading is modelled by the extreme value process. Probability of failure curves for the corrosion time initiation; mechanical failure and reinforcements' steel loss along time are presented. In addition to the assessment of the probability of individual failure modes, the progressive collapse paths along 50 years are analysed. The results obtained show that relevant changes on the predominant mechanical failure mode occur along time. Moreover, major values for the reinforcements' steel loss and the probability of mechanical collapse are observed at the end of 50 years, even accounting for the design code recommendations.

Chapter 4 – Studies concerning with atmospheric corrosion of metals have been carried out during many years. Havana City could be considered as one of the zones of higher atmospheric corrosion in the world. In the present chapter, the methodology often used in studies of atmospheric corrosion in metals is applied to study the atmospheric corrosion of steel-reinforced concrete. It is possible to reduce the premature deterioration in the structures in conditions of a coastal city located in a tropical island through the evaluation of the corrosion behavior of different types of concrete and covering thicknesses.

The use of reinforced concrete with water cement ratios 0.5 and 0.6 and covering thicknesses 20 and 40 mm does not assure an adequate durability and useful life for structures submitted to corrosivity categories of the atmospheres very high (C5) and extreme (CX) in a coastal-industrial atmosphere. It is required the use of w/c ratio 0.4 and cover thickness 40 mm to assure an adequate durability.

Chapter 5 – The reinforced concrete structures must beings able to absorb the forces applied to them throughout their lives and support the alterations over time and the environment to which they are exposed. In this context, an experimental study was conducted on a public-use building which has structural disorders using non-destructive testing (NDT). The rebound hammer test, the ultrasonic device and the chemical test are used in the field of non-destructive tests to determine respectively the compression strength, the ultrasonic pulse velocity (UPV) and the rebar corrosion in the concrete. Indeed, the test results were analyzed to identify the different disorders in order to offer adequate compensation method and protection against future attacks. Test results have shown that the concrete exhibits good compressive strength. The steel was completely corroded as a result of a chemical attack. The method of jacketing has been proposed for strengthening of building columns.

In: Reinforced Concrete
Editor: Sharon Robinson
ISBN: 978-1-53610-752-4

Chapter 1

FINITE ELEMENT ANALYSIS OF FIBRE REINFORCED POLYMER STRENGTHENED REINFORCED CONCRETE BEAMS

Prabin Pathak and Y. X. Zhang*
School of Engineering and Information Technology,
University of New South Wales, Canberra,
Australian Defence Force Academy, ACT, Australia

ABSTRACT

Fibre reinforced polymer (FRP) is used extensively nowadays in construction industry to reinforce and strengthen reinforced concrete (RC) structures to enhance the structural performance of the structures under various loading conditions. Finite element analysis is an efficient and accurate method for modelling the structural behavior of FRP strengthened RC structures especially under extreme loadings such as cyclic loading. For accurate numerical modelling of the structural behavior of FRP strengthened RC beams, appropriate material models of each component and bond behavior are essential. In this chapter, the developed materials models for concrete, FRP, steel rebar and adhesive and the bond stress-slip models for FRP/adhesive/concrete interfaces are reviewed. In addition the developed finite element models for analysis of FRP strengthened RC beams under static and cyclic load are also reviewed.

* Corresponding Author Email: y.zhang@adfa.edu.au.

Keywords: bond-slip, cyclic loading, Fibre Reinforced Polymer (FRP), finite element analysis, RC beams

1. INTRODUCTION

Reinforced concrete (RC) structures possess many advantages such as durability and strength, and they have been very widely used globally. Steel-rebar reinforced structures are subjected to structural deterioration when subjected to extreme loadings such as earthquake, fire, impact loadings and cyclic loading, consequently reducing the expected life and performance of structures.

To enhance the structural performance, the RC structures are usually retrofitted or strengthened. In late 1980s and early 1990s, steel plates were often used for the rehabilitation and strengthening of concrete structures. However disadvantages of steel such as tendency to corrode, heavy weights, deterioration of the bonds at their steel-concrete interfaces and the requirement of massive scaffolding during installation (Arockiasamy 1995) made it not so attractive. Since 1990, there has been an increasing interest in the use of high strength composites for repair and rehabilitation of reinforced concrete components. Fibre reinforced Polymers (FRPs) are being used increasingly as promising composite materials for enhancing the RC structures. FRP, a composite material made of a polymer matrix reinforced with fibres, such as glass, carbon, basalt fibres, is of superior characteristics such as high strength to weight ratio, excellent corrosion resistance, excellent fatigue resistance, good durability, and cost effective fabrication (Hollaway and Leeming 1999).

FRP has been used to strengthen RC beams, which is one of the most basic structural elements as well as an indispensable part for most civil constructions. In engineering practice, many RC structures including beams are subjected to dynamic loadings in their service life, such as cycling loading. For example, a typical RC bridge deck system may experience up to 7×10^8 stress cycles during the course of a 120-year life span (Hollaway and Leeming 1999), and an overpass on a typical highway with a design life of 40 years can experience a minimum of 58×10^8 loading cycles of varying amplitude (Ferrier et al. 2011). Under cyclic loading, internal cracking of concrete may occur, which could degrade the stiffness and load-carrying capacity of the structures (Loo 2010). FRP is used in different ways such as externally bonding, wrapping and near surface mounting as per need of the structures. FRP plates or sheets are usually glued to the bottom or tension side of a reinforced concrete beam to increase the flexural strength, whereas FRP plates are normally applied on sides of a reinforced concrete beams to strengthen the RC beam in shear.

A large number of experimental studies have been conducted on the structural flexural behaviour of FRP strengthened RC beams. Although experiment provides the source of reliable data and results, it is usually very time and resource consuming. Finite element method is one of the most powerful numerical methods for analysis of engineering structures, especially for those with complicated geometries, loading and boundary conditions. A large number of numerical analysis of FRP strengthened RC beams have been conducted, with most focusing on the static behaviour with a perfect bond assumption between FRP, adhesive and concrete. However, in practice, the structural performance of FRP strengthened RC beams depends not only on its components such as concrete, steel, FRP and adhesive, but also on the bond behaviour between FRP, adhesive and concrete. The bond between concrete, adhesive and FRP laminates plays a significant role in transferring the stress from the former to the latter, and bond behaviour is the critical aspect for the structural performance of FRP strengthened RC beams (Teng 2015). For an accurate numerical modelling of the structural behavior of FRP strengthened RC beams, appropriate material models of each component and bond behavior are essential.

In this chapter, the developed materials models for concrete, FRP, steel rebar and adhesive and the bond stress-slip models for FRP/adhesive/concrete interfaces are reviewed. In addition the developed finite element models for analysis of FRP strengthened RC beams under static and cyclic load are also reviewed. For accurate finite element analysis of FRP strengthened RC beam under cyclic loading, the material degradation and bond-slip degradations should be considered and these models are also reviewed in this chapter.

2. MATERIAL MODELS

A FRP strengthened RC beam consists of four major components, i.e., concrete, steel, FRP and adhesive, and each of these components has their own unique properties. So, for the accurate modelling of structural behaviour of FRP strengthened RC beams, each of these components should be modelled properly and proper selection of material models are essential. The material models for the concrete, steel, FRP and adhesive are reviewed herein.

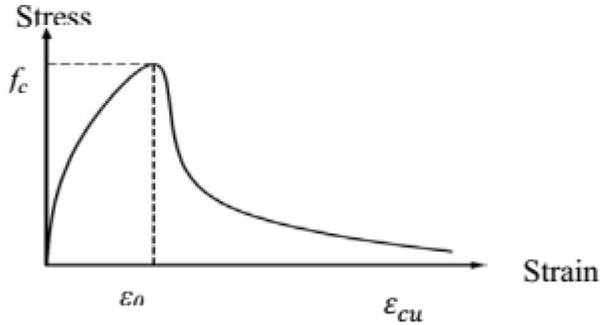

Figure 1. General stress-strain relation of concrete in compression.

Table 1. Concrete compressive models

Model	Equations	Diagram
Desayi and Krishanan (1964)	$\sigma_c = \frac{E_c \varepsilon_c}{1+(\varepsilon_c/\varepsilon_0)^2}$	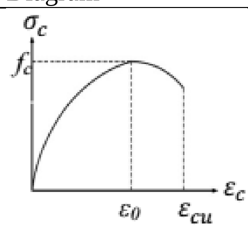
Hognestad (1955); Nitereka and Neal (1999)	For $\varepsilon \le \varepsilon_0$, $\sigma_c = f_c \left[\frac{\varepsilon_c}{\varepsilon_0}\left(2 - \frac{\varepsilon_c}{\varepsilon_0}\right)\right]$ For $\varepsilon_0 \le \varepsilon \le \varepsilon_{cu}$, $\sigma_c = f_c \left[1 - 0.15 \times \left(\frac{\varepsilon_c - \varepsilon_0}{\varepsilon_{cu} - \varepsilon_0}\right)\right]$	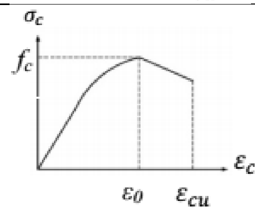
Popovics (1970); Thorenfeldt (1987)	$\sigma_c = \frac{n f_c (\varepsilon_c/\varepsilon_0)}{n-1+(\varepsilon_c/\varepsilon_0)^{nk}}$ $n = 0.8 + f_c/17$ For $1 < \varepsilon_c/\varepsilon_0 \le \varepsilon_{cu}$, $k = (0.67 + \frac{f_c}{62})$ For $\varepsilon_c/\varepsilon_0 \le 1$, $k = 1$	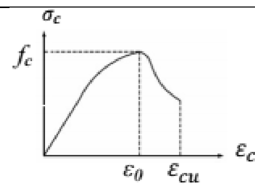

2.1. Material Models for Concrete

Concrete is a quasi-brittle material, which is strong in compression and generally weak in tension. For the numerical modelling of concrete, the material models in compression and tension are both essential. Many models have been developed for the stress-strain relationship of concrete.

2.1.1. Concrete Compression Model

Concrete compression material model is the relationship between compressive stress and strain developed in concrete. A typical curve is shown in Figure 1. The stress–strain relationship of concrete in compression is comprised of an ascending and a gradual descending branch, which is termed as softening branch. In general, the stress-strain relation of concrete under compression remains linear till 30% of the compressive strength after which the curve becomes nonlinear followed by softening of concrete until the ultimate strain (Bangash 1989). Several compression models for concrete have been developed and a few of the popular models are listed in Table 1.

2.1.2. Concrete Tension Model

Generally, the stress-stress relation of concrete under tension is assumed to be isotropic and linearly elastic up to the tensile strength after which crack occurs and stress gradually reduces to zero as shown in Figure 2. Tension stiffening in RC concrete members is usually caused by the increase in stiffness of a cracked member due to the development of tensile stresses in the concrete between the cracks. Concrete does not crack suddenly and completely but undergoes progressive micro-cracking and the intact concrete between neighbouring cracks carries considerable tensile force (Teng 2013). After cracking, tension stiffening effects becomes significant and should be included in the analysis. A few developed stress-strain relation of concrete in tension with tension stiffening effect is shown in Table 2.

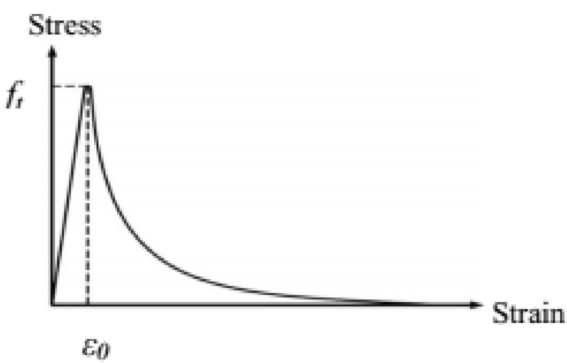

Figure 2. General stress-strain behaviour of concrete in tension.

Table 2. Different stress-strain relations of concrete in tension

Concrete tension model	Equations	Diagram
Izumo et al. (1992)	For $(\varepsilon_0 \le \varepsilon_t \le 2\varepsilon_0)$, $\sigma_t = f_t$ For $(\varepsilon_t \ge 2\varepsilon_0)$, $\sigma_t = (2\varepsilon_0/\varepsilon_t)^{0.04}$	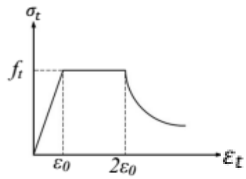
Nour et al. (2007)	For $0 \le \varepsilon_t \le \varepsilon_0$, $\sigma_t = E_C\varepsilon$ For $\varepsilon_0 \le \varepsilon_t \le \varepsilon_1$, $\sigma_t = f_t[1-(1-\beta)\frac{\varepsilon}{\varepsilon_1}]$ For $\varepsilon_1 \le \varepsilon_t \le \varepsilon_2$, $\sigma_t = \beta f_t$ For $\varepsilon_2 \le \varepsilon_t \le \varepsilon_{bar,y}$, $\sigma_t = \beta f_t(\frac{\varepsilon_{bar,y}-\varepsilon}{\varepsilon_{bar,y}-\varepsilon_2})$ where β is the tension-stiffening factor, $\varepsilon_{bar,y}$ is yield strain of steel	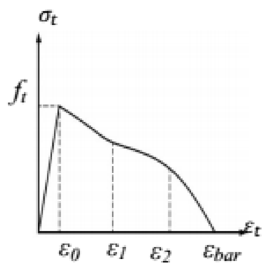
ANSYS (2013)	*Tc* is the multiplier for the amount of tensile stress relaxation.	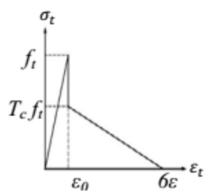

2.2. Material Models for Steel

A typical stress-strain relationship for steel is shown in Figure 3. Steel generally exhibits a linear stress-strain relationship up to a well-defined yield stress. Beyond the yield point, as deformation continues the stress increases due to strain hardening until it reaches the ultimate tensile strength. At the ultimate tensile stress, the neck forms, and tensile strength decreases. Beyond the maximum tensile strain, the steel fractures and ultimately fails with the loss of load capacity. For general engineering practice, the elastic-plastic model is usually used with or without use of strain hardening (Supaviriyakit et al. 2004).

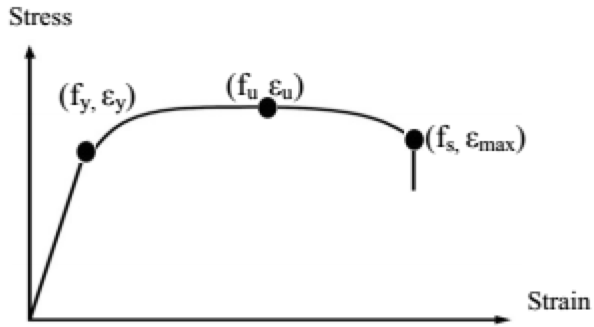

Figure 3. A typical tensile stress-strain curve for reinforcing steel rebar.

Three techniques are usually employed to model steel reinforcement in reinforced concrete structures, i.e., the discrete model, the embedded model, and the smeared model (Tavarez 2001). In the discrete model (Figure 4(a)), the reinforcement is modelled using bar or beam elements which are connected to concrete mesh nodes. Concrete and steel occupy the same region, and the concrete and steel reinforcement mesh share the same nodes. In the embedded model (Figure 4(b)), the stiffness of the reinforcing steel is evaluated separately from the concrete elements. In this model, the reinforcing steel displacements remain compatible with that of the surrounding concrete elements. For a complex modelling, this model is good, however this model also increases the number of nodes and degrees of freedom, making it cost and time inefficient. In the smeared model (Figure 4(c)), the reinforcement is uniformly distributed over concrete elements in a specific region of the finite element mesh. This type of model is useful in large scale model where reinforcement does not significantly contribute to the response of structure.

2.3. Material Model for FRPs

FRP composites are light-weight linearly elastic materials formed by embedding continuous fibres in a resin matrix. The fibres are the main load-carrying components while the matrix binds the fibres together. Though the fibres are the main load carrying component of the FRP composite, the binding resin matrix has equally important function. It actually aligns the fibres in a prescribed geometrical arrangement, and helps to transfer the force among the fibres. It also helps to prevent buckling of fibres under compressive action, and protects it from environmental agents.

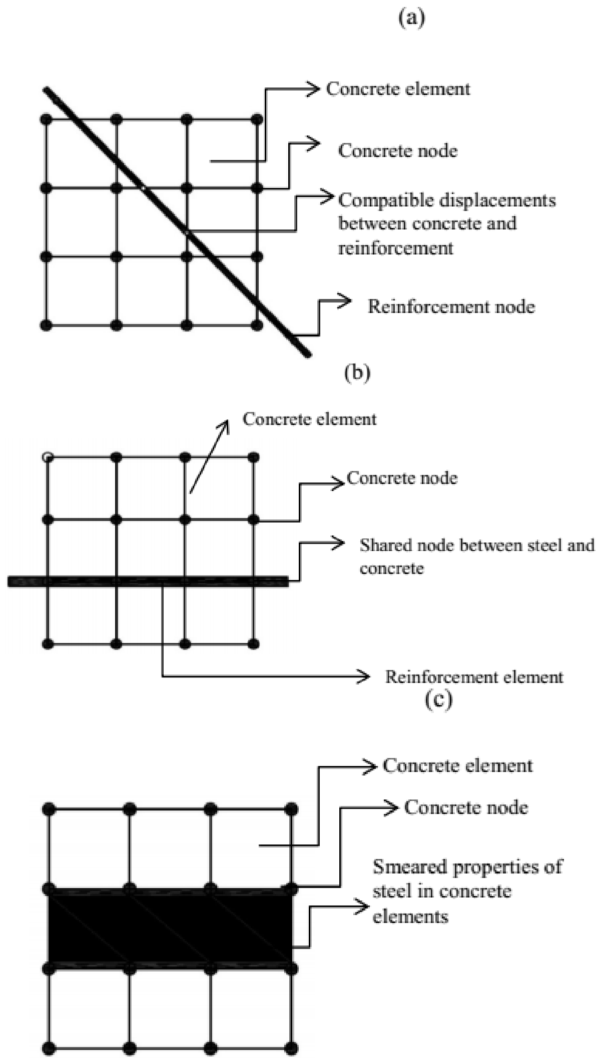

Figure 4. Modelling reinforcement in reinforced concrete (Tavarez 2001): (a) discrete model; (b) embedded model; and (c) smeared model.

The fibres may be made of carbon, glass or aramid while commonly used polymer based resins are epoxy resins, unsaturated polyester resins and vinylester resins. Carbon fibers are conductive, have an excellent combination of high modulus and high tensile strength, and offer good resistance to high temperatures. Glass fibres have got a lower stiffness with a lower cost. Aramid fibres have got the structural and mechanical properties in-between of carbon and glass fibres (Piggott 2002). Glass fibre reinforced polymer (GFRP) is durable in harsh environments and also light in weight. It has a high tensile strength but it is weak in shear, and it can have problems in alkaline environments, such as concrete. Aramid fibre reinforced polymer (AFRP) is less used than the other two types. It has high resistance against heat, but it is usually weak against moisture and ultraviolet radiation, and painting and coating are usually needed to protect AFRP against ultraviolet radiation (Minouei 2011).

The properties of different types of FRPs are presented in Table 3. The stress-strain relation of FRP is normally regarded as linear until it reaches the maximum tensile strength, after which it ruptures, and strength immediately reduces to zero. Figure 5 shows a typical stress-strain relationship of a FRP. An isotropic linear elastic model is usually used to model FRPs (Camata et al. 2007).

Table 3. Typical material parameter for materials used in retrofitting (Prince 2011)

Material	Tensile Strength(MPa)	Modulus of elasticity (GPa)
CFRP	1720-3690	120-580
AFRP	1720-2540	41-125
GFRP	480-1600	35-80
Steel	--	190-210

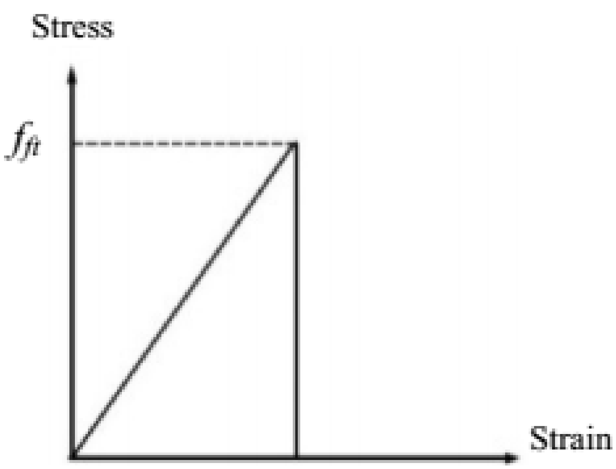

Figure 5. A typical stress-strain relation of a FRP.

2.4. Material Model for Adhesives

Generally an adhesive needs to be used to bind two different or same materials to avoid their separation. The use of adhesives offers many advantages over other binding techniques such as sewing, mechanical fastening, and thermal bonding. These include good ability to bind different materials together and to distribute stress more efficiently across the joint, cost effectiveness for an easily mechanized process, improvement in aesthetic design, and increased design flexibility (Kinloch 1987).

The most common adhesives for structural application between FRP and concrete are epoxy, acrylic and urethane. Epoxy provides very high bond strength with high temperature resistance, whereas acrylic has moderate temperature resistance with strength and rapid curing. The stress-strain relation of an adhesive is generally regarded as linearly elastic. A typical stress-strain relationship is shown in Figure 6.

3. MATERIAL MODELS UNDER CYCLIC LOADING

Generally, fatigue is considered as a distinctive behaviour of materials under cyclic loading. During application of cyclic loading, the first symptom of fatigue failure is micro-cracking, which is ultimately followed by fracture. Normally under cyclic load, the structure fails when the peak stress is considerably low compared to that under static load.

The number of loading cycles causing failure of a component is regarded as fatigue life. For analysis of FRP strengthened RC beams under cyclic loading, it is very essential to consider the effect of cyclic load on the concrete, steel, FRP and the interfacial behavior. Hence it is necessary to discuss the degradation of the material properties of these components under cyclic load.

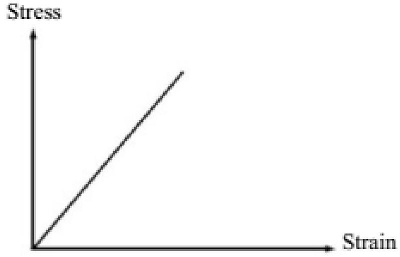

Figure 6. Stress-strain relation of an adhesive.

3.1. Concrete

Concrete is a heterogeneous material which is inherently full of flaws such as pores and air voids. The properties of concrete under cyclic load are a function of the accumulation of irreversible energy deformation, which manifests itself as inelastic strains in the form of cracks and creep (Loo 2010). Under cyclic loads, the strain of concrete increases significantly beyond the value observed after the first load cycle, which is similar to the behaviour of concrete under sustained stress. The fatigue strength of a typical concrete member corresponding to a life of ten million cycles is about 55 percent of the initial static strength of the member. This behaviour of concrete depends on the factors such as range of load, rate and frequency of loading, loading eccentricity, history, material properties and environmental conditions (ACI Committee 215, 1974). The softening of concrete in its stress-strain behaviour under cyclic load causes the slope of stress-strain curve to change as the number of cycles increases.

A number of investigators reported that concrete specimens under cyclic compressive loadings received progressive changes within their concrete matrix due to growth of micro cracking. Generally, the failure in concrete includes three processes: crack initiation, propagation and failure. The first stage occurs in the weak region of the concrete or mortar and it is termed as flaw initiation. The second stage is characterised by slow and progressive growth of the inherent flaws to a critical size and is generally known as micro cracking. In the final stage, when a sufficient number of unstable cracks are formed, a continuous or macro crack will develop, eventually leading to failure. In the first stage, the degradation rate is high but decreasing, the second stage (the longest stage) is characterized by a constant rate, and finally the degradation grows very quickly until failure is reached in the third stage.

Some experimental studies on concrete under cyclic loads (Dillman et al. 1981, Ople et al. 1966) indicated that with the increase in the number of loading cycles, stress redistribution occurred. Stress redistribution is the process of stress transfer from the most initially damaged compression zone to less fatigued areas while permanent and total strains are growing.

Various stress-strain relationship of concrete under cyclic loads has been developed and they are summarised as follows.

Holmen et al.'s Model (1982)

Holmen et al. (1982) proposed that the total maximum strain at any time and at any number of cycles was the sum of the two components as given in

Equation (1). The strain component ε_e is related to the endurance of the specimen, and the creep strain ε_t is a function of the loading time.

$$\varepsilon_{max} = \varepsilon_e + \varepsilon_t \tag{1}$$

It was observed from the tests that strain development followed three distinct phases: a rapid increase from 0 to about 10% of that at the total fatigue life, a uniform increase from 10% to about 80%, and a rapid increase until failure. Holmen et al. (1982) proposed the following equations to describe the first and second phases.

For $0.0 \leq \frac{N}{N_f} \leq 0.1$,

$$\varepsilon_{max} = \frac{1}{E_{sec}}[S_{max} + 3.18(1.183 - S_{max})\left(\frac{N}{N_f}\right)^{0.5}] + 0.413 * 10^{-3}{S_C}^{1.184}\ln(t+1) \tag{2}$$

For $0.1 \leq \frac{N}{N_f} \leq 0.8$,

$$\varepsilon_{max} = \frac{1.11}{E_{sec}}[1 + 0.677\left(\frac{N}{N_f}\right)^{0.5}] + 0.413 * 10^{-3}{S_C}^{1.184}\ln(t+1) \tag{3}$$

$$RMS = \frac{(S_{min}+S_{max})^{0.5}}{8} \tag{4}$$

where ε_{max} is the maximum strain; E_{sec} is the secant modulus at the first cycle; S_{max} is the ratio of maximum stress to concrete strength; S_C is the characteristic stress level and is given as S_m+ RMS, in which S_m is the mean stress ratio and is equal to $0.5(S_{max} + S_{min})$; $S_{min}$is the ratio of minimum stress to concrete strength, and N is the number of load cycles; N_f is the number of load cycles to failure for a specified probability of failure; t is the duration of the alternating load (in hours); *RMS* is the root mean square value of the stress ratio.

Balaguru and Shah's Model (1982)

According to Balaguru and Shah (1982), the cyclic creep strain of concrete can be expressed as the sum of a mean strain component and a cyclic strain component as shown in Equation (5)-(7).

$$\varepsilon_c = 129\sigma_m t^{\frac{1}{3}} + 17.8\sigma_m \Delta N^{\frac{1}{3}} \tag{5}$$

$$\sigma_m = \frac{\sigma_{max}+\sigma_{min}}{2f_c} \tag{6}$$

$$\Delta = \frac{\sigma_{max}-\sigma_{min}}{f_c} \tag{7}$$

in which ε_c is the cyclic creep strain of concrete, σ_m is the mean stress ratio, Δ is the stress range, N is the number of cycles, t is the loading time, σ_{max} and σ_{min} is the maximum and minimum applied stress, respectively, and f_c is compressive strength of concrete.

Zanuy et al.'s Model (2009)

Zanuy et al. (2009) proposed the following equations to evaluate the maximum strain of the concrete, which also includes stress redistribution in concrete under constant amplitude cyclic loading for the material behaviour of the concrete under cyclic loading.

For $0.0 \le \frac{N}{N_f} \le 0.1$,

$$\frac{\varepsilon_{max}}{\varepsilon_0} = 1 + A\frac{N}{N_f} + B(\frac{N}{N_f})^2 \tag{8}$$

For $0.1 \le \frac{N}{N_f} \le 0.8$

$$\frac{\varepsilon_{max}}{\varepsilon_0} = \varepsilon_{1-2} + \varepsilon_2(\frac{N}{N_f} - 0.1) \tag{9}$$

For $0.8 \le \frac{N}{N_f} < 1$

$$\frac{\varepsilon_{max}}{\varepsilon_0} = \varepsilon_{1-2} + \varepsilon_2(\frac{N}{N_f} - 0.1) + C(\frac{N}{N_f} - 0.8)^2 \tag{10}$$

where N is the number of cycles, N_f is the number of cycles at failure, ε_0 is the initial strain at the first load cycle (N = 1), and

$$A = 20(\varepsilon_{1-2} - 1) - \varepsilon_2 \tag{11}$$

$$B = 100(1 - \varepsilon_{1-2}) + 10\varepsilon_2 \tag{12}$$

$$C = 25\left(\frac{\varepsilon_{fail}}{\varepsilon_0} - \varepsilon_{1-2} - 0.9\varepsilon_2\right) \tag{13}$$

$$\varepsilon_{1-2} = \frac{1.184}{S_{max}} \tag{14}$$

$$\varepsilon_2 = \frac{0.74037}{S_{max}} \tag{15}$$

$$\varepsilon_2 \leq \frac{1}{0.9}\left(\frac{\varepsilon_{fail}}{\varepsilon_0} - \varepsilon_{1-2}\right) \tag{16}$$

where S_{max} is the ratio of maximum stress to concrete strength, N_f is the failure number of cycles, and ε_{fail} is the strain at N_f.

3.2. Steel

Many experiments have been conducted to understand the behaviour of steel under cyclic load, which is either embedded in concrete or tested in air. Crack propagation takes place with number of cycles of load to some critical size, a size at which the remaining uncracked cross section of the part becomes too weak to carry the imposed loads, eventually causing sudden fracture of the remaining cross-section. Crack initiation typically occurs at a location of the largest stress concentration, usually at the intersection of transvers and longitudinal reinforcement (Papakonstantinou et al. 2001). In addition to the material properties and loads, the analysis of steel under cyclic load must take into consideration the type of applied loading (uniaxial, bending, or torsional), loading pattern (either periodic loading at a constant or variable amplitude or random loading), magnitude of peak stresses, overall size of the part, fabrication method, surface roughness, presence of fretting or corroded surface, operating temperature and environment, and occurrence of service-induced imperfections (Boardman 1990). A few material models for steel under cyclic load are reviewed as follows.

Muralidharan and Manson's Model (1988)

This is a strain-based approach, which includes elastic and inelastic behaviour of steel under cyclic load. It includes the relationship of ultimate tensile strength, fatigue limit, ductility, and fatigue strength coefficient. In this model, the influence of ductility in elastic strain component is considered as negligible. However the level of plastic strain component is strongly influenced by the ratio of ultimate tensile strength to elastic modulus, and hence includes an extra ductility term in plastic strain component.

$$\varepsilon_{sn} = 0.623(\frac{f_y}{E_s})^{0.832}(2N_f)^{-0.09} + 0.0196(\varepsilon_{su})^{0.155}(\frac{f_y}{E_s})^{-0.53}(2N_f)^{-0.56} \quad (17)$$

where ε_{sn} is the steel's strain, f_y is the yielding stress, E_s is Young's modulus, N_f the number of loading cycles, and ε_{su} is the ultimate strain of the steel.

CEB -FIP-Model (1993)

According to the CEB-FIP-Model, the failure cycle N_f of a reinforcing steel bar under a constant amplitude loading can be expressed as follow.

For $\Delta\sigma \leq \Delta\sigma_{N^*}$,

$$\log N_f = \log(N^*) + k_1(log\Delta\sigma - log\Delta\sigma_{N^*}) \quad (18)$$

For $\Delta\sigma \geq \Delta\sigma_{N^*}$,

$$\log N_f = \log(N^*) + k_2(log\Delta\sigma_{N^*} - log\Delta\sigma) \quad (19)$$

where $\Delta\sigma$ is the stress range in the steel, $\Delta\sigma_{N^*}$ is the stress range at N^* cycles and k_1And k_2 are the stress exponents.

Mander et al.'s Model (1994)

Mander et al. (1994) proposed a model for steel under cyclic load with variation in Coffin-Manson relationship which includes elastic and plastic strain components.

$$\varepsilon_{sn} = \frac{f_y}{E_s} \times (2N_f)^b + \varepsilon_{su} \times (2N_f)^c \quad (20)$$

where ε_{sn} is the steel's strain, f_y *is* yielding stress, E_s Young's modulus, N_f is the number of loading cycles, *b* and *c* are -0.14 and -0.5, respectively, and ε_{su} is the ultimate strain of the steel.

3.3. FRPs

The failure mechanism of FRPs under cyclic load is more complicated than that of plain concrete or steel. With each load cycle, cracks are formed by fatigue at the weak points and then grow progressively. Composite materials often have a much greater fatigue life than other homogenous materials (Papakonstantinou et al. 2001). If an individual fibre within an FRP composite develops a defect, this defect will not propagate across to other fibres, reducing the extent to which cracks can grow. Once the FRP composite is damaged, the damage propagates along the matrix between unidirectional fibres and does not pass through adjacent fibres (Kim and Heffernan, 2008). According to Adimi et al. (2000), the failure of FRP composite is the combination of different degradation mechanisms including matrix cracking, fibre breakage, fibre-matrix debonding and delamination. Even if the surface fibres fail under cyclic load, the remaining fibres continue to support the redistributed load and this behaviour continues until total failure occurs. Some available models for FRP under cyclic loading are given below.

Adimi et al.'s Model (2000)

$$log\sigma_{max} = 3.43 - 0.0674 \log N \tag{21}$$

where σ_{max} = maximum tensile stress (MPa); N = number of cycles to failure.

Ferrier et al.'s Model (2011)

$$E_{fn} = m - n \times \log(N) \tag{22}$$

where m (in N/mm^3) is the Young's modulus under static loading, n is 1100, E_{fn} is Young's modulus of FRP after N number of cycles of loading.

4. BOND BEHAVIOR

Many experimental studies on FRP strengthened RC beams demonstrated that debonding was one of the most critical failure modes. Thus it is important to consider the compliance of the bond between concrete, adhesive and FRP in numerical modelling.

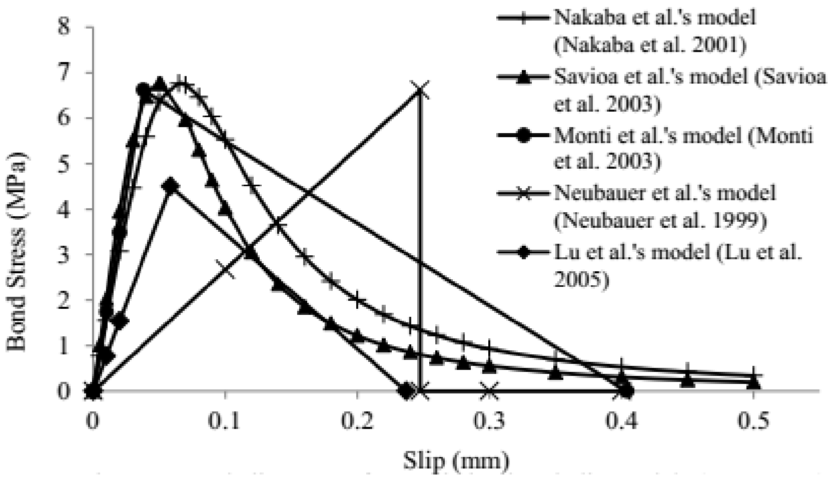

Figure 7. Bond-slip curves from existing bond-slip models (Teng 2013).

Table 4. Different bond-slip models

Bond-slip model	Ascending branch	Descending branch	τmax	S_0	S_f	β_w	Graph
Neubauer and Rostasy (1999)	$\tau_{max}(\frac{s}{s_0})$	0	$1.8\beta_w f_t$	$0.202 \times \beta_w$		$\sqrt{1.125\frac{2-\frac{b_f}{b_c}}{1+\frac{b_f}{400}}}$	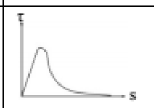
Nakaba et al. (2001)	$\tau_{max}\left(\frac{s}{s_0}\right)[3/(2+(\frac{s}{s_0})^3)]$		$3.5{f_c}^{0.19}$	0.065			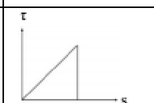
Monti et al. (2003)	$\tau_{max}\left(\frac{s}{s_0}\right)$	$\tau_{max}\left(\frac{s_f-s}{s_f-s_0}\right)$	$1.8\beta_w f_t$	$2.5\tau_{max}(\frac{t_a}{E_a}+\frac{50}{E_c})$	$0.33\beta_w$	$\sqrt{1.5\frac{2-\frac{b_f}{b_c}}{1+\frac{b_f}{100}}}$	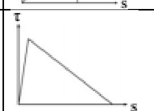
Savioa et al. (2003)	$\tau_{max}\left(\frac{s}{s_0}\right)[2.86/(1.86(\frac{s}{s_0})^{2.86})]$		$3.5{f_c}^{0.19}$	0.051			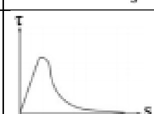
Lu et al. (2005)	$\tau_{max}(\frac{s}{s_0})$	$\tau_{max}\left(\frac{s_f-s}{s_f-s_0}\right)$	$1.5\beta_w f_t$	$0.0195\beta_w f_t$	$2\frac{G_f}{\tau_{max}}$	$\sqrt{\frac{2.25-\frac{b_f}{b_c}}{1.25+\frac{b_f}{b_c}}}$	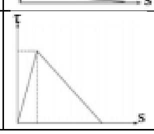

where τ is the local bond stress, τ_{max} is the maximum local bond stress, s is a local slip, s_0 is a local slip at τ_{max}, s_f is a local slip when bond stress τ reduces to zero, G_f is the interfacial fracture energy, β_w is width ratio factor, f_t is concrete tensile strength, b_f is the width of FRP plate, and b_c is the width of the concrete.

4.1. Bond-Slip Models under Static Loading

A bond stress-slip model is used to describe the interfacial behaviour as a relationship between the local shear stress (τ) and relative displacement (s) between concrete/ adhesive/FRP interfaces. Despite the difficulty in obtaining local bond-slip curves from tests directly, local bond-slip models for FRP/ adhesive/concrete interfaces have been developed based on strain measurements or load-slip curves (Lu et al. 2005). A few bond stress-slip relationships have been proposed and employed in finite element analysis of FRP strengthened RC beams. Different bond stress-slip models and the relationship between bond stress and slip reported in literatures are discussed below.

Neubauers and Rostasy's model (1999) is a linear-brittle model which is very different from other available models. The fact that the bond stress reduces to zero at the ultimate slip dictates that there exists an effective bond length beyond which an increase in the bond length will not increase the ultimate load. Other models (Nakaba et al. 2001, Savoia et al. 2003, Monti et al. 2003, and Lu et al. 2005) have indicated that the bond-slip curve should comprise of both an ascending and descending branch. The models of Nakaba et al. (2001) and Savioa et al. (2003) are quite similar and consist of nonlinear ascending and descending curves while those of Monti et al. (2003) and Lu et al. (2005) are bilinear. The maximum bond stress, slip at the maximum stress and ultimate slip at zero bond stress are the key parameters, which play significant roles in bond stress-slip relationship. It is found that the maximum bond stress and interfacial fracture energy (area under bond-slip curve) of each of the models of Nakaba et al (2001), Savioa et al. (2003) and Monti et al. (2003) are larger than the value predicted by Lu et al. (2005). Different bond-slip models are presented in Table 4. A comparison between these models is shown in Figure 7.

4.2. Bond-Slip Models under Cyclic Loading

Several cyclic loading tests were conducted to study FRP/adhesive/ concrete bonded interface and it was found that the interface debonding propagated progressively with the increase of fatigue cycles (Bizindavyi et al. 2003, Tan et al. 2003).

Test methods used to evaluate the bonding behaviour of externally-bonded FRP composite sheets and plates under cyclic loading include the single shear test (single lap joint) (Bizindavyi et al. 2003, Mazzotti and Savoia 2009), double lap joint test (Ferrier et al. 2005), pull-out specimen method for measuring peeling stresses (Khan et al. 2011) and the partially bonded beam test (Gheorghiu et al. 2004). Under fatigue loading, there are normally three distinct phases for the FRP/adhesive/concrete bonded joints. In the first phase, the bond mainly sustains damage in the form of micro cracks that cause residual plastic strain with negligible stiffness degradation. During second phase, the joint retains its load resisting ability, though macro cracks cause degradation of stiffness. In the third stage, when joint loses its stiffness and load resisting capacity, the debonding and fracture occur (Mahal 2015). It is clear that the bond stress degrades with number of cycles, and this affects the structural behaviour of the FRP strengthened RC beams. In the following, the bond-slip models under cyclic loading are reviewed.

Bizindavyi et al. (2003) investigated the behaviour of FRP/adhesive/ concrete joints of FRP strengthened RC beams under cyclic loading using the single lap joint test method. The test was set in such way that the progression of crack propagation during shear tests could be visualized. It was found that in the first and last quarter portions of the bonded joints, cracks propagated into the concrete core, while a cohesive debonding at the interface between the concrete and the adhesive or between the FRP and adhesive occurred in the central region of the joint. From the test, fatigue life curves were obtained and described by Equation (23)

$$\ln(\Delta\tau_{ave}) = a - cln(N_f) \tag{23}$$

where $\Delta\tau_{ave}$ is the cyclic mean bond stress range, N_f is the number of cycles to failure, and a and c are constants ranging from 0.08 to 1.06 and 0.041 to 0.095, respectively.

It was found that as the number of loading cycles increased, the FRP/ adhesive/concrete bond slip increased. Also, the higher the applied cyclic stress, the greater the slip and the shorter the fatigue life of the bonded joint.

Ferrier et al. (2005) conducted experiment using the double-lap shear test method to understand the fatigue behaviour of the adhesive layer between concrete and FRP. In this test, two concrete blocks, attached by two parallel composites strips separated by 20 mm, were applied with tensile load. An alternate load was applied with frequency of 1 Hz. The test suggested a linear relation between the maximum strength ($\Delta\tau_{adh}$) of concrete/adhesive/FRP interface and the logarithm of the number N of load cycles to failure. The linear relation is given by Equation (24).

$$\Delta\tau_{adh} = mlog(N) + b \tag{24}$$

where m = -0.07 and b=0.98

Parameters m and b are fitted with experimental data. The $\Delta\tau_{adh}$ - N curve revealed that the shear stress should be limited to 0.80 MPa to have a fatigue life of 10 million cycles at 1 Hz frequency.

Loo et al. (2012) calculated the fatigue life from the point where the slip (s_{max}) that is associated with the bond stress at the maximum cyclic load ($\tau_{ave,max}$) for a given cycle N. When this maximum slip equals the slip obtained from a static bond-slip test at the stress of $\tau_{ave,max}$, failure occurs. A model similar to that developed by Holmen (1982) for concrete in compression may be used to describe the fatigue response of FRP-to-concrete bond. Based on a regression analysis of Dai et al.'s (2005) and Yun et al.'s (2008), the following relationships were proposed:

$$s_{max} = \frac{\tau_{ave,max}}{E_{b0}}[1 + a(logN)^{b}.\left(\frac{\Delta\tau_{ave}}{\Delta\tau_{ave,f}}\right)^{c}] \tag{25}$$

$$E_b = E_{b0}[1 + \alpha(logN)^{\beta}.\left(\frac{\Delta\tau_{ave}}{\Delta\tau_{ave,f}}\right)^{\gamma} \tag{26}$$

where s_{max} is the slip (in mm) at the maximum applied average bond stress ($\tau_{ave,max}$); E_b is the modulus (in N/mm^3) at cycle N; $E_{b0}$is the modulus (in N/mm^3) at the first cycle; N_f is the number of cycles at failure; $\Delta\tau_{ave}$ is the average bond stress range; $\Delta\tau_{ave,f}$ is the average bond stress at failure; and the constants a to c and α to γ are the parameters to fit the experimental data.

4.3. Finite Element Modelling of Bond-Slip for FRP Strengthened RC Structures

Most of the developed finite element models for modelling of FRP strengthened RC structures with bond-slip neglected the adhesive component in the FRP strengthened RC structures, and considered the bond-slip between FRP and concrete interface. However, among different types of debonding failure, cohesive failure in concrete, adhesion failure at the concrete/adhesive interfaces and FRP/adhesive interfaces dominate (Holmer (2009)). Hence to analyse the bond-slip behaviour of FRP strengthened RC beams accurately, the bond-slip behaviour between concrete/adhesive interface and between adhesive/FRP interface should be included with proper bond-slip law.

Two approaches are generally used in modelling the debonding failures in FRP strengthened RC structures. One approach is to employ a layer of interface elements between the FRP, adhesive and the concrete (Wong et al. 2003, Wu et al. 2003) and debonding is simulated as the failure of the interface elements. The success of such an approach depends on the constitutive law (i.e., the bond-slip model) specified for the interface elements. In the second approach, the use of interface elements is avoided, and instead, debonding is directly simulated by modelling the cracking and failure of concrete elements adjacent to the adhesive layer. This is referred to as mesoscale analysis (Lu et al. 2004, Pham et al. 2007). It requires a very fine mesh for the interface between the concrete and adhesive, with an element size smaller than the thickness of the concrete layer (Lu et al. 2004). Recent work on the modelling of debonding failures using the second approach has shown that it is difficult to simulate debonding using the concrete constitutive models available in commonly used general-purpose FE software package such as ANSYS, MSC.MARC or ABAQUS (Teng 2013).

Generally, two types of interface elements have been used to model the interface between FRP, adhesive and concrete, including link element such as spring element and 1D contact element. For the bonding model of concrete/ adhesive interface, the concrete must be double nodded, and one set of nodes is used for the concrete elements, while the other is used for the adhesive. In adhesive-FRP interface, another set of nodes of adhesive element is used for the FRP. The nodes of these two interfaces are connected by bond elements that allow relative displacement, i.e., slip, to take place between concrete, adhesive and FRP. As a link element doesn’t have its own physical dimension, the two connected nodes have the same spatial coordinates. An alternative is the use of contact element as that developed by Goodman et al. (1968), and further developed by Hoshino and Schafer (Keuser and Mehlhorn 1987), which provided the continuous connection between two adjoining elements. It is an isoparametric element which in its deformed state has no dimension in the transverse direction. The simplest form has two double nodes and is based on a linear displacement function. In each pair of double nodes, one node is connected to a concrete element while the other is connected to the adhesive element, or one node is connected to an adhesive element while the other is connected to the FRP element. In the unloaded stage, the coordinates of the nodes at each end of the contact element are identical. Once loading begins, the nodes behave independently, resulting in a relative displacement between the two connected points (Wong et al 2003).

5. NONLINEAR FINITE ELEMENT ANALYSIS OF RC BEAMS UNDER STATIC LOADING

5.1. Nonlinear Finite Element Analysis of RC Beams under Static Load with Perfect Bond Assumption

Abundant amount of researches have been conducted on finite element analysis of FRP strengthened RC beams subjected to static load without considering bond slip between FRP, adhesive and concrete. For example, Hashemi et al. (2007) conducted finite element analysis of CFRP strengthened RC beams under four-point loading using ANSYS. The concrete, steel reinforcement and FRP were modelled using SOLID65 element, LINK8 element and SOLID45 element respectively. Steel reinforcement and CFRP were modelled using elastic-perfectly plastic model and a linear model up to the failure respectively. The concrete in compression was modelled as a linearly elastic-perfectly plastic material, and tension was modelled as linearly elastic until the maximum tensile strength after which strength gradually reduced to zero. Sundarraja et al. (2008) analysed the structural behaviour of GFRP strengthened RC beam under four-point loading using ANSYS. In the modelling, the concrete was modelled using the Desayi and Krishanan’s (1964) material model for compression and linear elastic model until crack for tension with strength gradually reducing to zero after cracking. For steel reinforcement the elastic- perfectly plastic material model was used. Hu et al. (2004) conducted finite element analysis using ABAQUS to predict the ultimate loading capacity of reinforced concrete beams strengthened by CFRP under uniformly distributed load. The stress-strain curve for concrete under compression was based on Saenz’s (1964) model, whereas under tension, the relation was assumed to be linear until it reached the maximum tensile strength after which it reduced gradually to zero. Steel was assumed to be elastic-perfectly plastic. The stress-strain relation of FRP was based on Hahn and Tsau (1973). The reinforced concrete was modelled using 8-node solid elements with three degrees of freedom per node where reinforcement was smeared throughout the element section. FRP was modelled using a four-node shell element assuming perfect bond with concrete.

5.2. Nonlinear Finite Element Analysis of FRP Strengthened RC Beams with Bond Slip under Static Load

Three-dimensional models can capture failure modes which are not available for two dimensional elements such as spalling and anchorage failure in support regions (Ingason 2013, Baky et al. 2007). For accurate prediction of local deformation and fracturing process of concrete, a three-dimensional finite element model is essential (Imperatore et al. 2012). The developed finite element models with bond-slip are categorized broadly as two-dimensional and three dimensional finite element models.

5.2.1. Two Dimensional Finite Element Models

Wong et al. (2003) conducted finite element analysis of RC beams strengthened with externally bonded CFRP subjected to three-point loading. The analysis was based on the Modified Compression Field Theory proposed by Vecchio and Collinns (1986), and the constitutive relation given by Vecchio (1989, 1990). Steel reinforcement was assumed to be elastic-plastic with strain hardening effects, whereas FRP was assumed to be linearly elastic with brittle fraction in tension. The bond stress-slip relationship between concrete and FRP was based on the elastic-plastic models of Homam et al. (2000) and a one-dimensional contact element was used to model the interface between concrete and FRP. FRP was modelled using the truss element. It was found that the linear elastic bond law was appropriate only when failure was dominated by a sudden delamination of FRP plate for a low strength of epoxy, and that for stronger epoxies, elastic-plastic bond slip model was appropriate when failure was due to peeling of concrete cover. Wu et al. (2005) used DIANA for the finite element analysis of debonding mechanisms of RC beams strengthened with CFRP composites under three-point loading. Concrete, steel reinforcement, FRP were modelled by the Drucker-Prager plasticity model, elastic–perfectly plastic model, and linearly elastic model respectively. For concrete cracking, the discrete crack model was used, and FRP/concrete bond was based on Niu and Wu’s model (2001). Concrete was modelled by four-node plane stress elements, whereas reinforcing bars and the FRP sheets were modelled by two-node linear truss elements. The FRP/concrete bond was modelled by zero-thickness interface elements. Stirrups and adhesives were not considered in this model.

Neale et al. (2006) used ADINA to conduct the numerical simulation of CFRP strengthened RC beams. The constitutive laws for compression and tension used to model the concrete were based on ADINA (2004b). The basic features of the constitutive model are: i) a nonlinear stress-strain relation to allow for the weakening of the material under increasing compressive stresses, (ii) failure envelopes to define both failure in tension and crushing in compression, and (iii) a strategy to model the post-cracking and post-crushing behaviour of the material. A uniaxial elastic-plastic stress-strain relationship and a linear elastic orthotropic constitutive relation was adopted for steel reinforcement and FRP composites, respectively. The bond slip model used for FRP/concrete interface was a slight modification of the precise model developed by Lu et al. (2005), which imposed a linear relationship between the bond stress and the slip in the pre-peak zone, and the descending part of the relationship was the same as that in the precise model. Adhesive was neglected in this model. FRP/concrete interface and concrete were modelled by the 2-node interface element and quadrilateral 9-node plane stress elements respectively. Steel reinforcement and FRP laminates are modelled using the 3-node truss element. Most of the beam failed through debonding, and it was found that the bond-slip law proposed by Lu et al. (2005) was efficient and accurate for the FRP/concrete interface.

Aram et al. (2008) used ATENA for finite element analysis of CFRP strengthened RC beams under four-point bending load, and two finite element models FEM1 and FEM2 were developed. For the FEM1, the uniaxial stress–strain diagram and biaxial stress failure criteria were based on Kupfer et al. (1969). The SBeta material property of ATENA was used for the quadrilateral concrete elements. This SBeta material property consists of all nonlinear behaviour of concrete including softening behaviour of concrete. The stress-strain relation of concrete in compression is based on CEB-FIP model (1993) whereas under tension, the relation was assumed to be linear until it reached the maximum tensile strength after which it reduced gradually to zero. Smeared crack model was used for concrete. The steel reinforcement and FRP plate were modelled using bar elements. The behaviour of the FRP/concrete interface was defined according to the bond-slip relationship given by Ulaga et al. (2003). Steel reinforcement was assumed to behave in an elastic–plastic manner with strain hardening effects, while the FRP reinforcement was assumed to behave linearly elastic with brittle fracture in tension. In FEM2 model, the FRP plate and the adhesive layer were modelled by two-dimensional quadrilateral elements. The FRP plate was modelled by elastic plane stress elements. Normal stress could not be given in FEM1 because of the use of one dimensional bar elements for the CFRP reinforcement.

Aktas et al. (2014) modelled CFRP strengthened reinforced concrete beams subjected to four-point bending load using ABAQUS. The Hognestad's model (1955) which was modified in CEB-FIP (1993), was employed as the stress-strain relationship under compression for concrete. A bilinear model (Coronado and Lopez 2006) was adopted for the tensile behaviour of concrete. The concrete damage plasticity model was used to model damage in concrete. Steel and CFRP were modelled as elasto-perfectly plastic and linearly elastic material until reaching failure strain respectively. The bond-slip model for concrete, adhesive and FRP interfaces was based on the bilinear model of Lu et al. (2005). The concrete, steel, CFRP and epoxy were modelled as four-node plane strain element (CPE4R), two-node truss element (T2D2), four-node plane stress element (CPS4R), and four-noded solid element (COH2D4) respectively.

Zhang and Teng (2014) used MSC. MARC for finite element analysis of RC beams strengthened in flexure with externally bonded CFRP under three-point and four-point bending load. In this model, the concrete was modelled using four-node plane stress elements and both the steel bars and the FRP reinforcement were modelled using two-node beam elements. The bond behaviour between FRP and concrete was modelled using four-node cohesive elements. The uniaxial compressive stress–strain curve which was modified by Elwi and Murray (1979) and Saenz's (1964) curve was employed. The exponential tension-softening curve of concrete in tension proposed by Hordijk (1991) was used to represent the tensile behaviour of concrete in which the maximum tensile strength of concrete was calculated based on CEB-FIP (1993). The cracking of concrete was simulated using the smeared crack model available in the general-purpose FE package MSC. MARC. The FRP was modelled as an elastic and isotropic brittle material, and the steel bars including the steel tension bars, steel compression bars and the stirrups were modelled as an elastic-perfectly plastic material. The bond–slip model for concrete/FRP interface was based on Lu et al.'s simplified bond-slip model (2005).

5.2.2. Three Dimensional Finite Element Models

Kishi et al. (2005) used DIANA for the numerical analysis of RC beams strengthened with FRP sheets (AFRP and CFRP) under four-point loading. Steel rebar and FRP sheets were modelled as eight-node solid element, and concrete as six-node solid element, and stirrup as embedded reinforcement elements. Geometrical discontinuities due to debonding of the FRP sheet were taken into account using the FRP sheet debonding model, which was based on Coulomb friction concept. Concrete in compression was defined based on JSCE (2002), and in tension region a linear softening model was used. For rebar and stirrup a bilinear isotropic-hardening model was used, and for FRP a linearly elastic material model until rupture was used. Adhesive was neglected in this model.

Obaidat et al. (2010) modelled the flexural behaviour of CFRP strengthened RC beams subjected to four-point bending load using ABAQUS. Concrete was modelled according to plastic damage model with two main assumptions, i.e., two failure modes are tensile cracking and compressive crushing. In tension, the stress–strain response of the concrete was assumed to be linearly elastic until the value of the failure stress was reached. Beyond the failure stress, the material was represented by a softening stress–strain response where strength reduced to zero gradually. The stress–strain relationship proposed by Saenz (1964) was used as the uni-axial compressive stress–strain curve for concrete. Steel reinforcement was assumed to be elastic and perfectly plastic. Two different material models were used for CFRP, i.e., a linearly elastic-isotropic and a linearly elastic-orthotropic model. Both perfect bond model and cohesive zone model based on Lu et al. (2005) were used for the CFRP/concrete interface. Four-node linear tetrahedral elements were used to model concrete, reinforcement steel and CFRP in this model, and eight-node three-dimensional cohesive element was used to model the interface layer between concrete and FRP.

Choi et al. (2013) used ABAQUS to conduct finite element analysis of FRP (CFRP and GFRP) strengthened RC beams under three-point bending loading. The concrete beams were modelled using three-dimensional eight-node solid elements and the FRP was modelled using four-node shell elements. FRP/concrete interface was modelled using a three-dimensional eight-node cohesive element. Concrete was regarded as an elastic material with tension stiffening and plasticity of concrete was obtained from the compressive and tensile material tests. For FRP composites, a linearly elastic material model was used, and for epoxy cohesive modelling approaches was used to model elastic traction material behaviours and debonding damage behaviours initiated by the maximum stress criteria. Stirrups were not modelled in this model, and adhesive was not modelled as a separate component. An earlier debonding was predicted from FE models than that from the experimental investigation.

Hawileh et al. (2013) used ANSYS to conduct numerical simulation of RC beams externally strengthened with CFRP subjected to four-point bending. Concrete, steel reinforcement, FRP and epoxy were modelled using eight-node SOLID65 brick element, two-node LINK8 element, SHELL99 element and SOLID45 element respectively. The interface between FRP and concrete was modelled as the 3D eight-node linear interface element (INTER205 element). The compressive behaviour of concrete was modelled using Hognestad et al.'s model (1955) and the concrete tensile stress-strain response was regarded as linearly elastic behaviour up to the tensile rupture strength. After the peak tensile stress, a linearly descending tensile stress-strain curve was used. The steel reinforcement and CFRP were assumed to be elasto-plastic and elastic orthotropic respectively. The bond-slip between CFRP, adhesive and concrete was based on an exponential form of the cohesive zone model developed by Xu and Needleman (1994). Most of the FRP attached with concrete with epoxy adhesive failed by plate end debonding.

Pathak et al. (2016) developed two simple finite element model for accurte and effective analysis of structural behavior of FRP strengthened RC beams with and without bond-slip effect under four-point bending loading using FE analysis software ANSYS. All the components of the beam were considered in the models. The three-dimensional eight-node Solid65 element was used to represent the concrete, steel reinforcement was modelled using two-node Link180 element, four-node Shell181 element was used to model FRP, which was smeared as thin plates, and the epoxy adhesive was modelled using eight-node Solid45 element. For the bond slip between FRP, adhesive and concrete interfaces, two-node nonlinear spring element COMBIN39, which had no physical mass and dimension, was employed. The nonlinear stress-strain relationship by Nitereka and Neale (1999) consisting of an ascending curve and linear descending branch was adopted to represent the compressive uniaxial stress-strain relationship of the concrete. The stress-strain curve of concrete in tension is assumed to be isotropic, linear and elastic up to the tensile strength after which crack occurs and stress gradually reduces to zero. The steel rebar is assumed to be elastic and perfectly plastic which behaves identically in tension and compression with stiffness only in axial direction. FRPs are assumed to be linear and elastic until the tension stress reaches its ultimate strength, after which brittle rupture occurs and stress then reduces to zero. A bilinear bond-slip model under static loading developed by Lu et al. (2005) was adopted to model the bond-slip behaviour between FRP, adhesive and concrete. Parametric studies were also carried out to learn the effects of types and thickness of FRP on the structural behavior of FRP strengthened RC beams based on the developed model.

To sum up, most of the developed finite element models are two-dimensional models with a few three-dimensional models. Adhesive has not been considered in most of the developed models assuming bond-slip between concrete and FRP interface. Debonding can take place in between concrete layers, concrete/adhesive interface, adhesive-concrete interface, and hence bond-slip behaviour should be considered in both interfaces.

6. Nonlinear Finite Element Analysis of FRP Strengthened RC Beams under Cyclic Load

6.1. Nonlinear Finite Element Analysis of FRP Strengthened RC Beams under Cyclic Load Assuming Perfect Bond

El-Tawil et al. (2001) modelled the reinforced concrete beams strengthened with CFRP under four-point loading using T-DACS (Time-Dependent Analysis of Composite Sections). The first series of beams were subjected to low moment range from 44 to 89 kN-m, and the second series was subjected to 44 to 132 kN-m. Concrete in compression was modelled using the compression model by Thorenfeldt et al. (1987) and Popovics (1970). In tension, concrete was modelled by ACI 318 code (2014). It was assumed that the modulus of elasticity of the reinforcing steel and FRP remained unchanged during the cyclic loading. The CFRP was assumed to be an elastic-perfectly plastic material. The FRP/adhesive/concrete interface was assumed to be perfectly bonded. The steel reinforcement was modelled as an elastic-plastic material with a postyield strain hardening of 1%. The fatigue behaviour of concrete was based on the linear stress-strain relationship of Holmen (1982). The variation of secant modulus with number of cycles was based on the test results from Bennet and Raju (1971) and Holmen (1982). Results obtained from the analysis were stiffer than the experimental results. The material degradation behaviour of steel and FRP were suggested for accurate prediction of the structural behaviour of FRP strengthened RC beams.

Al-Rousan et al. (2011) conducted a numerical simulation of reinforced concrete beams externally strengthened with CFRP sheets under cyclic four-point bending using ANSYS. Concrete was modelled as a quasi-brittle material and the stress-strain curve in tension was linearly elastic up to the ultimate tensile strength after which concrete cracked and the strength reduced to zero. Steel reinforcement was modelled as an elastic-perfectly plastic material. FRP and epoxy were assumed as orthotropic materials with linear elastic properties. Perfect bond was assumed between concrete, adhesive and

FRP. Concrete, steel, and FRP were modelled by SOLID65 element with smeared crack approach, LINK8 element, and SOLID46 element respectively. It was found that the ultimate capacity of FRP strengthened RC beams under cyclic loading decreased by more than 5% compared to that under static loading. Effect of the number of cycles on the properties of components of FRP strengthened RC was neglected.

Zhang et al. (2008) conducted numerical modelling of GFRP strengthened RC beams under three-point cyclic loading using ANSYS. The constitutive relation of concrete under compression was based on Popovic’s model (1970) and Park et al.’s model (1975). Under tension, the concrete was assumed to be linearly elastic before rupture and the stress then gradually reduced to zero after cracking. FRP and steel rebars were modelled as isotropic linear elastic materials. The 8-node SOLID185 element was used to model the rebar and concrete, and the 4-node elastic SHELL63 element was used to model the FRP composites. Adhesive was neglected, and degradation of properties of concrete, steel and FRP with number of cycles was not considered.

Pathak and Zhang (2016) developed a simple and effective finite element model for nonlinear finite element analyses of structural behavior of FRP strengthened RC beams under cyclic loading. All the components of the beam including concrete, steel rebar, FRP sheet, adhesive and shear strengthening stirrups were included in the model. Material nonlinear properties of concrete and steel rebars were accounted for, while the FRP and adhesive were considered to be linearly elastic until rupture. The degradation of each material under cyclic loading was considered and defined using the user-programmable features in ANSYS. Parametric studies were also carried out to learn the effects of types, thickness, and length of FRP on the structural behavior of FRP-strengthened RC beams based on the FEM-C model.

In most of the reported numerical studies, the material degradation of components with the number of cycles has not been considered, leading to an inaccurate prediction of the structural behaviour. In order to assess the behaviour of FRP strengthened RC beams under cyclic load accurately, it is necessary to include the effects of cyclic loading on all the components of the beam. Erki and Heffernan (2004) suggested that the bond strength of the FRP/concrete interface may reduce with number of cycles of load, hence it is very important to consider proper bond strength degradation model with number of cycles.

6.2. Nonlinear Finite Element Analysis of FRP Strengthened RC Beams under Cyclic Load with Bond-Slip

Ferrier et al. (2011) modelled CFRP strengthened RC beam under cyclic loading. The concrete in compression and in tension was deduced from a strain–stress model by Varastehpour and Hamelin (1997). The mechanical behaviour of steel was characterised by elastic-yielding. The FRP was assumed to be linear and elastic until failure. The bond-slip between concrete, adhesive and FRP was based on the analytical solution provided by Täljsten (1997). Material degradation property of concrete with number of cycles of the load was based on Aas-Jakobsen's model (1970) and the decrease in Young's modulus was based on Balaguru and Shah's model (1982). The model for reinforcing steel was based on Mander et al.'s model (1994). The response of FRP and adhesive joint subjected to cyclic load was based on Ferrier et al.'s model (2011).

Loo et al. (2012) conducted a numerical simulation of CFRP strengthened beam under cyclic loading. The constitutive relation of material behaviour of concrete, steel reinforcement, FRP and bond stress-slip relation was based on Chong et al. (2004) and Khomwan et al. (2010). For the fatigue analysis, the stress–strain relationship for concrete in compression under fatigue loading was modelled based on Holmen (1982). The steel reinforcement was based on CEB-FIP model (1993). Elastic-brittle stress-strain relationship was used for FRP assuming the strength of FRP would not change with fatigue. The proposed FRP to concrete bond-slip model (Loo et al. 2012) under cyclic load was used for the FE analysis. The four-node isoparametric concrete element was used for concrete, bar element for steel reinforcement, elastic-plastic truss elements for FRP composites, and 1D bond interface element based on Khomwan et al (2010) for bond slip between concrete and FRP interface. Degradation of FRP properties with number of cycles was neglected in this model although it was recommended to be included in future research.

Pathak and Zhang (2016) modelled the the structural behavior of FRP strengthened RC beams under cyclic loading considering the bond-slip between FRP, adhesive and concretet. The degradations of material properties of concrete, steel reinforcement, and FRP due to cyclic loading were taken into account.

CONCLUSION AND FUTURE RESEARCH

Bond behaviour of FRP/adhesive/concrete interfaces play important role in determining strucutural character of FRP strengthened RC beams along with its material properties of components such as concrete, steel, FRP and adhesive. Investigations in structural behaviour of FRP strengthened RC beams subjected to cyclic loading have suggested that the properties of components of FRP strengthened RC beam degrades with the increase of the number of cycles of load. Proper selection of material properties along with its degradation with number of cycles, and bond stress-slip law is very important for the accurate and efficient analysis of FRP strengthened RC beams. In this chapter, these models are reviewed and the developed finite eelment models are also reviewed. It is found that

- Most of the finite element analyses on FRP strenghened RC beams focus on the structural behavior under static loading with a perfect bond assumption between the FRP/concrete/adhensive, leading to inaccurate modelling of the structural performance;
- There is a lack of the finite element anlaysis of the structural behavior of FRP strenghend RC beam under cylic loading;
- The material property of concrete, FRP and steel degrade under cyclic loading. However in most of the reported numerical studies of the the structural behavior of FRP strenghend RC beam under cylic loading, the material property degradtion under cyclic loading has not been account for although it will affect the accuracy of the prediction significantly;
- Adhesive is an important component of hte FRP strenghened RC beam and play important role in the strucutral behavior. However In most of the reported numerical studies, adhesive has not been counsidered in the modelling, leading to inaccurate prediction of the structural behavior.
- Finite element models developed so far for FRP strengthened RC beams under static and cyclic load in literature is lack either proper material properties or bond stress-slip laws, hence simple, effective and accurate three-dimensional finite element model whcih includes all the compoents, proper material properties and bond stress-slip law is in demand and should be developed in the future research for more effective and acute structural analysis and design.

References

Aas-Jakobsen, K. Fatigue of concrete beams and columns. *Division of Concrete Struc. Bulletin*, 1970, Norwegian Institute of Technology.

ACI Committee 215. Considerations for design of concrete structures subject to fatigue loading, *ACI Materials Journal*, 1974, 71 (3), 97-121.

Adimi, M. R.; Rahman, A. H.; Benmokrane, B. New method for testing fiber-reinforced polymer rods under fatigue. *Journal of Composites for Construction,* 2000, 4(4), 206-13.

Al-Rousan, R.; Issa, M. Fatigue performance of reinforced concrete beams strengthened with CFRP sheets. *Construction and Building Materials*, 2011, 25(8), 3520-9.

ADINA Theory and Modelling Guide, Vol. I, Chapter 3, Version 8.2. ADINA R&D Inc., Watertown, MA, USA, 2004.

ANSYS, Inc. Release 15.0 Documentation for ANSYS, SAS IP, Inc, USA, 2013.

Aktas, M.; Sumer, Y. Nonlinear finite element analysis of damaged and strengthened reinforced concrete beams. *Journal of Civil Engineering and Management*, 2014, 20(2), 201-10.

Aram, M. R.; Czaderski, C.; Motavalli, M. Debonding failure modes of flexural FRP-strengthened RC beams. *Composites Part B: Engineering*, 2008, 39(5), 826-41.

Arockiasamy, M.; Sowrirajan, R.; Shahawy, M.; Beitelman, T. Repair of damaged pretensioned solid slab using CFRP laminates, *Proceedings of Second Non-metallic (FRP) Reinforcement for Concrete Structures (FRPRCS-2)*, (ed.) L. Taerwe, London, 1995, 492-500.

Balaguru, P.; Shah, S. A method of predicting crack widths and deflections for fatigue loading. *ACI Special Publication*, 1982, 75, 153-76.

Bangash, M. Concrete and concrete structures: Numerical modelling and applications, *Elsevier Applied Science*, New York, 1989.

Bennett, E.; Raju, N. Cumulative fatigue damage of plain concrete in compression, *Proceedings of the International Conference on Structure, Solid Mechanics and Engineering Design in Civil Engineering Materials*, (ed.) M. Teeni, Southamton, England, 1969, 1-14.

Bizindavyi, L.; Neale, K.; Erki, M. Experimental investigation of bonded fiber reinforced polymer-concrete joints under cyclic loading, *Journal of Composites for Construction*, 2003;7(2), 127-34.

Boardman, Bruce. Fatigue Resistance of Steels. ASM Handbook, Volume 01-Properties and Selection: Irons, Steels, and High-Performance Alloys, *ASM International Handbook Committee*, 1st ed. ASM International, 1990.

Camata, G.; Spacone. E.; Zarnic, R. Experimental and nonlinear finite element studies of RC beams strengthened with FRP plates. *Composites Part B: Engineering*, 2007, 38(2), 277-88.

Choi, E.; Utui, N.; Kim, H. S. Experimental and analytical investigations on debonding of hybrid FRPs for flexural strengthening of RC beams. *Composites Part B: Engineering*, 2013, 45(1), 248-56.

Chong, K. T.; Gilbert, R. I.; Foster, S. J. Modelling time-dependent cracking in reinforced concrete using bond-slip interface elements. *Computers and Concrete*, 2004, 1(2), 151-68.

Comité Euro-International du Béton (CEB-FIP). Model code1990. CEB Bulletin d'Information no. 213, Paris, 1993.

Coronado, C. A.; Lopez, M. M. Sensitivity analysis of reinforced concrete beams strengthened with FRP laminates. *Cement and Concrete Composites*, 2006, 28(1), 102-14.

Dai, J.; Saito, Y.; Ueda, T.; Sato, Y. Static and fatigue bond characteristics of interfaces between CFRP sheets and frost damage experienced concrete. *Proceedings of Seventh International Symposium on Fiber Reinforced Polymer Reinforcement for Reinforced Concrete Structures (FRPRCS-7)*, (ed.) C. K. Shield, J. P. Busel, S. L. Walkup and D. D. Gremel, Kansas City, USA, 2005, 1515-1530.

Desayi, P.; Krishnan, S. Equation for the stress-strain curve of concrete. *ACI Journal Proceedings*, 1964, 61(3), 345-50.

DIANA, release 7.2., Division of Engineering Mechanics and Information Technology, TNO Building and Construction Research, Deflt, The Netherlands, 2000.

Dillman, R. Die Spannungsverteilung in der Biegedruckzone von Stahlbetonquerschnitten bei häufig wiederholter Belastung, *PhD thesis*, Technischen Hochschule Darmstadt, Germany, 1981.

El-Tawil, S.; Ogunc, C.; Okeil, A.; Shahawy, M. Static and fatigue analyses of RC beams strengthened with CFRP laminates. *Journal of Composites for Construction*, 2001, 5(4), 258-67.

Elwi, A. A., Murray, D. W. A 3D hypoelastic concrete constitutive relationship. *Journal of the Engineering Mechanics Division*. 1979, 105(4), 623-41.

Heffernan, P.; Erki, M. Fatigue behavior of reinforced concrete beams strengthened with carbon fiber reinforced plastic laminates. *Journal of Composites for Construction*; 2004, 8(2), 132-40.

Ferrier, E.; Bigaud, D.; Hamelin, P.; Bizindavyi, L.; Neale, K. Fatigue of CFRPs externally bonded to concrete. *Materials and Structures*, 2005, 38(1), 39-46.

Ferrier, E.; Bigaud, D.; Clement, J.; Hamelin, P. Fatigue-loading effect on RC beams strengthened with externally bonded FRP. *Construction and Building Materials*, 2011, 25(2), 539-46.

Gheorghiu, C.; Labossière, P.; Raiche, A. Environmental fatigue and static behavior of RC beams strengthened with carbon-fiber-reinforced polymer. *Journal of Composites for Construction*, 2004, 8(3), 211-18.

Goodman, R. E.; Taylor, R. L.; Brekke, T. L. A model for the mechanics of jointed rocks. *Journal of Soil Mechanics & Foundations Div*, 1968, 94(3), 637-60.

Hahn, H. T.; Tsai, S. W. Nonlinear elastic behavior of unidirectional composite laminae. *Journal of Composite Materials.* 1973, 7(1), 102-18.

Hashemi, S. H.; Rahgozar, R.; Maghsoudi, A.A. Finite Element and Experimental Serviceability Analysis of. *American Journal of Applied Sciences*, 2007, 4(9), 725-35.

Hawileh, R. A.; Naser, M. Z.; Abdalla, J. A. Finite element simulation of reinforced concrete beams externally strengthened with short-length CFRP plates. *Composites Part B: Engineering*, 2013, 45(1), 1722-30.

Hognestad, E.; Hanson, N. W.; McHenry, D. Concrete stress distribution in ultimate strength design. *Journal ACI*, 1955, 52(4), 455-80.

Holmen, J. O.; Fatigue of concrete by constant and variable amplitude loading. *ACI Special Publication*; 1982, 75, 71-110.

Holmer, N. P. Parametric study of the bond between fiber reinforced polymers and concrete using finite element analysis. *Master's Thesis*, Faculty of the Graduate School, Marquette University, Milwaukee, Wisconsin, 2010.

Hollaway, L. C.; Leeming, M. Strengthening of reinforced concrete structures: Using externally-bonded FRP composites in structural and civil engineering, *Woodhead Publishing*, 1999.

Homam, S. M. Durability of fibre-reinforced polymers (FRP) used in concrete structures, *Master Thesis*, Graduate Department of Civil Engineering, University of Toronto, 2000.

Hordijk, D. Local approach to fatigue of concrete, *PhD thesis*, Delft University of Technology; 1991.

Hu, H. T.; Lin, F. M.; Jan, Y. Y. Nonlinear finite element analysis of reinforced concrete beams strengthened by fiber-reinforced plastics. *Composite Structures*, 2004, 63(3), 271-81.

Imperatore, S.; Lavorato, D.; Nuti, C.; Santini, S.; Sguerri, L. Numerical modeling of existing RC beams strengthened in shear with FRP U-sheets. *Proceedings in 6th International Conference on FRP Composites in Civil Engineering (CICE)*, (ed.) G Monti, Rome, Italy, 2012, 1-8.

Ingason, D. F. O. A. Modelling and simulation of reinforced concrete beams, *Masters Thesis*, Department of Applied Mechanics, Chalmers University of Technology, Sweden, 2013.

Izumo, J.; Shin, H.; Maekawa, K.; Okamura, H. An analytical model for RC panels subjected to in-plane stresses. *Concrete Shear in Earthquake. Elsevier Applied Science*, New York, 1992, 206-15.

Japan Society of Civil Engineers (JSCE). Standard specifications for concrete structures-2002. Structural performance verification, Tokyo, Japan, 2002.

Keuser, M.; Mehlhorn, G. Finite element models for bond problems. *Journal of Structural Engineering*, 1987, 113(10), 2160-73.

Khan, A; Al-Gadhib, A.; Baluch, M. Experimental and computational modeling of low cycle fatigue damage of CFRP strengthened reinforced concrete beams. *International Journal of Damage Mechanics*, 2011, 20(2), 211-43.

Khomwan, N.; Foster, S. J.; Smith, S. T. FE modeling of FRP-repaired planar concrete elements subjected to monotonic and cyclic loading. *Journal of Composites for Construction*, 2010, 14(6), 720-9.

Kim, Y. J.; Heffernan, P. J. Fatigue behavior of externally strengthened concrete beams with fiber-reinforced polymers: state of the art. *Journal of Composites for Construction*, 2008, 12(3), 246-56.

Kinloch, A. Adhesion and Adhesives, Science and Technology, Chapman and Hall. New York, 1987.

Kishi, N.; Zhang, G.; Mikami, H. Numerical cracking and debonding analysis of RC beams reinforced with FRP sheet. *Journal of Composites for Construction*, 2005, 9(6), 507-14.

Kupfer, H.; Hilsdorf, H. K.; Rusch, H. Behavior of concrete under biaxial stresses. *ACI Journal Proceedings*. 1969, 66(8), 656:66.

Loo, K. Fatigue behaviour of CFRP-repaired corroded RC beams. *PhD. Thesis*, School of Civil and Environmental Engineering, University of New South Wales, Sydney, Australia, 2010.

Loo, K. Y. M.; Foster, S. J.; Smith, S. T. FE modeling of CFRP-repaired RC beams subjected to fatigue loading. *Journal of Composites for Construction*. 2012, 16(5), 572-80.

Lu, X. Z.; Teng, J. G.; Ye, L. P.; Jiang, J. J. Bond–slip models for FRP sheets/plates bonded to concrete. *Engineering structures*, 2005, 27(6), 920-37.

Mahal, M. S. H. Fatigue behaviour of RC beams strengthened with CFRP, *PhD thesis*, Division of Structural and Construction Engineering Department of Civil, Environmental and Natural Resources Engineering, Luleå University of Technology SE - 971 87, Lulea, Sweden, 2015.

Mander, J.; Panthaki, F.; Kasalanati, A. Low-cycle fatigue behavior of reinforcing steel. *Journal of Materials in Civil Engineering*. 1994, 6(4), 453-68.

Mazzotti, C.; Savoia, M. FRP-concrete bond behaviour under cyclic debonding force. *Advances in Structural Engineering*, 2009, 12(6), 771-80.

Minouei, M. B. Finite Element Analysis of Bond Characteristics at the FRP-Concrete Interface, *Master thesis*, Department of Civil Engineering and Applied Mechanics McGill University, Montreal Quebec, Canada, 2011.

Monti, G.; Renzelli, M.; Luciani, P. FRP adhesion in uncracked and cracked concrete zones. *Proceedings of the Sixth International Symposium on FRP Reinforcement for Concrete Structures (FRPRCS-6)*, (ed.) K. H. Tan, Singapore, 2003; 183-92.

Muralidharan, U.; Manson, S. A modified universal slopes equation for estimation of fatigue characteristics of metals. *Journal of Engineering Materials and Technology*, 1988, 110(1), 55-8.

Nakaba, K.; Kanakubo, T.; Furuta, T.; Yoshizawa, H. Bond behavior between fiber-reinforced polymer laminates and concrete. *Structural Journal*, 2001, 98(3), 359-67.

Neale, K.; Ebead, U.; Baky, H. A.; Elsayed, W.; Godat, A. Analysis of the load-deformation behaviour and debonding for FRP-strengthened concrete structures. *Advances in Structural Engineering*. 2006, 9(6), 751-63.

Neubauer, U.; Rostasy, F. S. Bond failure of concrete fiber reinforced polymer plates at inclined cracks-experiments and fracture mechanics model. *In Proc. of 4th International Symposium on Fiber Reinforced Polymer Reinforcement for Reinforced Concrete Structures*, SP-188. Farmington Hills (MI): ACI, Baltimore, (ed.) C. W. Dolan, S. H. Rizkalla and A Nanni, USA, 1999, 369–82.

Nitereka, C.; Neale K. W. Analysis of reinforced concrete beams strengthened in flexure with composite laminates, *Can. J. Civ. Eng*., 1999, 26(5), 646–654.

Niu, H.; Wu, Z. Peeling-off criterion for FRP-strengthened R/C flexural members. FRP Composites in Civil Engineering *Proceedings of the International Conference on FRP composites in Civil Engineering*, (ed.) J. G. Teng, Hongkong, China 2001, 571-78.

Nour, A.; Massicotte, B.; Yildiz, E.; Koval, V. Finite element modeling of concrete structures reinforced with internal and external fibre-reinforced polymers. *Canadian Journal of Civil Engineering*. 2007, 34(3), 340-54.

Obaidat, Y. T.; Heyden, S.; Dahlblom, O. The effect of CFRP and CFRP/concrete interface models when modelling retrofitted RC beams with FEM. *Composite Structures*, 2010, 92(6), 1391-8.

Ople, F.; Hulsbos, C. Probable fatigue life of plain concrete with stress gradient. *ACI Journal Proceedings*, 1966, 63(1), 59-82.

Papakonstantinou, C. G.; Petrou, M. F.; Harries, K. A. Fatigue behavior of RC beams strengthened with GFRP sheets. *Journal of Composites for Construction*, 2001, 5(4), 246-53.

Park, R., Paulay, T. Reinforced concrete structures: John Wiley & Sons, 1975.

Pathak, P.; Zhang, Y. X.; Teng, X. Nonlinear finite element analysis of FRP strengthened RC beams with bond-slip effect, *International Journal for Numerical Methods*, 2016, paper accepted.

Pathak, P.; Zhang, Y. X. Nonlinear finite element analyses of FRP-strengthened steel-reinforced concrete beams under cyclic loading, *Structural Concrete Journal*, Submitted in July 2016.

Pathak, P.; Zhang Y. X. Nonlinear finite element analyses of FRP-strengthened steel-reinforced concrete beams under cyclic loading, Special Issue of Journal of Bridge Engineering, ASCE, submitted Nov. 2016.

Pham, H. B.; Al-Mahaidi, R. Modelling of CFRP-concrete shear-lap tests. *Construction and Building Materials*, 2007, 21(4), 727-35.

Piggott, M. Load bearing fibre composites: Springer Science & Business Media, 2002.

Popovics, S. A review of stress-strain relationships for concrete. *ACI Journal Proceedings*, 1970, 67(3), 243-48.

Prince, R. E. Characteristics and Behaviors of Fiber Reinforced Polymers (FRPs) Used for Reinforcement and Strengthening of Structures, *Prince Engineering*, PLC, 2011.

Saenz, L. Equation for the stress-strain curve of concrete. *ACI Journal*, 1964, 61(9), 1229-35.

Savoia, M.; Ferracuti, B.; Mazzotti, C. Nonlinear bond-slip law for FRP-concrete interface. *Proceedings of the Sixth International Symposium on FRP Reinforcement for Concrete Structures (FRPRCS-6)*, (ed.) K. H. Tan, Singapore, 2003, 163-72.

Sundarraja, M.; Rajamohan, S. Flexural strengthening effect on RC beams by bonded composite fabrics. *Journal of Reinforced Plastics and Composites*, 2008, 27(14), 1497-513.

Supaviriyakit, T.; Pornpongsaroj, P.; Pimanmas, A. Finite element analysis of FRP-strengthened RC beams. *Journal of Science and Technology*, 2004, 26(4), 497-507.

Tan, K. Effect of cyclic loading on FRP-concrete interfacial bond strength. *Proc, Int Symp on Latest Achievement of Technology and Research on Retrofitting Concrete Structures*, Japan Concrete Institute, Kyoto, Japan, 2003, 1-8.

Täljsten, B. Strengthening of beams by plate bonding. *Journal of Materials in Civil Engineering*; 1997, 9(4), 206-12.

Tavárez, F. A. Simulation of behavior of composite grid reinforced concrete beams using explicit finite element methods, *Master Thesis*, University of Wisconsin-Madison, 2001.

Teng, J.; Smith, S. T.; Yao, J.; Chen, J. Intermediate crack-induced debonding in RC beams and slabs. *Construction and Building Materials*, 2003, 17(6), 447-62.

Teng, X. Nonlinear finite element analysis of FRP-strengthened concrete slabs under static and traffic loads, *PhD. thesis*, School of Engineering and Information Technology, Univ. of New South Wales Canberra, Canberra, Australia, 2013.

Teng, X.; Zhang, Y. X.; Lin, X.; Two new composite plate elements with bond-slip effect for nonlinear finite element analysis of FRP-strengthened concrete slabs, *Computers and Structures*, 2015, 148, 35-44.

Thorenfeldt, E.; Tomaszewicz, A.; Jensen, J. Mechanical properties of high-strength concrete and application in design. *Proceedings of the Symposium Utilization of High Strength Concrete*, (ed.) I. Holand, Tapir, Trondheim, Norway, 1987, 149-159.

Ulaga, T.; Vogel, T.; Meier, U. Bilinear stress-slip bond model: theoretical background and significance. *Proceedings of the Sixth International Symposium on FRP Reinforcement for Concrete Structures (FRPRCS-6)*, (ed.) K. H. Tan, Singapore, 2003, 153-62.

Varastehpour, H.; Hamelin, P. Strengthening of concrete beams using fiber reinforced plastics. *Mater Struct*. 1999, 30, 160–66.

Vecchio, F. J.; Collins, M.P. The modified compression-field theory for reinforced concrete elements subjected to shear. *ACI J*. 1986, 83(2), 219-31.

Vecchio, F. J. Nonlinear finite element analysis of reinforced concrete membranes. *ACI Structural Journal*, 1989, 86(1), 26-35.

Vecchio, F. J. Reinforced concrete membrane element formulations. *Journal of Structural Engineering*, 1990, 116(3), 730-50.

Wong, R. S.; Vecchio, F. J. Towards modeling of reinforced concrete members with externally bonded fiber-reinforced polymer composites. *ACI Structural Journal*. 2003, 100(1), 47-55.

Wu, Z.; Yin, J. Fracturing behaviors of FRP-strengthened concrete structures. *Engineering Fracture Mechanics*. 2003, 70(10), 1339-55.

Xu, X. P.; Needleman, A. Numerical simulations of fast crack growth in brittle solids. *Journal of the Mechanics and Physics of Solids*, 1994, 42(9), 1397-434.

Yun, Y.; Wu, Y. F.; Tang, W. C. Performance of FRP bonding systems under fatigue loading. *Engineering Structures*, 2008, 30(11), 3129-40.

Zanuy, C.; Albajar, L.; De la Fuente, P. Sectional analysis of concrete structures under fatigue loading. *ACI Structural Journal*, 2009, 106(5), 667.

Zhang, R.; Shi, Z. Numerical simulation of rebar/concrete interface debonding of FRP strengthened RC beams under fatigue load. *Materials and Structures*, 2008, 41(10), 1613-21.

Zhang, S. S.; Teng, J. G. Finite element analysis of end cover separation in RC beams strengthened in flexure with FRP. *Engineering Structures*, 2014, 75, 550-60.

BIOGRAPHICAL SKETCH

Prabin Pathak

Affiliation: University of New South Wales Canberra @ Australian Defence Force Academy

Education: Masters of Civil Engineering

Business Address: School of Engineering and Information Technology, University of New South Wales, Canberra, Australian Defence Force Academy, ACT, 2600, Australia

Honors: Research scholarship from University of New South Wales

Publications Last 3 Years:

Pathak, P.; Zhang, Y. X.; Teng, X. Nonlinear finite element analysis of FRP strengthened RC beams with bond-slip effect. *International Journal of Computational Method*, 2016, 14(2), 1750032(1-19).

Pathak, P.; Zhang, Y. X. Finite element simulation for nonlinear finite element analysis of FRP strengthened RC beams with bond-slip effect. *Applied Mechanics and Materials*, 2016, 846, 440-445.

Pathak, P.; Zhang, Y. X. Nonlinear finite element analysis of FRP strengthened RC beams. *The 8th International Structural Engineering and Construction Conference*, (ed.) S. Saha, Y. Zhang, Y. Yazdani and A. Singh, Sydney, Australia, November 23-28, 2015, 463-68.

BIOGRAPHICAL SKETCH

Y. X. Zhang

Affiliation: University of New South Wales, Canberra

Education: BE, ME, PhD

Business Address: School of Engineering and Information Technology, University of New South Wales, Canberra, Australian Defence Force Academy, ACT, 2600, Australia

Honors:

Best Student Paper Award, Yuguo Yu, Amar Khennane, Y. X. Zhang, Numerical modelling of degradation of cement paste under external sulfate attack, the 2nd Australiasian Conference on Computational Mechanics (ACCM2015), Brisbane, Australia, Nov. 30-Dec 1, 2015.

Best paper award, Chengjun Liu, Y. X. Zhang, Chunhui Yang, Numerical investigation on mechanical behavior of aluminum foams using a representative volume element method, the 4th International Conference on Mechanical Engineering, Materials and Energy, Singapore, 2014.

The Spitfire Memorial Defence Fellowship, Australia, 2012 (Received by the Australian Governor General).

High Impact Publication Award, School of Engineering and Information Technology, UNSW@ADFA, 2011.

Publications Last 3 Years:

Edited Books:

1. Swapan Saha, Y. X. Zhang, Siamak Yazdani, Amarjit Singh (editors), Implementing Innovative Ideas in Structural Engineering and Project Management, ISEC Press, 2015, ISBN: 978-0-9960437-1-7.

Book Chapters:

2. C. Yang, Y. X. Zhang, Virtual engineering-based teaching on engineering design theories to engineering students, book chapter, *Handbook of Research on Educational Resource Sharing in Engineering Programs*, Ataur Rahman, Graham Jenkins, Roger Hadgraft, David Brian Lowe (Eds.), IGI Global, 2016.
3. Y. X. Zhang, He Tian, Toughening mechanisms for whisker-reinforced composites, Chapter 7, *Toughening mechanisms in composite materials*, Qinghua Qin, Jianqiao Ye (Eds.), Woodhead Publishing Limited, 2015, pp191-207.
4. Y. X. Zhang, Xiaoshan Lin, Toughening mechanics for FRP reinforced concrete beams, Chapter 14, *Toughening mechanisms in composite materials*, Qinghua Qin, Jianqiao Ye (Eds.), Woodhead Publishing Limited, 2015, pp373-392.

Referred Journal Articles:

5. He Tian, Y. X. Zhang, Tensile and shrinkage behaviour of green hybrid fibre-reinforced cementitious composites, Cement and Concrete Composites, paper accepted on Nov. 9 2016.
6. Chengjun Liu, Y. X. Zhang, L. Ye, (2017). High velocity impact responses of sandwich panels with metal fibre laminate skins and aluminum foam, Journal of Impact Engineering, 100, 139-153.
7. Chengjun Liu, Y. X. Zhang, C. Yang, Micromechanics-based modelling of mechanical behavior of aluminium foams, International Journal of Mechanical Science, accepted on Aug. 31, 2016.
8. Ting Huang, Y. X. Zhang,(2016). Numerical modelling of mechanical behaviour of engineered cementitious composites under uniaxial tension, Computers and Structures, 173, 95-108.

9. Hu Chen, Mengyan Zang, Y. X. Zhang, (2016). A ghost particle-based approach for the combined finite-discrete element method, Finite Elements in Analysis and Design, 114, 68-77.
10. Ting Huang, Y. X. Zhang, C. Yang, (2016). Multiscale modelling of multiple-cracking tensile fracture behavior of engineered cementitious composites, Engineering Fracture Mechanics, 160, 52-66.
11. He Tian, Y. X. Zhang, (2016). The influence of bagasse fibre and fly ash on long-term properties of green cementitious composites, Construction and Building Materials, 111, 237-250.
12. He Tian, Y. X. Zhang, C. Yang, YN Ding (2016). Development of nature fiber reinforced cementitious composites, Structural Concrete Journal, 17(4), DOI: 10.1002/suco.201500177.
13. Xiaoshan Lin, Y. X. Zhang, (2016). Nonlinear finite element analysis of FRP-strengthened reinforced concrete panels under blast loads, International Journal of Computational Methods, 13 (4), 1641002-1-1641002-17.
14. Prabin Pathak, Y. X. Zhang, Xiaodan Teng, (2016). Nonlinear finite element analysis of FRP strengthened RC beams with bond-slip effect, International Journal for Numerical Methods, paper accepted in Aug. 2016.
15. Y. X. Zhang, (2016). Meet our editorial board member, Recent Patents on Mechanical Engineering, 9, 183.
16. He Tian, Y. X. Zhang, C. Yang, (2016). Numerical modelling of mechanical behaviour of fibre reinforced cementitious composites, Applied Mechanics and Materials, 846, 139-144.
17. Chengjun Liu, Y. X. Zhang, C. Yang, (2016). Representative volume element-based modelling of closed-cell aluminum foams, Applied Mechanics and Materials, 846, 530-534.
18. Yuguo Yu, Amar Khennane, Y. X. Zhang, (2016). Numerical modelling of degradation of cement paste under external sulfate attack, Applied Mechanics and Materials, 846, 127-132.
19. Hu Chen, Y. X. Zhang, Mengyan Zang, Paul J. Hazell, (2016). A Lagrangian coupling approach for the combined finite-discrete element method, Applied Mechanics and Materials, 846, 518-523.
20. Prabin Pathak, Y. X. Zhang, (2016). A new finite element model for nonlinear finite element analysis of FRP strengthened RC beams with bond-slip effect, Applied Mechanics and Materials, 846, 440-445.

21. He Tian, Y. X. Zhang, L. Ye, C. Yang (2015), Mechanical properties of green hybrid fibre reinforced cementitious composites. Construction and Building Materials, 95, 152-163.
22. Yuguo Yu, Y. X. Zhang, Amar Khennane, (2015). Numerical modelling of degradation of cement-based materials under leaching and external sulfate attack, Computers and Structures, 158, 1-14.
23. Hu Chen, Y. X. Zhang, Mengyan Zang, Paul J. Hazel (2015). An accurate and robust contact detection algorithm for article-solid interaction in combined finite-discrete element analysis, International Journal for Numerical Methods in Engineering, 103, 598-624.
24. Xiaodan Teng, Y. X. Zhang, Xiaoshan Lin, (2015). Two new composite plate elements with bond-slip effect for nonlinear finite element analysis of FRP-strengthened concrete slabs, Computers and Structures, 148, 35-44.
25. Ting Huang, Y. X. Zhang, Cheng Su, Robert Lo, (2015). Effect of slip-hardening interface behavior on fiber rupture and crack bridging in fiber reinforced cementitious composites, Journal of Engineering Mechanics, ASCE, 04015035-1-04015035-13, DOI: 10.1061/(ASCE)EM.1943-7889.0000932.
26. Xiaodan Teng, Y.X. Zhang, (2015). Nonlinear finite Analyses of FRP-strengthened reinforced concrete slabs under fixed-point cyclic loading, Journal of Composites for Construction, ASCE, 19 (3), 10.1061/ (ASCE)CC.1943-5614.0000519,04014057.
27. Chengjun Liu, Y. X. Zhang, Rikard Heslehurst (2014). Impact resistance and bonding capability of sandwich panels with fibre metal laminate skins and aluminum foam core, Journal of Adhesion Science and Technology, 28(24), 2378-2392.(2010 ERA ranking B).
28. Long Bai, Yuhong Cui, Y. X. Zhang, Na Zhao (2014). A three-dimensional numerical simulation of cell behavior in a flow chamber based on fluid-solid interaction, Bio-Medical Materials and Engineering, 24, 2645-2655. (2010 ERA ranking B).
29. Xiaodan Teng, Y. X. Zhang, (2014). Nonlinear finite element analysis of FRP-strengthened reinforced concrete slabs using a new layered composite plate element, Composite Structures, 114, 20-29.
30. Xiaoshan Lin, Y. X. Zhang (2014). Evaluation of bond stress-slip models for FRP reinforcing bars in concrete, Composite Structures, 107, 131-141. (ERA ranking A).

31. Xiaoshan Lin, Y. X. Zhang, Paul J. Hazell, (2014). Modelling the responses of reinforced concrete panels under blast loading, Materials & Design, 56, 620-628.(ERA ranking A).
32. Yuguo Yu, Y. X. Zhang, Yansheng Huang (2014). Investigation of bond strength of FRP-to-concrete interface, Applied Mechanics and Materials, 553, 655-660.
33. Xiaoshan Lin, Y. X. Zhang, Paul J. Hazell (2014). Blast modeling of steel reinforced concrete panels, Applied Mechanics and Materials, 553, 100-108.
34. Xiaoshan Lin, Y. X. Zhang (2014). Finite element analysis of FRP-reinforced concrete beams with bond-slip effect, Applied Mechanics and Materials, 553, 661-666.
35. Chengjun Liu, Y. X. Zhang, Qing H. Qin, Rikard Heslehurst (2014). High velocity impact modeling of sandwich panels with aluminum foam core and aluminum sheet skins, Applied Mechanics and Materials, 553, 745-750.
36. Hu Chen, Y. X. Zhang, Mengyan Zang, Paul J. Hazell (2014). An explicit Lagrange constraint method for finite element analysis of frictionless 3D contact/impact problems, Applied Mechanics and Materials, 553, 751-756.

Refereed Conference papers

Best paper award:

Yuguo Yu, Amar Khennane, Y. X. Zhang, (2015). Numerical modelling of degradation of cement paste under external sulfate attack, the 2nd Australiasian Conference on Computational Mechanics (ACCM2015), Brisbane, Australia, Nov. 30-Dec 1, 2015.

37. *Liu Chengjun, Zhang YX, Yang Chunhui (2014). Numerical investigation on mechanical behaviour of aluminium foams using a representative volume element method, the 4th International Conference on Mechanical Engineering, Materials and Energy (ICMEME2014), Singapore, Nov. 14-15, 2014, full paper accepted to be published in Advanced Mechanics and Materials.

Keynotes:

38. Y. X. Zhang, He Tian (2014). Mechanical behavior of a green hybrid fibre- reinforced cementitious composite, Plenary Lecture speaker in BICTAM Symposium on Mechanical Behaviors and Experimental Methods of Advanced Materials, Tianjin, China, May 8-9, 2014. (Abstract only published).
39. Ting Huang, Y. X, Zhang, C. Yang, Multiscale modelling of multiple-cracking fracture behavior of engineered cementitous composites, the 6th International Conference on Computational methods (ICCM2015), Auckland, New Zealand, July 14-17, 2015. (minisymposium keynote).
40. Hu Chen, Y. X. Zhang, Mengyan Zang, Paul J. Hazell, A ghost particle-based coupling approach for combined finite–discreite element method, the 6th International Conference on Computational methods (ICCM2015), Auckland, New Zealand, July 14-17, 2015. (minisymposium keynote).
41. Xiaoshan Lin, Y. X. Zhang, Numerical modelling of FRP-strengthened reinforced concrete panels under blast loading, Applied Mechanics and Materials, The 2nd Australiasian Conference on Computational Mechanics (ACCM2015), Brisbane, Australia, Nov. 30-Dec 1, 2015. (Session keynote).
42. He Tian, Y. X. Zhang, C. Yang, Numerical modelling of mechanical behaviour of fibre reinforced cementitious composites, Applied Mechanics and Materials, the 2nd Australiasian Conference on Computational Mechanics (ACCM2015), Brisbane, Australia, Nov. 30-Dec 1, 2015. (Session keynote).
43. Chengjun Liu, Y. X. Zhang, C. Yang, Representative volume element-based modelling of closed-cell aluminum foams, Applied Mechanics and Materials, The 2nd Australiasian Conference on Computational Mechanics (ACCM2015), Brisbane, Australia, Nov. 30-Dec 1, 2015. (Session keynote).

Invited:

44. X. Lin, Y. X. Zhang, Parametric study of FRP-strengthened reinforced concrete panels under blast loads, the 6th International Conference on Computational methods (ICCM2015), Auckland, New Zealand, July 14-17, 2015. (minisymposium invited paper).

General:

45. Liu Chengjun, Zhang YX, Yang Chunhui (2016). Numerical investigation on mechanical behaviour of aluminium foams using a representative volume element method, MATEC Web of Conferences, 65, 03003, the international conference on Nanomaterial, Seminconductor and Composite Materials (ICNSCM 2016).
46. Yuguo Yu, Y. X. Zhang, A novel numerical method for simulations of leaching of cementitious materials in ammonium nitrate solution, The 24th Australasian Conference on the Mechanics of Structures and Materials (ACMSM24), Perth, 6-9 December 2016. Full paper accepted.
47. Yuguo Yu, Y. X. Zhang, Estimation of elastic property of cementitious materials under external sulfate attack, The 24th Australasian Conference on the Mechanics of Structures and Materials (ACMSM24), Perth, 6-9 December 2016. Full paper accepted.
48. Dan Meng, C. K. Lee, Y. X. Zhang, Mechanical behavior of a new PVA-ECC, The 24th Australasian Conference on the Mechanics of Structures and Materials (ACMSM24), Perth, 6-9 December 2016. Full paper accepted
49. Chengjun Liu, Y. X. Zhang, Impact responses of aluminium foam sandwich panels with FML skins, The 24th Australasian Conference on the Mechanics of Structures and Materials (ACMSM24), Perth, 6-9 December 2016. Full paper accepted.
50. He Tian, Y. X. Zhang, Y. H. Cui, C. Yang, Analytical study on material properties of fibre reinforced cementitious composites, The 24th Australasian Conference on the Mechanics of Structures and Materials (ACMSM24), Perth, 6-9 December 2016. Full paper accepted.
51. Chengjun Liu, Y. X. Zhang, High velocity impact behavior of aluminium foam sandwich panels with FML skins, 4th International Conference on Protective Structures (ICPS4), Beijing, China, 18-21 Oct 2016. Paper accepted.
52. Yuguo Yu, Y. X. Zhang, A convertible self-consistent method for evaluation of diffusivity of cement paste, The 12th World Congress on Computational Mechanics and the 6th Asia-Pacific Congress on Computational Mechanics, WCCM XII & APCOM VI, Seoul, Korea, July 24-29, 2016. Full paper (not peer reviewed) accepted.
53. He Tian, Y. X. Zhang, Long-term mechanical properties of a sustainable hybrid fibre reinforced cementitious composite, in: Implementing Innovative Ideas in Structural Engineering and Project Management,

Swapan Saha, Y. X. Zhang, Siamak Yazdani, Amarjit Singh (Eds), ISEC Press, 2015, pp. 645-651.
54. Prabin Pathak, Y. X. Zhang, Nonlinear finite element analysis of FRP strengthened RC beams. in: Implementing Innovative Ideas in Structural Engineering and Project Management, Swapan Saha, Y. X. Zhang, Siamak Yazdani, Amarjit Singh (Eds), ISEC Press, 2015, pp. 463-468.
55. Yuguo Yu, Y. X. Zhang, Modelling the degradation of mechanical properties of cementitious materials under leaching, Proceedings of the Second International Conference on Performance-based and Life-cycle Structural Engineering (PLSE 2015), Dilum Fernando, Jin-Guang Teng, Jose L Torero (Eds), Brisbane, Australia, Dec. 9-11, 2015, pp. 402-411.
56. Xiaoshan Lin, Y. X. Zhang, Chi King Lee, Finite element analysis of FRP-strengthened reinforced concrete panels under blast loading, Design and Analysis of Protective Structures, The 5th International Conference on Design and Analysis of Protective Structures, Singapore, May 19-21, 2015.
57. He Tian, Y. X. Zhang, Tensile behaviour of a sustainable fibre reinforced cementitious composite under different strain rate, in Recent Advances in Structural Integrity Analysis: Proceedings of the international Congress (APCF/SIF-2014), L. Ye. et al. (editors), Sydney, Australia, Dec. 9-11, 2014, pp. 316-320.
58. Ting Huang, Y. X. Zhang, Simulation of material behaviour of ECC under uniaxial tension, in Recent Advances in Structural Integrity Analysis: Proceedings of the international Congress (APCF/SIF-2014), L. Ye. et al. (editors), Sydney, Australia, Dec. 9-11, 2014, pp. 539-543.
59. Chengjun Liu, Y. X. Zhang, Numerical modelling of impact response of aluminium foam/FML sandwich panels, in Recent Advances in Structural Integrity Analysis: Proceedings of the international Congress (APCF/SIF-2014), L. Ye. et al. (editors), Sydney, Australia, Dec. 9-11, 2014, pp 163-167.
60. Hu Chen, Y. X Zhang, Mengyan Zang, Paul J Hazell, An accurate and robust contact algorithm for finite-discrete element modelling, Proceedings of the 11th World Congress on Computational Mechanics, Barcelona, Spain, July 20-25, 2014.
61. Chengjun Liu, Y. X. Zhang, Modelling the mechanical behaviour of aluminium foam using a new RVE model, Proceedings of the 11th World Congress on Computational Mechanics, Barcelona, Spain, July 20-25, 2014.

62. Y. X. Zhang, Zachary S. Kerr, Brain Jarvis, High velocity impact behavior of a new high performance hybrid fibre reinforced cementitious composite, The 7th International Conference on FRP Composites in Civil Engineering (CICE 2014) Vancouver, British Columbia, Canada, August 20-22, 2014.
63. Xiaodan Teng, Y. X. Zhang, Analyses of bond behavior of FRP strengthened RC slabs using a new composite plate element. The 7th International Conference on FRP Composites in Civil Engineering (CICE 2014) Vancouver, British Columbia, Canada, August 20-22, 2014.
64. He Tian, Y. X Zhang, Influence of fly ash and bagasse fibre content on the mechanical properties of a green hybrid fibre-reinforced cementitious composite, 2nd Australasia and South East Asia Conference in Structural Engineering and Construction, Sustainable Solutions in Structural Engineering and Construction, Chantawarangul et al. (editors), Bangkok, Thailand, Nov. 3-7, 2014, pp. 371-376.
65. Ting Huang, Y. X. Zhang, Mechanical properties of a PVA fibre reinforced high performance cementitious composite, 2nd Australasia and South East Asia Conference in Structural Engineering and Construction, Sustainable Solutions in Structural Engineering and Construction, Chantawarangul et al. (editors), Bangkok, Thailand, Nov. 3-7, 2014, pp. 439-444.
66. Chengjun Liu, Y. X. Zhang, Rikard Heslehurst, Experimental study of sandwich panels with aluminum foam core subjected to repeated impact. Proceedings of the Composite Australia and CRC-ACS 2014 Composites Conference, Newcastle, Australia, 7-9 April, 2014.
67. He Tian, Y. X. Zhang, Tensile mechanical properties of a sustainable hybrid fibre reinforced cementitious composite, Proceedings of the Composite Australia and CRC-ACS 2014 Composites Conference, Newcastle, Australia, 7-9 April, 2014.
68. Ting Huang, Y. X Zhang, Parametric effect on mechanical properties of PVA-ECC, Proceedings of the Composite Australia and CRC-ACS 2014 Composites Conference, Newcastle, Australia, 7-9 April, 2014.

In: Reinforced Concrete
Editor: Sharon Robinson
ISBN: 978-1-53610-752-4

Chapter 2

THE MECHANICAL BEHAVIOR MODELING OF REINFORCED CONCRETE STRUCTURES BY THE LUMPED DAMAGE MODEL

Karolinne Oliveira Coelho, Edson Denner Leonel*[*] *and Julio Flórez-López

School of Engineering of São Carlos, Department of Structural Engineering, University of São Paulo, São Carlos, SP, Brazil

ABSTRACT

The nonlinear behavior of reinforced concrete (RC) structures can be represented using the continuum damage models. The goal of this approach is the description of the processes of mechanical damage and the subsequent implementation in structural analysis programs. In continuum damage models, the damage evaluation is carried out across the entire structural domain, which significantly increases the computational effort. Alternatively, lumped damage mechanics allows for an accurate mechanical modeling of non-linear behavior of concrete without representing damage over the total structural area. This theory combines concepts of fracture mechanics with the plastic hinge idea and it can be used accurately in one-dimensional structural elements. In this chapter, this theory is applied to the mechanical analysis of one RC beam and one RC frame. The results are compared with numerical and

[*] Corresponding Author E-mail: edleonel@sc.usp.br.

experimental responses available in the literature. Good agreement is observed among the results shown in the references and those obtained by the lumped damage model.

Keywords: lumped damage, reinforced concrete, finite element method

INTRODUCTION

The concrete is one of the most used materials in the industry. In structural systems, the combination of concrete and steel reinforcement bars gives rise to the reinforced concrete (RC), which is widely applied in the civil engineering field, because of its adequate mechanical strength, durability, fire resistance and easier of forming in complex geometries. Currently, the design of reinforced concrete frames and structures is made considering the elastic behavior. However, in many cases, it is also necessary to consider concrete cracking and reinforcement's yielding, i.e., the inelastic behavior. Thus, for the inelastic mechanical modeling of reinforced concrete, three approaches are currently used: plasticity theory, damage mechanics and fracture mechanics.

The application of elastoplastic criteria was one of the first inelastic approaches used to describe the non-linear mechanical behavior of reinforced concrete. The main drawback of this method consists in the limitations of the plasticity theory in describing correctly the reduction of the mechanical strength after the critical load (negative hardening) and the stiffness degradation process. Therefore, it became necessary the development of new models.

The work of Kachanov [1] is considered the beginning of the classic damage mechanics. Between the 60s and 70s, the continuum damage mechanics developed considerably [2]. However, the models based on continuum damage mechanics had few practical applications. This was due to the lack of convergence, or mesh-dependency, of the damage analyses. Some efforts have been devoted to the solution of such difficulties, such as the development of non-local damage models. However, some of these mathematical adjustments had poor physical basis. Moreover, often the implementation of computational algorithms was complex and inefficient, making difficult the use of such approaches for the analysis of tridimensional structures or with complex geometry and boundary conditions.

Within the framework of continuum damage mechanics, the damage theory developed by Mazars [3] is one of the most frequently used in the analysis of inelastic structural systems. Despite being a simplified approach, the modeling based on the concepts of Mazars damage gives good results, as described in the literature [4-7]. However, such a model requires a fine longitudinal discretization, and, additionally, the division of the cross section in fibers, where each one of them represents the mechanical behavior of steel or concrete. Thus, the computational cost of these models can derail the analysis of complex structures (such as offshore and other industrial structures), or the reliability analysis of structures.

Damage evolution, i.e., the propagation of micro defects in the material, generates consequences on the macro scale through the appearance of cracks. While damage theory aims to quantify the effects of the propagation of micro defects in the material response, fracture mechanics analyzes crack propagation in discrete form. The fracture mechanics theory is consolidated in the inelastic analysis of structures. Thus, it is widely applied in structures with simple geometry and homogeneous material. The description of the propagation of a small number of cracks in a continuum in this context can be carried out successfully [8]. However, in reinforced concrete structures, some complicating factors may prevent its use. For instance, the fact that the concrete is a physically non-linear, heterogeneous, material and the presence of the reinforcement.

Thus, to perform numerical analysis, simplified models can be used if they do not lose the representativeness of the phenomena involved. Lumped damage mechanics is an alternative to the models of the classic damage mechanics. This approach consists in the coupling of damage and fracture mechanics concepts with the plastic hinge idea [9]. Thus, the damage is incorporated into the plastic hinges, which thus become inelastic hinges. These models, although simpler, are efficient and present results as good as those obtained with more complex and refined constitutive equations. In addition, due to the large reduction in computational cost, lumped damage models can be used for the analysis of complex structures, 3D frames, cyclic or impact loadings and reliability analyses.

Several studies show how lumped damage mechanics can be successfully applied in various types of structures as [10-12, 13] evaluated plane frames with lumped damage models. Studies were also conducted in 3D frames, as in the work of [14], and reinforced concrete arches [8, 15]. Good results can also be obtained for cyclic loadings, high cycle fatigue, impact loads or explosion [14, 16].

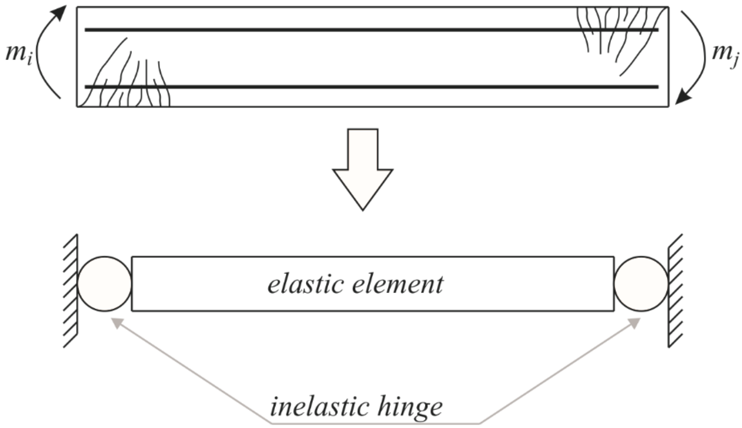

Figure 1. Finite element of RC and the corresponding model of lumped damage.

In this study, a lumped damage model was implemented into a platform of finite elements (FEM). The numerical model was used in the simulation of a beam and a plane frame, which were previously analyzed numerically and experimentally in other works available in the literature. Thus, the force versus displacement curves obtained by lumped damage model are compared with the results described in [17] and [18], and the results of a continuum damage analysis presented by [19]. It was achieved good correlation between the results obtained by the lumped damage model and the responses given in the literature.

LUMPED DAMAGE MODEL

Consider a structural element in RC as shown in Figure 1, which is subjected to bending moments m_i and m_j, applied at its ends *i* and *j*, respectively. It is assumed that concrete cracking and reinforcements' yielding occur at the element ends. Plasticity in the steel rebars is represented by the formation of plastic hinges. It is also considered cracking at the element ends. Then, damage variables are added to the plastic hinges (*di*, *dj*), which will be considered as inelastic hinges [9].

The finite element presents generalized strains that are represented by the matrix Φ shown in Eq. (1).

$$\{\Phi\} = \begin{Bmatrix} \phi_i \\ \phi_j \\ \delta \end{Bmatrix} \tag{1}$$

where ϕ_i e ϕ_j represent relative rotations and δ is the elongation of the element, as illustrated in Figure 2.

The strain equivalence hypothesis [9] states that matrix $\{\Phi\}$ be decomposed into elastic, plastic and damage parts (Eq. (2)), respectively, $\{\Phi_e\}$, $\{\Phi_p\}$ and $\{\Phi_d\}$. It is then assumed that reinforcement's yielding as well as concrete cracking generate relative rotations.

$$\{\Phi\} = \{\Phi_e\} + \{\Phi_p\} + \{\Phi_d\} \tag{2}$$

Generalized stresses, strains, rotations and damage values are computed using kinematic relations, equilibrium and constitutive laws. The latter considers evolution laws of damage and plasticity. Figure 3 shows a flowchart that describes the steps required for the structural analysis using a lumped damage model. Their respective relationships are presented in the following.

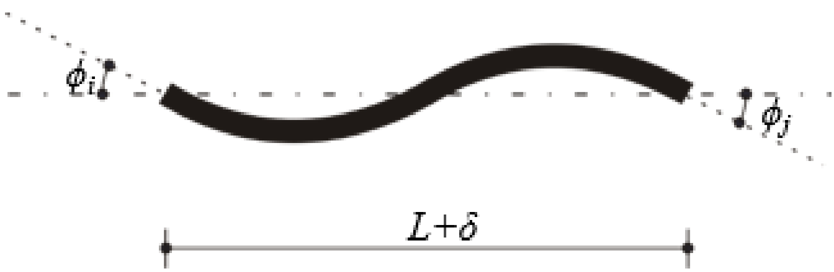

Figure 2. Generalized strains of the finite element.

Consider a finite element for a planar frame with six degrees of freedom, three for each at the two nodes of the element: horizontal displacement u, vertical w and rotation θ. The generalized displacement matrix is built as shown in Eq. (3):

$$\{U\} = \begin{Bmatrix} u_i \\ w_i \\ \theta_i \\ u_f \\ w_f \\ \theta_f \end{Bmatrix} \tag{3}$$

Generalized displacements and strains are related by the kinematic equations that are obtained by geometrical considerations. In the case of plane frame element, this matrix is presented in Eq. (4), [9].

$$\{\Delta\Phi\} = [\mathbf{B}_0]\{\Delta U\} \tag{4}$$

The [B] matrix indicates the kinematic transformation, which is obtained by geometrical relations. Considering the frame finite element, this matrix is defined as follows [9]:

$$[\mathbf{B}_0] = \begin{bmatrix} \frac{\operatorname{sen}(\alpha)}{L} & -\frac{\cos(\alpha)}{L} & 1 & -\frac{\operatorname{sen}(\alpha)}{L} & \frac{\cos(\alpha)}{L} & 0 \\ \frac{\operatorname{sen}(\alpha)}{L} & -\frac{\cos(\alpha)}{L} & 0 & -\frac{\operatorname{sen}(\alpha)}{L} & \frac{\cos(\alpha)}{L} & 1 \\ -\cos(\alpha) & -\operatorname{sen}(\alpha) & 0 & \cos(\alpha) & \operatorname{sen}(\alpha) & 0 \end{bmatrix} \tag{5}$$

where α is the angle between the horizontal direction and the element axis.

The equilibrium equation is presented in Eq. (6) neglecting the nonlinear geometrical and inertia effects.

$$[\mathbf{B}_0]^T \{M(t)\} = \{P(t)\} \tag{6}$$

where P is the nodal forces matrix. Matrix $M(t)$ represents the generalized stress matrix conjugated with Φ.

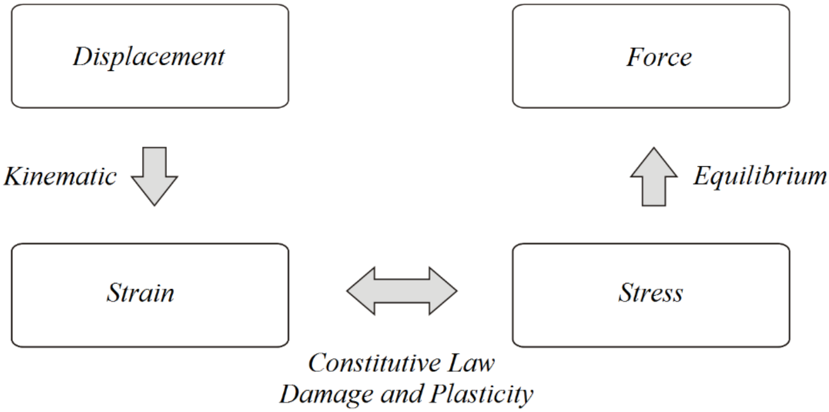

Figure 3. Flowchart for lumped damage analysis.

It includes bending moments at the element ends and the axial force as indicated in Eq. (7).

$$\{M(t)\} = \begin{Bmatrix} m_i(t) \\ m_j(t) \\ n(t) \end{Bmatrix} \tag{7}$$

The constitutive law relates generalized strains and stresses though the matrix expression shown in Eq. (8), [9].

$$\{\Phi - \Phi_p\} = [\mathbf{F}(\boldsymbol{D})]\{M\} + \{\Phi_0\} \tag{8}$$

where [F] is the flexibility matrix of a damaged element and $\{\Phi_0\}$ is the matrix of initial strains.

Considering the strain equivalence hypothesis, the flexibility matrix of a damaged element can be computed by Eq. (9), [9].

$$[\mathbf{F}(\boldsymbol{D})] = [\mathbf{F}_0] + [\mathbf{C}(\boldsymbol{D})] \tag{9}$$

where $[F_0]$ is the flexibility matrix of the elastic element and $[C(D)]$ represents the additional flexibility due to the concrete cracking.

Then, introducing the damage variables for the planar frame d_i and d_j, the flexibility matrix of a damage element can be computed as shown in Eq. (10).

$$[\mathbf{F}(\boldsymbol{D})] = \begin{bmatrix} \dfrac{L}{3EI(1-d_i)} & -\dfrac{L}{6EI} & 0 \\ -\dfrac{L}{6EI} & \dfrac{L}{3EI(1-d_j)} & 0 \\ 0 & 0 & \dfrac{L}{AE} \end{bmatrix} \tag{10}$$

The damage evolution law is based on the energy criterion formulated by Griffith. The generalized Griffith criterion introduces an energy release rate during the crack propagation phase as the derivative of the complementary energy with respect to the damage parameters.

For the frame element, the strain energy is defined as shown in Eq. (11) [14].

$$W_b = \frac{1}{2}\{M\}^T\{\Phi - \Phi_p\} = \frac{1}{2}\{M\}^T[\mathbf{F}(\boldsymbol{D})]\{M\} + \frac{1}{2}\{M\}^T\{\Phi_0\} \tag{11}$$

Therefore, the energy release rates for hinges i and j of the finite element is defined by Eqs. (12) and (13).

$$G_i = \frac{\partial W_b}{\partial d_i} = \frac{Lm_i^2}{6EI(1-d_i)} \tag{12}$$

$$G_j = \frac{\partial W_b}{\partial d_j} = \frac{Lm_j^2}{6EI(1-d_j)} \tag{13}$$

The damage evolution law is obtained by comparing the energy release rate with the crack resistance of the inelastic hinge (see eqs. 14 and 15). They establish a nil damage variation if the energy release rate is lesser than the crack resistance. For damage increments, energy release rate and crack resistance have the same value.

$$\begin{cases} \Delta d_i = 0, \text{ se } G_i < R_i \\ G_i = R_i, \text{ se } \Delta d_i > 0 \end{cases} \tag{14}$$

$$\begin{cases} \Delta d_j = 0, \text{ se } G_j < R_j \\ G_j = R_j, \text{ se } \Delta d_j > 0 \end{cases} \tag{15}$$

The crack resistance function of an inelastic hinge is based on an experimental analysis that relates this parameter with the damage variable. The crack resistance function is given by Eq. (16), [9].

$$R(d) = R_0 + q\frac{\ln(1-d)}{1-d} \tag{16}$$

where R_0 represents an initial resistance.

The second term of the equation describes a gain in resistance due to the presence of the reinforcements, which hinders the propagation of cracks in the concrete.

The parameters R_0 and q depend on the characteristics of the element and is computed from the first cracking and the ultimate moment of the cross-section. It is possible to establish a relationship between damage and bending moment, by making G equal to R, as shown in Eq. (17). It is then obtained the graph presented in Figure 4.

$$m^2 = \frac{6EI(1-d)^2}{L}R_0 + \frac{6qEI}{L}(1-d)\ln(1-d) \tag{17}$$

When the bending moment reaches the value of the critical moment, it is assumed nil damage in the hinge, and with that, the R_0 value is given by Eq. (18).

$$R_0 = \frac{{M_{cr}}^2 L}{6EI} \tag{18}$$

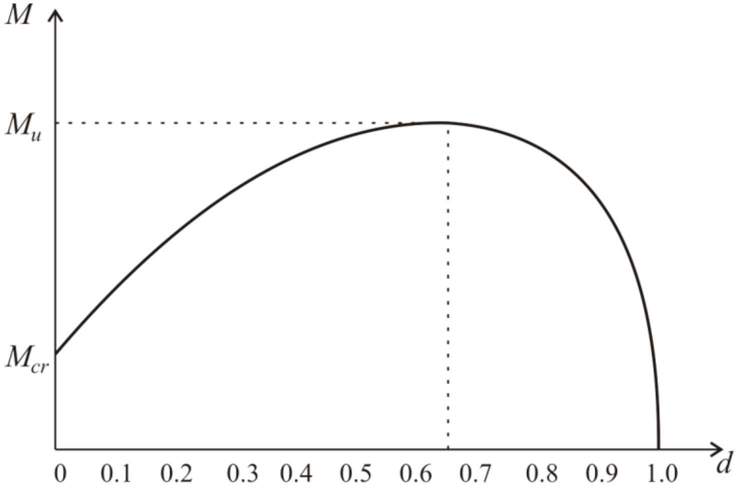

Figure 4. Bending moment as a function of damage.

The value of q is determined by the ultimate moment and its respective damage value. This ultimate damage, as shown in Figure 4, is determined by deriving the function shown in Eq. (17) with respect to the damage variable and equating it to zero.

The plastic strain evolution laws is defined by Eqs. (19) and (20).

$$\begin{cases} d\phi_{p_i} = 0, \text{ se } f_i < 0 \\ f_i = 0, \text{ se } d\phi_{p_i} \neq 0 \end{cases} \tag{19}$$

$$\begin{cases} d\phi_{p_j} = 0, \text{ se } f_j < 0 \\ f_j = 0, \text{ se } d\phi_{p_j} \neq 0 \end{cases} \tag{20}$$

The yield function f includes damage and kinematic hardening. The dependence of the yield function is obtained considering an equivalent moment and the hypothesis of equivalence in strains [9]. Then:

$$f = \left| \frac{m}{1-d} - c\phi_p \right| - k_0 \tag{21}$$

where c and k_0 are element-dependent constants.

In reinforced concrete structures, the first cracking moment is lower than the yield moment. Thus, the values of c and k_0 are computed as a function of the yield damage d_p through the aforementioned relationship (17).

When the value of yield damage is reached, it is assumed that the plastic rotation is nil as well as its the yield function. Thus, it can be observed that k_0 is the effective yield moment as shown in Eq. (22).

$$k_0 = \frac{M_p}{1-d_p} \tag{22}$$

The yield function is also equal to zero when the ultimate bending moment is reached. Therefore, the Eq. (23) is obtained for the computation of the coefficient c as a function of the ultimate plastic rotation.

$$c = \frac{1}{\phi_{p_u}}\left(\frac{M_u}{1-d_u} - \frac{M_p}{1-d_p}\right) \tag{23}$$

APPLICATION 1: RC BEAM, MECHANICAL ANALYSIS

The previously presented lumped damage model was applied in the mechanical analysis of the four-point bending test illustrated in Figure 5.

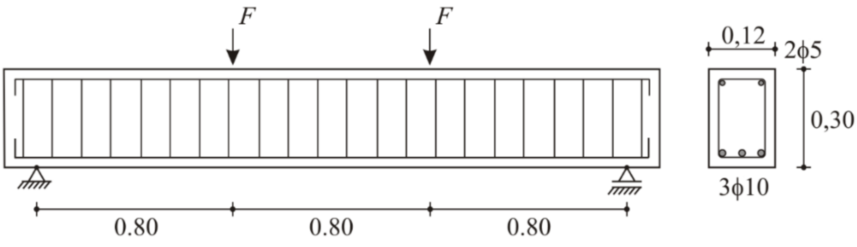

Figure 5. Four-point bending test on a reinforced concrete beam (dimensions in meters).

Table 1. Beam data

Parameter	Variable	Value
Yield stress of steel	f_y (MPa)	500
Elasticity modulus of steel	E_s (MPa)	196000
Elasticity modulus of concrete	E_c (MPa)	29200

The specimen was experimentally tested by [17] and simulated by [19] using the Mazars' damage model. The material parameters presented by [17] are included in Table 1.

The longitudinal reinforcements consisted in Brazilian CA-50 bars with a yield stress of 500 MPa. Plastic hardening was also considered with an ultimate stress equal to $1.1f_y$, i.e., 550 MPa, at an ultimate strain of 0.8%. The transversal reinforcements consisted of ϕ 5 mm bars with a separation of 12 cm. The concrete cover was 1.5 cm. The incremental load used steps of 2 kN. The concrete resistance f_{ck} was equal to 38 MPa. This value was computed with the equation of the elasticity modulus proposed in [20], as shown in Eq. (24).

$$E_c = 4700\sqrt{f_{ck}} \tag{24}$$

The distribution of stresses in the concrete was determined according to [20] (Eq. (25))

$$f_c = f_{ck}\left(2\frac{\varepsilon_c}{\varepsilon_{c0}} - \left(\frac{\varepsilon_c}{\varepsilon_{c0}}\right)^2\right) \tag{25}$$

where ε_{c0} is equal to 0.002 and ε_{cu} is the maximum strain of the concrete given by Eq. (26).

$$\varepsilon_{cu} = \frac{3 + 0,29\,f_{ck}}{145\,f_{ck} - 1000} \tag{26}$$

Once damage and concrete cracking are distributed along the central part of the beam due to the constant bending moment, it is adopted a function to penalize the elastic stiffness of the finite element. [20] suggests that the effective moment of inertia (I_{ef}) be computed as a function of the bending moment applied over the element ends (m) and the first cracking moment (M_{cr}), as shown in Eq. (27).

$$I_{ef} = \left(\frac{M_{cr}}{m}\right) I_{eq} + \left[1 - \left(\frac{M_{cr}}{m}\right)^3\right] I_{ult} \tag{27}$$

where I_{eq} is the inertia moment of the entire cross-section and I_{ult} is the inertia moment corresponding to the ultimate bending moment computed by Eq. (28).

$$I_{ef} = bd^3 \left[\frac{1}{2}k^2\left(1 - \frac{k}{3}\right) + n\rho\beta_c\left(k - \frac{d'}{d}\right)\left(1 - \frac{d'}{d}\right)\right] \tag{28}$$

where b is the cross-sectin thickness, d is the effective height, d' is the distance from the most compressed fiber to the steel bar, ρ is the positive reinforcements ratio, n is the relation between steel and concrete elasticity modulus, k is the position of the neutral axis given by Eq. (29) and β_c is a coefficient defined by Eq. (30).

$$k = \sqrt{(n\rho)^2(1+\beta_c)^2 + 2n\rho\left(1 + \beta_c\frac{d'}{d}\right)} - n\rho(1+\beta_c) \tag{29}$$

$$\beta_c = \frac{m\rho'}{n\rho} \tag{30}$$

where m is another parameter defined as 1 - n and ρ' is the negative reinforcement ratio.

The lumped damage analysis was carried out using a mesh with only four finite elements as shown in Figure 6. The computer program required only 0.140 seconds in a standard desktop to finish the numerical analysis. The results obtained by [19] using the Mazars model required six finite elements with seven Gauss-Lobato integration point across the cross-section height.

Figure 7 presents the curves of force versus displacement at the mid-section of the beam for the experimental results presented in [17], the numerical ones obtained by [19] and the model proposed in this chapter.

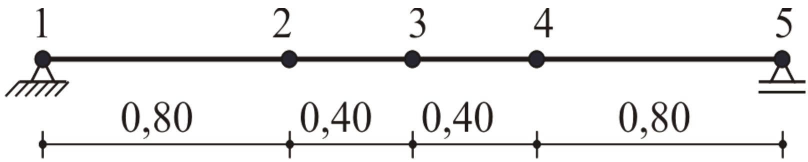

Figure 6. Finite element mesh for the lumped damage analysis.

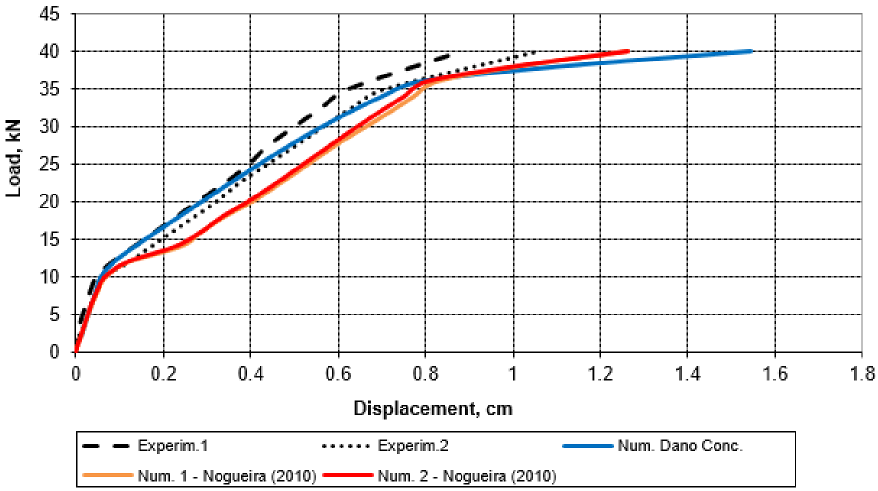

Figure 7. Force x displacements curves for the four-point bending test.

The two damage models are capable to predict accurately the value of the experimental critical load. It is noteworthy that even with the simplifications, the lumped damage model has good agreement with the experimental curve, both during the elastic phase and in the second part of the curve, after the concrete cracking. A better approximation to the experimental curve is observed in the lumped damage model when compared to the Mazars' model. However, in both numerical models, largest displacement values are obtained for collapse after the reinforcements' yielding. This can be attributed to the steel hardening effect, since no experimental data on the ultimate stress and strains values were provided.

APPLICATION 2: RC FRAME, MECHANICAL ANALYSIS

The second application concerns the reinforced concrete frame analyzed experimentally by [18], as shown in Figure 8. In this analysis, two loads of

700 kN at the end of the two columns were firstly applied. Next, it is applied a horizontal displacement *u* at the upper right node of the frame until structural collapse. The parameters presented by [18] are described in Table 2.

Table 2. Frame data

Parameter	Variable	Value
Yield stress of steel	f_y (MPa)	418
Ultimate steel stress	f_{su} (MPa)	598
Elasticity Modulus of Steel	E_s (MPa)	192500
Elasticity Modulus of Concrete	f_{ck} (MPa)	30

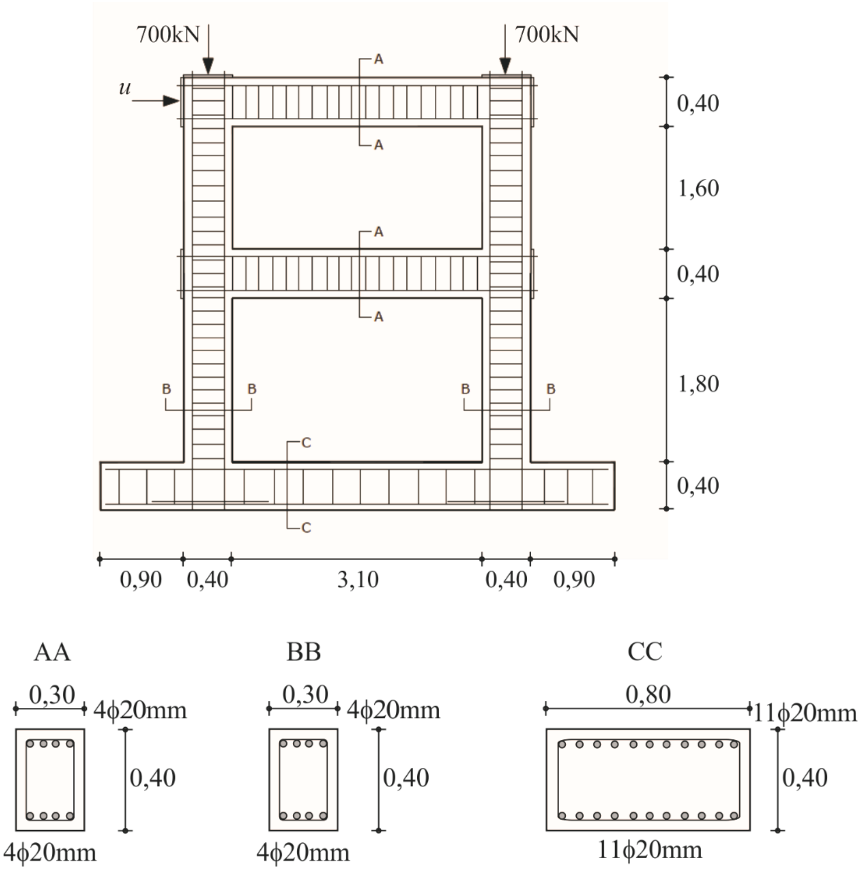

Figure 9. RC frame (dimensions in meters).

In this application, the following values of ultimate strains were adopted: 0.8% for steel and 0.35% for concrete (also computed according to Eq. (26), as in the previous application). The concrete cover in the columns was 3 cm, 2 cm for the beams and 4 cm for the foundation elements. Stirrups in all the cross-sections consisted in ϕ 10 mm bars at each 12.5 cm. The elasticity modulus is calculated as proposed by Eq. (24), and a value of 25743 MPa was obtained.

The finite element mesh for this problem is shown in Figure 9. Only six finite elements are used and the computer program solves the problem in a total time of 1.373 seconds on a standard desktop.

The equilibrium path of node 3, obtained with the lumped damage model, is shown in Figure 10, along with the experimental results [18]. Notice that the numerical simulation is similar to the experimental behavior throughout the charging process.

The equilibrium path of node 2 is also considered, as shown in Figure 11. Note that for this node, the lumped damage model also exhibits results quite close to the experimental response.

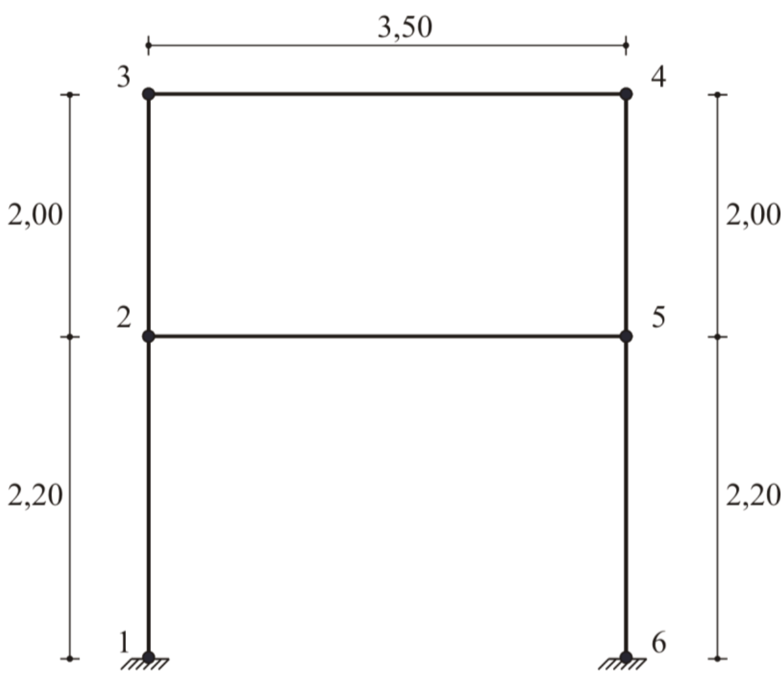

Figure 9. Finite element mesh for the RC frame (dimensions in meters).

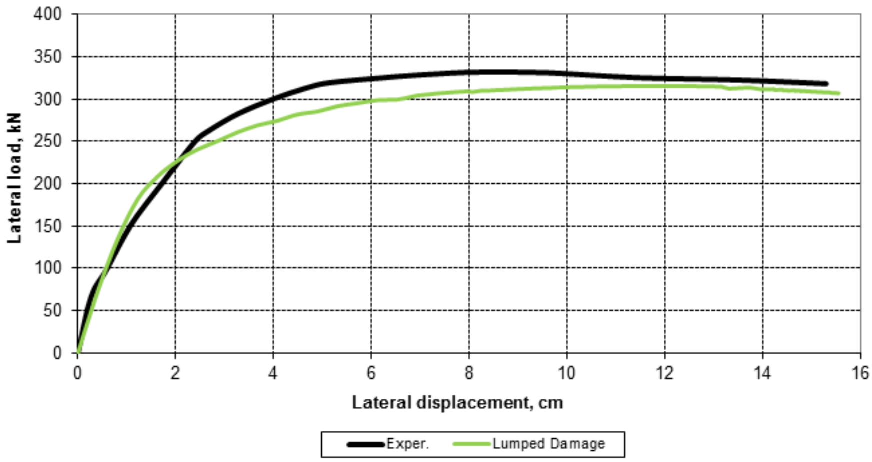

Figure 10. Load x displacement curve. Node 3.

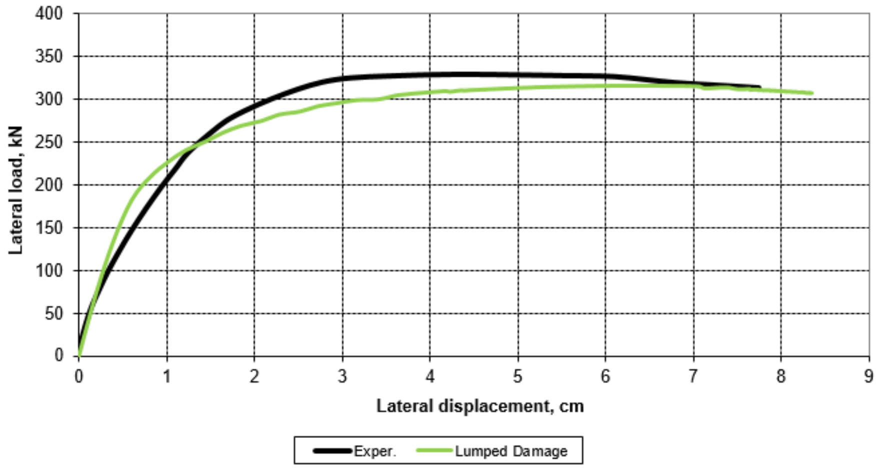

Figure 11. Load x displacement curve. Node 2.

CONCLUSION

This study presented a lumped damage model and its FEM implementation. In the two applications analyzed, the results obtained with the lumped damage model are in good agreement with the experimental and numerical responses available in the literature. In the case of structures that have a stretch of continuous damage, the use of functions that reduce the inertia (stiffness) in combination with the lumped damage provides a good degree of accuracy, as shown in the application 1.

It is also noteworthy that the lumped damage concept leads to meshes with less finite elements and therefore lower computational cost without compromising the results accuracy. This permits the application of models of lumped damage in structures with a higher degree of complexity, allowing the inelastic analysis of problems that have high computational cost if modeled via continuum damage mechanics.

It is intended to apply the model developed in this study in structural reliability analysis. Thus, simulation methods can be applied since the processing time is no longer a limiting factor.

ACKNOWLEDGMENTS

The authors acknowledge the financial support provided by FAPESP, research project Nº 2014/18928-2, without which this study could not have been carried out.

REFERENCES

[1] Kachanov, LM. On the Time to Failure under Creep Conditions, *Izv. Akad. Nauk*. SSR, Otd. Tekhn. n. 8, 26-31, 1958.

[2] Lemaitre, J.; Desmorat, R. Engineering Damage Mechanics. Springer-Verlag; 2005.

[3] Mazars, J. Application de la mechanique de l'endommagement au comportement non lineaire et à la rupture du béton de structure [Application of damage mechanics to nonlinear behavior and fracture of structural concrete], Paris, Thèse de Doctorat d'État, Université Paris 6, 1984.

[4] Légeron, F; Paultre, P; Mazars, J. Damage mechanics modeling of nonlinear seismic behavior of concrete structures. *Journal of Structural Engineering,* 2005, vol. 131, n. 6, pp. 946-955.

[5] Junior, FS; Venturini, WS. Damage modelling of reinforced concrete beams. *Advances in Engineering Software,* 2007, vol. 38, n. 8, pp. 538-546.

[6] Nogueira, C. G., 2010. Desenvolvimento de Modelos Mecânicos, de Confiabilidade e de Otimização para Aplicação em Estruturas de Concreto Armado [Development of Mechanical, Reliability and Optimization Models for Application in Armed Concrete Structures]. Tese de Doutorado, Escola de Engenharia de São Carlos, Universidade de São Paulo.

[7] Pituba, JJC; Lacerda, MMS. Simplified damage models applied in the numerical analysis of reinforced concrete structures. *Revista IBRACON de Estruturas e Materiais*, 2012, vol. 5, n. 1, pp. 26-37.

[8] Amorim, DLDF; Proença, SP; Flórez-López, J. A model of fracture in reinforced concrete arches based on lumped damage mechanics. *International Journal of Solids and Structures*, 2013, vol. 50, n. 24, pp. 4070-4079.

[9] Flórez-López, J; Marante, ME; Picón, R. Fracture and Damage Mechanics for Structural Engineering of Frames: State-of-the-Art Industrial Applications. IGI Global; 2015.

[10] Cipollina, A; López-Inojosa, A; Flórez-López, J. A Simplified damage mechanics approach to nonlinear analysis of frames. *Computers and Structures*, 1995, vol. 54, n. 6, pp. 1113-1126.

[11] Flórez-López, J. Frame analysis and continuum damage mechanics. *European Journal of Mechanics – A/Solids*, 1998, vol. 17, n. 2, pp. 269-283.

[12] Rajasankar, J; Nagesh, R; Prasad, A. Modelling inelastic hinges using CDM for nonlinear analysis of reinforced concrete frame structures. *Computers and Concrete*, 2009, vol. 6, n. 4, pp. 319-341.

[13] Alva, GMS; El Debs, ALHC. Application of lumped dissipation model in nonlinear analysis of reinforced concrete structures. *Engineering Structures*, 2010, vol. 32, n. 4, pp. 974-981.

[14] Marante, ME; Flórez-López, J. Three-dimensional analysis of reinforced concrete frames based on lumped damage mechanics. *International Journal of Solids and Structures*, 2003, vol. 40, n. 19, pp. 5109-5123.

[15] Amorim, DLDF, Proenca, SP, Florez-Lopez, J. Simplified modeling of cracking in concrete: Application in tunnel linings. *Engineering Structures*, 2014, vol. 70, 23-35.

[16] Febres, R; Inglessis, P; Flórez-López, J. Modeling of local buckling in tubular steel frames subjected to cyclic loading. *Computers and Structures*, 2003, vol. 81, n. 22-23, pp. 2237-2247.

[17] Álvares, M. da S., 1993. Estudo de um modelo de dano para o concreto: formulação, identificação paramétrica e aplicação com o emprego do

método dos elementos finitos [Study of a damage model for concrete: formulation, parametric identification and application using the finite element method]. Tese de Doutorado, Escola de Engenharia de São Carlos, Universidade de São Paulo.

[18] Vecchio, FJ; Collins, MP. The modified compression-field theory for reinforced concrete elements subjected to shear. *ACI Structural Journal*, 1986, vol. 83, n. 2, pp. 219-231.

[19] Nogueira, CG; Venturini, WS; Coda, HB. Material and geometric nonlinear analysis of reinforced concrete frame structures considering the influence of shear strength complementary mechanisms. *Latin American Journal of Solids and Structures*, 2013, vol. 10, n. 5, pp. 953-980.

[20] ACI Committee, American Concrete Institute, and International Organization for Standardization, 2008. *Building code requirements for structural concrete (ACI 318-08) and commentary*, American Concrete Institute.

In: Reinforced Concrete
Editor: Sharon Robinson

ISBN: 978-1-53610-752-4

Chapter 3

MECANO-PROBABILISTIC ASSESSMENT OF REINFORCED CONCRETE STRUCTURES SUBJECTED TO REINFORCEMENTS' CORROSION TRIGGERED BY CARBONATION AND CHLORIDE PENETRATION

Karolinne Oliveira Coelho and Edson Denner Leonel*

School of Engineering of São Carlos, Department of Structural Engineering, University of São Paulo, São Carlos, SP, Brazil

ABSTRACT

This study aims the mecano-probabilistic modelling of reinforced concrete structures subjected to reinforcements' corrosion. The corrosion time initiation due to the carbonation or the chloride penetration is assessed by diffusion approaches. The tree of failure is utilized for determining the probability of individual and global failure modes. The structural mechanical resistance is evaluated according to the Brazilian design code NBR 6118/2014. The penalizations over the reinforcements' cross section area and over its yield stress, both caused by the corrosion process, are accounted. The loading is modelled by the extreme value process. Probability of failure curves for the corrosion time initiation; mechanical failure and reinforcements' steel loss along time are

* Corresponding Author E-mail: edleonel@sc.usp.br.

presented. In addition to the assessment of the probability of individual failure modes, the progressive collapse paths along 50 years are analysed. The results obtained show that relevant changes on the predominant mechanical failure mode occur along time. Moreover, major values for the reinforcements' steel loss and the probability of mechanical collapse are observed at the end of 50 years, even accounting for the design code recommendations.

Keywords: reinforcements' corrosion, carbonation, chloride ingress, structural reliability

INTRODUCTION

The performance of reinforced concrete structures may become inadequate during its service life due to the pathological manifestations. Several phenomena trigger these pathologies. Among them, it is worth mentioning the reinforcements' corrosion. The corrosion is a chemical or electrochemical process of material degradation caused by an external agent [1]. Large efforts have been dedicated by public and private sectors over the last years for maintaining and repairing reinforced concrete structures [2, 3]. The costs with inspection, maintenance and repair on structures subjected to corrosion processes vary between 3% to 4% of the Gross Domestic Product (GDP) in industrialized countries and overcome US$ 1.8 trillion worldwide [3, 4]. In Brazil, the monetary loss caused by the corrosion in the structural context overcome US$20.79 billion/year [1, 4].

The reinforcements are chemically protected by the passivating layer, which is chemically stable due to the PH of the aqueous solution at the concrete pores. However, the presence of CO_2, in carbonation case, or Cl, in chloride ingress case, affects the chemical stability of such passivating layer [5]. The diffusion of CO_2 into concrete pores triggers carbonation reactions with sodium, potassium and mainly calcium cations. These chemical reactions create the carbonation front, in which the concrete PH is reduced from 14 to 9 approximately. When the front reaches the reinforcements, the depassivation process occurs and uniform corrosion starts [6]. On the other hand, the corrosion triggered by chloride ingress starts when the chloride concentration at the passivating layer reaches the threshold value. In such a case, punctual destabilizations at the passivating layer appear. Then, the corrosion occurs in a punctual form named as pits [7]. The corrosion process in reinforced concrete structures leads to the reduction of rebar's cross section and to the reduction of the rebar's yield stress value. Moreover, the expansive chemical components produced during the corrosion cause concrete cracking, rebar's adherence loss and, in advanced stages, the spalling [8].

Several approaches have been presented in the literature for handling the corrosion in reinforced concrete structures. Most of them propose deterministic methods and analysis procedures for simplified type of structures. However, the corrosion phenomenon in reinforced concrete structures is only addressed properly through probabilistic approaches. Uncertainties are inherent in such a problem. Moreover, the uncertainties have major importance on the mechanical performance assessment [9-11].

Many efforts have been dedicated to the modelling of corrosion triggered by carbonation. Several experimental studies are observed in the literature. In addition, analytical models were proposed accounting for these experimental data. An experimental study of carbonation is presented in [12]. The carbonation front for one exposed structural surface was analysed and experimental data were presented. The authors emphasize the large randomness into the data obtained. The influence of the global climatic change on the carbonation phenomenon is studied by [13], which emphasizes the importance of this engineering problem for the society worldwide. A numerical model for CO_2 diffusion is presented by [14]. The results obtained were compared with references data. A numerical approach is introduced by [15] aiming the description of random damage fields in reinforced concrete structures subjected to reinforcements' corrosion. The salt induced corrosion was considered in the study. A mathematical-numerical model of carbonation process in reinforced concrete structures is presented in [16]. Analytical equations were applied and random fields were described. An analytical technique for carbonation prediction in early-aged cracked concrete is presented by [17]. The CO_2 diffusion of pore water in sound concrete and in cracked concrete were considered.

Several researchers worldwide have studied the reinforcements' corrosion triggered by chloride penetration. In this context, [15] proposed a probabilistic model for reinforcements' corrosion in bridges beams. The influence of the temperature and the moisture on the chloride diffusion into concrete pores was studied by [18], which proposed an approach for this purpose. The mechanical degradation processes caused by reinforcements' corrosion, concrete cracking and bio deterioration agents are studied by [19] taking into account uncertainties. The mechanical degradation of the concrete cover caused by corrosion processes in non-cracked stages and in partially cracked stages is analysed by [20]. The mechanical behaviour of reinforced concrete girders as a function of time is represented by the model proposed in [21]. In such a model, the Fick's law represents the chloride diffusion along time, empirical laws were adopted for quantifying the reinforcements' cross section loss and the Monte Carlo simulation method applied to carry out the probabilistic analysis. The assessment of the probabilistic corrosion time initiation was performed by [22, 23], which utilized the coupling of Fick's law and reliability approaches. In this study, the influence of uncertainties associated to the concrete cover depth, environment aggressiveness and water-cement ratio on the probability of structural service life failure was analysed. Moreover, interaction abacuses were proposed in order to determine proper values of concrete cover according to inspection/maintenance time fixed a priori. A deterministic mechanical model is proposed by [24] for the durability assessment of reinforced concrete structures subjected to reinforcements' corrosion. This model is based on the coupling of Fick's law, damage mechanics and elastoplastic criteria, which were included in a robust finite element code.

In the present study, probabilistic analyses involving corrosion time initiation, reinforcements' cross section reduction and mechanical collapse of hyperstatic beams due to carbonation and chloride ingress are presented. The corrosion time initiation is modelled by the Fick's diffusion approach for the chloride ingress case [25]. Such a time is assessed by the diffusion approach introduced by [26] for the carbonation case. Thus, the parameters related to the concrete-mix design and, consequently, to the concrete porosity have major importance in this analysis.

The reinforcements' cross section reduction and the reinforcements' yield stress reduction during the corrosion are represented by empirical approaches, which were previously introduced in the literature [27]. The reinforcements' corrosion process is triggered differently by carbonation and chlorides ingress, as previously mentioned. Thus, different approaches were utilized for the modelling of these effects. For carbonation case, the approaches presented by [28] were utilized whereas for chloride ingress case the approaches introduced by [29] were applied.

Finally, the evolution of the probability of mechanical failure along time for hyperstatic beams is studied. The model utilized accounts for the mechanical degradation mechanisms caused by the corrosion process. The mechanical model adopted is based on the equilibrium assumptions provided by the NBR 6118/2014 [30]. Moreover, the external loading is described by the extreme value process [31, 32], thus, it is not constant along time. This loading modelling assumption is one contribution of this study. In addition, the evolution of the probability of individual failure modes and the global failure mode along time is studied. The predominant failure path is determined along time, which is another contribution of the present study. The results obtained show that the predominant mechanical failure path change along time due to the corrosion effects. Therefore, failure modes do not predict in the design phase may occur due to the corrosion. This study contributes to the modelling and prediction of the probabilistic mechanical behaviour of reinforced concrete structures subjected to reinforcements' corrosion. Moreover, this study contributes to the comprehension of the mechanical effects caused by the corrosion into the mechanical structural resistance.

CORROSION TIME INITIATION MODELLING

The reinforcements' corrosion triggered by chloride ingress starts when the chloride concentration at the passivating layer that surrounds the reinforcements reaches the threshold value. Thus, punctual destabilization along the passivating layer occurs and pit corrosion is observed. The chemical reactions involved in this corrosion type have large randomness [5]. Especially, the threshold value for the chloride concentration [33], which may vary from 0.1% to 1.96% of the mortar volume. The randomness observed in the corrosion triggered by chloride ingress occurs because such phenomenon depends on the water cement ratio (w/c), the chemical composition of cement, chemical composition of steel and the environmental effects such as temperature and moisture, which are inherent random. In the Brazilian territory, the reinforcements' corrosion caused by chlorides is critical at the coastal regions. Thus, the chloride disperse into the environment is another important random parameter involved in this problem. To determine the concentration of the disperse chlorides into the environment, recent studies have been developed in Brazil as presented by [34] in Fortaleza, [35] in João Pessoa and [36] in Maceió.

The chloride diffusion into concrete pores is modelled by the non-steady state approach provided by the second Fick's law. Fick's laws for diffusion are applicable for homogeneous, isotropic and inert materials. Moreover, the mechanical properties related to the diffusion process are assumed as identical along all directions and kept constants along time. These hypotheses are not completely satisfied for concrete case because such a material is well known heterogeneous, anisotropic and chemically reactive. However, the methods commonly adopted for chlorides transportation modelling in concrete consider this process as governed only by the ionic diffusion. Thus, it assumes that the concrete cover is completely saturated. Therefore, it makes the hypotheses of Fick's laws acceptable for the chloride ingress modelling because, in this case, the material is assumed as completely saturated with unidirectional chloride flux, i.e., from the exterior surface to the concrete depth [37]. The Fick's law represents the diffusion problem through the following equation:

$$\frac{\partial C}{\partial t} = \frac{\partial}{\partial x}\left(-D \frac{\partial C}{\partial x} \right) \tag{1}$$

The solution for the equation previously presented is given by:

$$cob = 2\mathrm{erfc}^{-1}\left[\frac{C_{\mathrm{lim}}}{C_0} \right] \sqrt{D t_{\mathrm{ini}}} \tag{2}$$

in which C_{lim} is the threshold chloride concentration, C_0 indicates the chloride concentration at the structural surface, D is the chloride diffusion coefficient, cob represents the concrete cover depth and t_{ini} is the time for corrosion initiation.

The chloride diffusion coefficient required to solve Eq. (1) can be determined by different methods. Empirical approaches may be applied, as presented by [38], as well as electrochemical analyses, as introduced by [39]. Numerical method may be applied to solve Eq. (1) [40]. In such case, the parameters that govern the problem are assumed as time dependent. The model adopted in this study for obtaining the chloride diffusion coefficient is introduced by [25]. This model is based on experimental data and its prediction relates D to the concrete-mix design parameters as presented in Eq. (3).

$$D = D_{H_2O} 0.15 \frac{1 + \varrho_c \left({}^{w}\!/_{c} \right)}{1 + \varrho_c \left({}^{w}\!/_{c} \right) + \frac{\varrho_c}{\varrho_{ag}} \left({}^{ag}\!/_{c} \right)} \left(\frac{\varrho_c \left({}^{w}\!/_{c} \right) - 0{,}85}{1 + \varrho_c \left({}^{w}\!/_{c} \right)} \right)^3 \tag{3}$$

in which D_{H2O} indicates the chloride diffusion coefficient into an infinite solution, whose value is $1.6.10^{-5}$ cm²/s for NaCl. ρ_c is the concrete density and

ρ_{ag} the aggregate density, *w*/*c* represents the water/cement rate and *ag*/*c* represents the aggregate/cement rate.

The concrete is a high alkalinity media due to the presence of hydroxides of sodium, potassium and calcium. The CO_2 penetrates into concrete pores and reacts with these alkaline composites. As a result, carbonate salts are produced. These reactions are named carbonation, which reduce the concrete PH from 14 to 9, approximately [6, 41]. The PH reduction causes the loss of the chemical passivating layer that surrounds the reinforcements. Thus, in this case, uniform corrosion is triggered. This type of corrosion is observed commonly in underground parkings, bridges and tunnels, for instance. Moreover, the CO_2 concentration may reach 0.3% in global metropolis. In exceptional conditions this concentration may reach 1% [6, 42].

Several approaches have been proposed in the literature to represent the CO_2 diffusion into concrete pores [43, 44]. However, these approaches require chemical parameters from the concrete, which have complex obtaintion in real applications in civil engineering. Therefore, the CO_2 diffusion process is modelled commonly by the approach presented in [26], which is based on the association of the Fick's diffusion law and empirical data calibration. This approach requires the parameters related to the concrete-mix design. Thus, the determination of the time for corrosion initiation by this approach follows Eq. (4):

$$cob = 0.35\varrho_c \frac{w/c}{\left(1+\frac{\varrho_c w/c}{1000}\right)} + RH\sqrt{\left(1+\frac{\varrho_c w/c}{1000}+\frac{\varrho_c ag/c}{\varrho_{ag}}\right)C_{CO_2}\frac{22.4}{44}10^6 t_{ini}} \tag{4}$$

in which *RH* is the relative air moisture, C_{CO2} is the CO_2 concentration in the environment.

PROBABILITY OF FAILURE IN STRUCTURES SUBJECTED TO CORROSION PHENOMENON

The limit state function describes a structural problem by involving the material resistance and the external loading. Both variables are random ***X***, as illustrated in Eq. (5) [45]:

$$g(\boldsymbol{X}) = \mathrm{R}(\boldsymbol{X}) - S(\boldsymbol{X}) \tag{5}$$

The probability of failure in the structural context can be defined as the probability of the structural system do not accomplish one or more than one design requirements [45]. Therefore, the failure is characterized when $g(\boldsymbol{X})$ becomes lesser than zero.

$$P_f = P\left[g(\boldsymbol{X}) \leq 0\right] \tag{6}$$

In the present study, the mechanical structural resistance is determined by the equilibrium equations presented in [30]. Bending and shear resistances are accounted. Moreover, the reinforcements' cross section reduction and the reduction on the reinforcements' yield stress along time due to the corrosion process are accounted. In addition, the external loading is represented by the extreme value process.

RESISTANCE

The corrosion process leads to the mechanical degradation over the reinforcements' steel. Consequently, the reinforcements' cross section reduces after the time for corrosion initiation. Such reduction is determined by the corrosion rate, which indicates the velocity that corrosion reactions occur. This parameter is calculated differently for carbonation and chloride corrosion types.

The uniform corrosion is observed during the corrosion processes triggered by CO_2. For the carbonation mechanism, the diameter reduction is calculated as presented in Eq. (7), [27]:

$$\Delta d = 0.0232 i_{corr} \left(t - t_{ini}\right) \tag{7}$$

in which i_{corr} is the corrosion rate (μ/mm²), Δd is the reduction on the reinforcements' diameter and t is the actual time instant in years.

The carbonation reactions, and consequently the corrosion rate, are affected by the temperature, T. Therefore, for the carbonation case, the i_{corr} may be evaluated as proposed by [28]:

$$i_{corr} = i_{corr\text{-}20}\left(1+K_C\left(T - 20\right)\right) \tag{8}$$

in which $i_{corr\text{-}20}$ is the corrosion rate at 20ºC and K_C represents a coefficient equal to 0.025 if $T \leq 20$ºC or 0.073 if $T > 20$ºC.

For pitting corrosion, the reinforcements' cross reduction is determined by calculating the pit's cross-sectional area, given by Eq. (9) [27, 29].

$$A_{pit}(t) = \begin{cases} A_1 + A_2 & \text{if } p(t) \leq \dfrac{d_0}{\sqrt{2}} \\ \dfrac{\pi d_0}{4} - A_1 + A_2 & \text{if } \dfrac{d_0}{\sqrt{2}} < p(t) \leq d_0 \\ \dfrac{\pi d_0}{4} & \text{if } p(t) \geq d_0 \end{cases} \tag{9}$$

where:

$$b = 2\,p(t)\sqrt{1-\left(\frac{p(t)}{d_0}\right)^2} \tag{10}$$

$$A_1 = 0.5\left[\theta_1\left(\frac{d_0}{2}\right)^2 - b\left[\frac{d_0}{2} - \frac{p(t)^2}{d_0}\right]\right] \tag{11}$$

$$A_2 = 0.5\left[\theta_2\, p(t)^2 - b\,\frac{p(t)^2}{d_0}\right] \tag{12}$$

$$\theta_1 = 2\arcsin\left(\frac{b}{d_0}\right) \tag{13}$$

$$\theta_2 = 2\arcsin\left(\frac{b}{2\,p(t)}\right) \tag{14}$$

$$p(t) = 0.0116 i_{corr} R t \tag{15}$$

in which d_0 is the initial rebar diameter, $p(t)$ is the pit depth, b is the pit width and R is the pitting factor (ratio between the maximum pit depth and the corrosion penetration) adopted as 5.08 [27, 29].

The i_{corr} value is evaluated using the *w/c* rate for corrosion processes triggered by chloride ingress [46]. Then:

$$i_{corr} = \frac{37.8\left(1 - {}^{w}\!/_{c}\right)^{-1.64}}{cob} \tag{16}$$

where cob is the concrete cover value in cm.

The degradation on the reinforcements' yield stress is evaluated by the approach presented in [29]. This empirical approach recommends that the yield stress be penalized by the following equation:

$$\overline{f_y} = \left[1 - 0.005\left(\frac{0.046 i_{corr}\left(t - t_{ini}\right)}{d}\right)\right] f_y \tag{17}$$

in which f_y and $\overline{f_y}$ represents the yield stress before and during the corrosion process, respectively.

In this study, the mechanical structural resistance is assessed by the recommendations of the Brazilian design code [30]. Obviously, the reinforcements' cross section reduction and reinforcements' yield stress reduction are accounted by the Eq. (7), Eq. (8) and Eq. (9).

The resistant bending moment is determined by enforcing equilibrium conditions along the structural cross section. Therefore, assuming a rectangular cross section, such a moment is determined as follows:

$$M_d = 0.68 b x f_{cd}\left(d - 0.4x\right) \tag{18}$$

in which M_d is the resistant bending moment, b is the cross section thickness, f_{cd} is the compressive concrete resistance, d is the distance between the tensile reinforcement and the cross section top and x is the neutral axis position.

The equilibrium of forces, which involves the concrete and reinforcements resultant of forces, leads to the determination of the neutral axis position. Then:

$$x = 1,25d\left[1 - \sqrt{\frac{M_d}{0,425bd^2 f_{cd}}}\right] \tag{19}$$

$$\xi = \frac{x}{d} \tag{20}$$

When the cross section is on the domain 3 of strain [30], ξ varies from 0.628 to 0.259 for CA-50 steel. In such a case, the resistant bending is the following:

$$M_d = f_{yd} A_s \left(d - 0,4x\right) \tag{21}$$

in which f_{yd} is the reinforcements' yield stress and A_s the reinforcements' cross section area. During the corrosion process, both variables vary along time.

On the other hand, when the cross section is on domain 4 of strain [30], the compression reinforcements' resistance is accounted. Thus, the resistant bending moment is composed by the bending moment on domain 3 and 4 (M_{34}), in addition to the bending moment due to the compression reinforcements (M_2). Thus, one defines:

$$M_d = M_{34} + M_2 \tag{22}$$

$$M_{34} = f_{yd} A_{s34} \left(d - 0,4x_{34}\right) \tag{23}$$

$$M_2 = f_{yd} A_s' \left(d - d'\right) \tag{24}$$

The resistant shear effort is determined by the coupling of two mechanisms. The first is named complementary truss mechanism (V_c) and the second transversal reinforcements' mechanism (V_{sw}). These mechanisms depend on the design model chosen, model I or model II, which are described in [30].

The model I assumes that the angle between the compression concrete struts is fixed in 45º. Therefore, in such a model V_c is constant. As a result, V_c and V_{sw} are determined as follows:

$$V_c = 0.6 a_{v2} f_{ctd} b_w d \tag{25}$$

$$V_{sw} = \left(\frac{A_{sw}}{s}\right) 0.9d\, f_{ywd} \left[sen\left(a\right) + cos\left(a\right) \right] \tag{26}$$

in which A_{sw} is the transversal reinforcements' cross section area and s indicates the transversal reinforcements' spacing. α is the angle between the transversal reinforcements axe and the structural axe, which may vary from 45º to 90º. f_{ywd} represents the transversal reinforcements yield stress, which is equal to f_{yd}, for stirrups, or 0.70 f_{yd} and limited to 435 MPa for bent reinforcements. Finally, α_{v2} is defined as follows:

$$a_{v2} = 1 - \frac{f_{ywd}}{250} \tag{27}$$

in which f_{ywd} in (MPa)

On the other hand, the model II assumes that the angle between the compression concrete struts may vary from 30º to 45º. Consequently, V_c varies according to the value of V_{sw}. In such a case, the resistant shear effort is evaluated as follows:

$$\begin{cases} V_c = V_{c0} = 0.6 f_{ctd} b_w d & \text{if } V_{sd} \leq V_{c0} \\ V_c = 0 & \text{if } V_{sd} = V_{Rd,II} \end{cases} \tag{28}$$

$$V_{sw} = \left(\frac{A_{sw}}{s}\right) 0.9d\, f_{ywd} \left[\mathrm{cotg}\left(a\right) + \mathrm{cotg}\left(\theta\right) \right] \mathrm{sen}\left(a\right) \tag{29}$$

in which θ is the angle between the compression concrete struts and $V_{Rd,II}$ indicates the maximum stress along the compression concrete struts, which is evaluated by the following equation:

$$V_{Rd,II} = 0.54 a_{v2} f_{cd} bd \left[\text{sen}^2 \left(\theta \right) \right] \left[\text{cotg} \left(a \right) + \text{cotg} \left(\theta \right) \right] \tag{30}$$

LOADING PROCESS

The Brazilian design code for reinforced concrete structures [30] predicts as service life 50 years for usual reinforced concrete structures. Therefore, the assumption of time-constant load in its maximum value during a reliability analysis over the entire structural service life is unreal. Thus, to represent in a real form the loading process in time dependent problems the extreme value process is utilized.

The cumulative maximum distribution function for a sampling of n random variables is defined as follows [31]:

$$F_{Y_n}(y) = \left[F_X(y) \right]^n \tag{31}$$

in which $F_X(y)$ indicates the function of cumulative distribution.

The extreme distribution presented above tends to limiting forms as n becomes higher. Such forms are named as asymptotic extreme distribution, which may be classified as: Gumbel, Frechet and Weibull (types I, II e III, respectively), according to the type of the original distribution assumed $F_X(y)$ [32].

In the present study, the accidental loading is represented by the Gumbel distribution for maximum, which cumulative probability function is defined as follows [31]:

$$F_X(x) = \exp\left[-\exp\left[-\omega \left(x - u_n \right) \right] \right] \tag{32}$$

in which ω represents the form parameter and u_n the maximum characteristic value given by Eq. (33) and Eq. (34). μ and σ indicate the mean and standard deviation, respectively.

$$\omega = \frac{\pi}{\sqrt{6}\sigma} \tag{33}$$

$$u_n = \mu - \frac{0,577216}{\omega} \tag{34}$$

The maximum characteristic of a given extreme distribution is defined as follows:

$$F_X(u_n) = \mathrm{P}\left[\left\{X \leq u_n\right\}\right] = 1 - \frac{1}{n} \tag{35}$$

Consequently, the maximum characteristic value for 50 years is known, i.e., such a value for the structural service life is defined. Then, the characteristic values for any other time *n* is achieved by utilizing the Eq. (34) and Eq. (32). Thus, the Eq. (36) is obtained:

$$u_n = u_{50} + \ln\left(-\ln\left(\frac{50 - n}{50}\right)\right)^{1/\omega} \tag{36}$$

MONTE CARLO SIMULATION

The Monte Carlo simulation method is a numerical simulation procedure widely utilized for solving reliability problems. In such a simulation method, a sampling of random variables is applied for describing the failure and the safe spaces. The sampling is constructed accounting for the statistical distribution assigned for each random variable in the problem. In time dependent problems, the sampling is assessed at each time step. The Monte Carlo approach deals the simulation of the limit state function. Therefore, the spaces' description and the probabilities of failure are accurately achieved as larger be the sampling adopted.

The structural failure is observed when the sampling points lead to the failure domain. Otherwise, safety condition is observed. The series schemes define failure if at least one limit state function be violated. Otherwise, the parallel schemes define failure when a set of critical limit state functions is violated. These sets of limit state functions are defined taking into account the structural system and the failure paths available. Optimization approaches, such as the First Order Reliability Method (FORM) and the Second Order Reliability Method (SORM), can be adopted for assessing the probability of failure. These approaches are based on the determination of the reliability index, which is associated to the probability of failure. The probability of failure is calculated, for the Monte Carlo simulation, using the following equation [46]:

$$P_f = \int_{\Omega} I[x] \mathrm{f}_X(x) \mathrm{d}x = \frac{1}{n_t} \sum_{j=1}^{n} I[x_j] = \frac{n_f}{n_t} \tag{37}$$

in which n_t is the range sampling and n_f the number of failures observed. $I[x]$ is 1 for failure condition and nill for safe condition.

It is worth mentioning that Monte Carlo requires a large number of limit state function simulations when the probability of failure is small. This is a disadvantage of this approach. In such a case, the computation cost becomes this approach non-recommended. Nevertheless, this method is applied in the present study once the limit states accounted are described analytically.

In general structural systems or even in individual structural elements more than one failure mechanism may lead to the structural failure. Therefore, the probability of failure in such cases is addressed consistently by the system reliability approach. This approach aims at identifying and systematizing the failure modes paths. Then, the probability of structural failure is achieved by the sum of the probability of failure of each failure mode path. For this purpose, the tree of failure has to be constructed, which divides the failure modes as series or parallel schemes [47]. In series failure modes, the failure of one link leads to the structural failure. On the other hand, in parallel failure modes, the structural failure is characterized by the failure of all parallel links. Isostatic structures are classified as series system whereas hyperstatic structures are classified as parallel system, for instance.

APPLICATIONS

In the present study, fourteen random variables describes the environmental, mechanical and geometrical characteristics of the structural system. The environmental conditions for both carbonation and chloride ingress corrosions are assumed as high aggressiveness, as presented in Table 1. The chloride concentration values at the structural surface are based on [34], which present such a concentration for the coastal regions of Fortaleza and Maceió. The statistical properties for the threshold chloride concentration at the reinforcements' interface are based on [33]. For the corrosion triggered by carbonation, the structure is assumed as placed into an industrial region, i.e., the CO_2 concentration at the atmosphere is assumed as higher than 0.3% [42].

The permanent load is described by the Gaussian distribution whereas the variable load is described by the Gumbel distribution for maximum [11]. The reinforcements' steel is the CA-50, with coefficient of variation of 10% [11]. The variables *ag/c* and aggregate density are assumed as deterministic, which value are 5 and 2560 kg/m³, respectively.

The time for corrosion initiation is analysed in three different scenarios, named (a), (b) and (c). The difference among them concerns the characteristic concrete resistance, f_c, the *w/c* rate and the concrete cover value, as presented in Table 2.

For the first case, (a), mean values are adopted for the three variables mentioned in order to attend the recommendations of [30]. On the other hand, the cases (b) and (c) account for higher values of *w/c* rate and lower values for the characteristic concrete resistance in order to analyse the influence of these parameters on the time for corrosion initiation.

Table 1. Random variables used in reliability analysis

Parameter	Distribution	Mean	Standard Deviation
f_y (MPa)	Lognormal	500	50
Relative Moisture (%)	Normal	60	12
Temperature (ºC)	Uniform	30	10
$i_{corr\text{-}20}$ (μA/cm²)	Lognormal	0.431	0.259
CO_2 (%)	Lognormal	0.5	0.5
C_{lim} (kg/m³)	Lognormal	0.403	0.088
C_0 (kg/m³)	Lognormal	0.773	0.214
g_1 (kN/m)	Normal	3.125	0.391
q_1 (kN/m)	Lognormal	20	4.30
g_2 (kN/m)	Normal	3.125	0.391
q_2 (kN/m)	Lognormal	7.5	1.63

Table 2. Random variables and cases. These variables follow Gaussian distribution

Case	Parameter	Mean	Standard Deviation
(a)	Concrete cover (cm)	5.0	0.5
	f_c (MPa)	45	6.75
	w/c	0.45	0.09
(b)	Concrete cover (cm)	4.5	0.45
	f_c (MPa)	40	6
	w/c	0.5	0.1
(c)	Concrete cover (cm)	4.0	0.4
	f_c (MPa)	35	5.25
	w/c	0.6	0.12

Application 1: Hyperstatic Symmetric Beam

The first application of this study concerns the hyperstatic beam presented in Figure 1. The beam has 5 meters of span length and rectangular cross section of 25 cm x 50 cm (thickness x high), which is subjected to an uniform distributed load. The Figure 1 presents the static scheme applied on this beam and the maximum bending moment and shear effort values. There are two maximum bending moments: the negative at the central support and the positive at the semi-span. The maximum shear effort occurs at the central support. These efforts are described, respectively, by the following expressions:

$$M_A = \frac{9\left(g_1 + q_1\right)L^2}{128} \tag{38}$$

$$M_B = \frac{\left(g_1 + q_1\right)L^2}{8} \tag{39}$$

$$V_C = \frac{5\left(g_1 + q_1\right)L}{8} \tag{40}$$

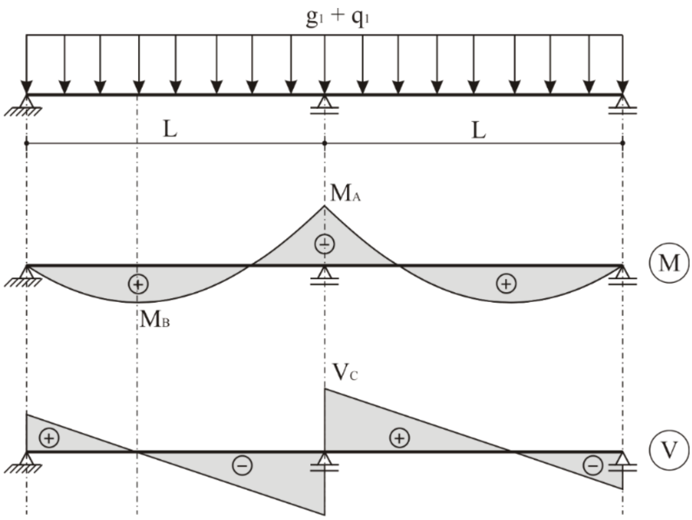

Figure 1. Static scheme 1 – load; bending moment and shear effort diagrams.

The beam illustrated in Figure 1 was designed following the recommendations of [30]. Moreover, this desing accounts for the mean load values presented in Table 1. The design of this beam is illustrated in Figure 2.

In the context of progressive mechanical collapse path, hyperstatic structures are described consistently by parallel systems. Then, the mechanical collapse is observed when the amount of local collapses is equal to the hyperstatic degree plus one. The beam analysed has hyperstatic degree equal to one. Therefore, the mechanical collapse is accomplished when at least two local collapses are observed.

Initially, the failure occur due to the negative or positive bending moment (A or B, respectively), or shear effort (C). These failure modes are orderly assembled in a failure tree, as showed in Figure 3.

If the first failure mode occurs, due to the negative bending moment (A), two other failures may occur: failure due to the positive bending moment or shear failure. A similar case is observed when the first failure mode is the positive bending moment. However, if the first failure mode is the shear, structural collapse is assumed.

When the first failure mode is the bending moment, the shear and the bending diagrams are shifted due to the formation of plastic hinges in the failure zone. Therefore, the conditional failure probabilities are defined according to the new beam static configuration.

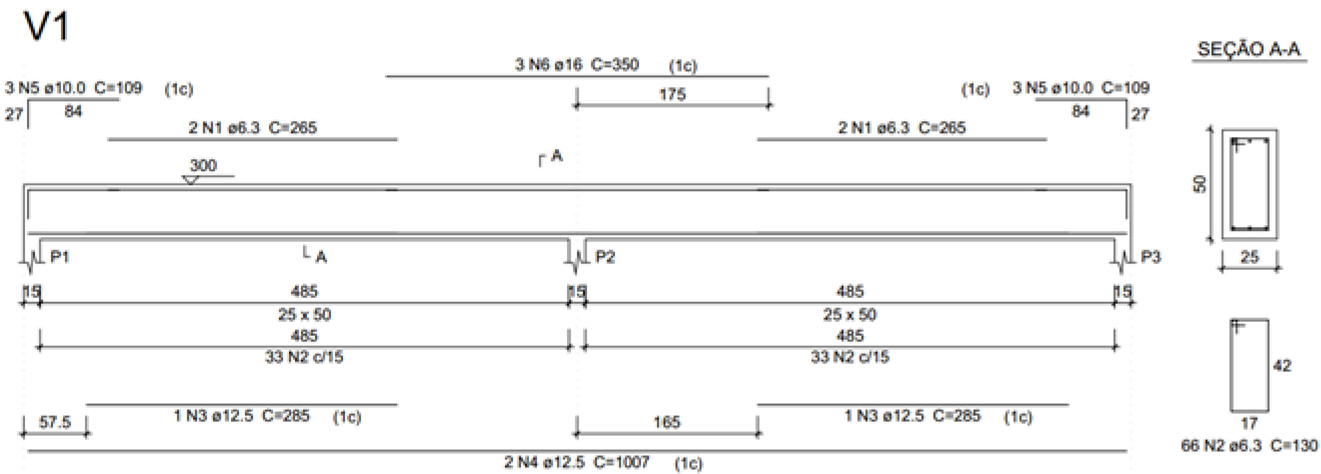

Figure 2. Design 1 – Hyperstatic symmetric beam.

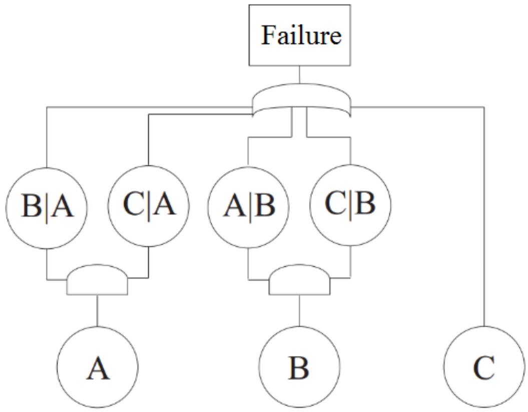

Figure 3. Failure tree 1.

If the first failure mode is the positive moment, the hinge formation will provide a large negative bending moment increment. Then, the positive moment failure mode leads automatically to the failure of the negative bending moment. On the other hand, when the first failure is the negative bending moment, the conditional probabilities must be analysed in order to determine the critical path. This analysis leads to the failure probability determination presented in the Eq. (41).

$$P_f = P[A]\left(P[B\,|\,A]+P[C\,|\,A]\right)+P[B]P[A\,|\,B]+P[C] \tag{41}$$

Application 2: Cantilever Hyperstatic Beam

The second application concerns a beam one-time hyperstatic. The beam first spam has 4 m length and the second 3 m length. The beam has a cantilever region of 2 m length. The cross section is 25 x 50 cm (thickness x high) along the entire beam length.

Shear effort and bending moment diagrams are illustrated in Figure 4. There are three maximum bending moments, two negatives and one positive. Moreover, there is a maximum shear effort, which are calculated with the following equations:

$$M_A = \frac{3L_1^{\,3}\left(g_1+q_1\right)+4L_1^{\,2}L_2\left(g_1+q_1\right)-L_2^{\,3}\left(g_1+q_1\right)+2L_2L_3^{\,2}\left(g_2+q_2\right)}{8\left(L_1+L_2\right)} - \frac{L_1^{\,2}\left(g_1+q_1\right)}{2} \tag{42}$$

$$M_B = \frac{\left[3L_1^{\,3}\left(g_1+q_1\right)+4L_1^{\,2}L_2\left(g_1+q_1\right)-L_2^{\,3}\left(g_1+q_1\right)+2L_2L_3^{\,2}\left(g_2+q_2\right)\right]^2}{128L_1\left(L_1+L_2\right)\left(g_1+q_1\right)} \tag{43}$$

$$M_C = \frac{L_3^{\,2}\left(g_2+q_2\right)}{2} \tag{44}$$

$$V_D = \frac{L_1^{\,3}\left(g_1+q_1\right)+4L_1^{\,2}L_2\left(g_1+q_1\right)-4L_1L_3^{\,2}\left(g_2+q_2\right)}{8L_2\left(L_1+L_2\right)} + \frac{5L_2^{\,3}\left(g_1+q_1\right)-6L_2L_3^{\,2}\left(g_2+q_2\right)}{8L_2\left(L_1+L_2\right)} \tag{45}$$

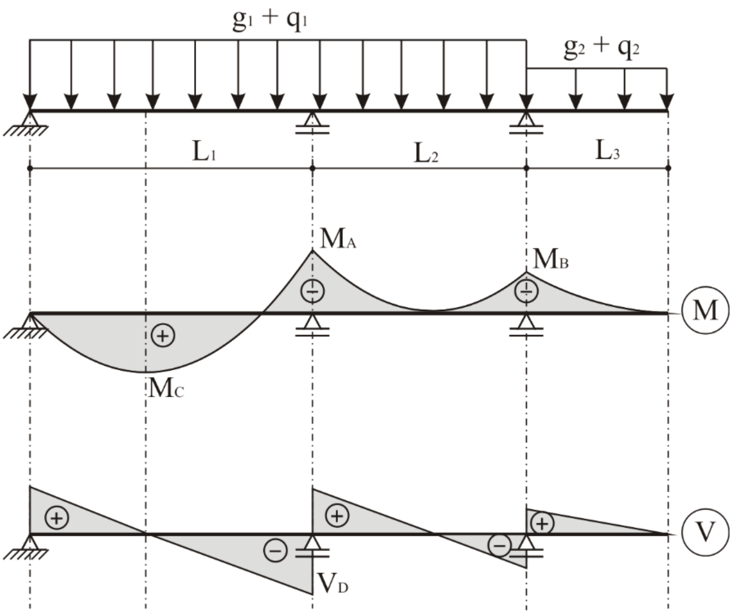

Figure 4. Static scheme 2 – load; bending moment and shear diagrams.

The beam design is illustrated in Figure 5.

Analogously to the previous application, the failure tree is defined by determining the critical paths and the probability of failure (see Figure 6). Four initial failures modes, three of them relative to bending moment (A, B and C) and the other relative to shear efforts (D), are considered.

A plastic hinge is formed at the zones of failure due to the bending moments. Thus, new diagrams are utilized for the new static configuration. When the failure occurs at the negative bending moment zones, three other failures may occur: due to the positive or the negative bending moments, at points B or C, or shear effort at D. If the first failure mode is due to the bending moment at B, it is assumed that the plastic hinge formation largely increases the negative bending moment in A. Then, in this path, the second failure occurs automatically in A. On the other hand, the failure mode due to the bending in C generates a hypostatic zone (cantilever region). Thus, in this case, structural collapse is assumed. Lastly, the failure due to the shear effort also leads to the collapse of the beam.

Therefore, the probability of failure can be calculated with Eq. (46).

$$P_f = P[A]\left(P[B|A]+P[C|A]+P[D|A]\right)+P[B]P[A|B]+P[C]+P[D] \quad (46)$$

RESULTS AND DISCUSSION

Time for Corrosion Initiation

The probabilistic analysis for the corrosion time initiation is performed by the Monte Carlo simulation. The limit state function is given by Eq. (47).

$$g(X)=t-t_{ini}(X) \quad (47)$$

The probability curves of corrosion initiation due to the carbonation and the chloride ingress are presented in Figure 7. Three cases are considered: (a), (b) and (c). For the case (a), a high probability of reinforcements' depassivation, for both types of corrosion, is observed before 50 years. This result was obtained with the parameters recommended in [30] for environments with high aggressiveness.

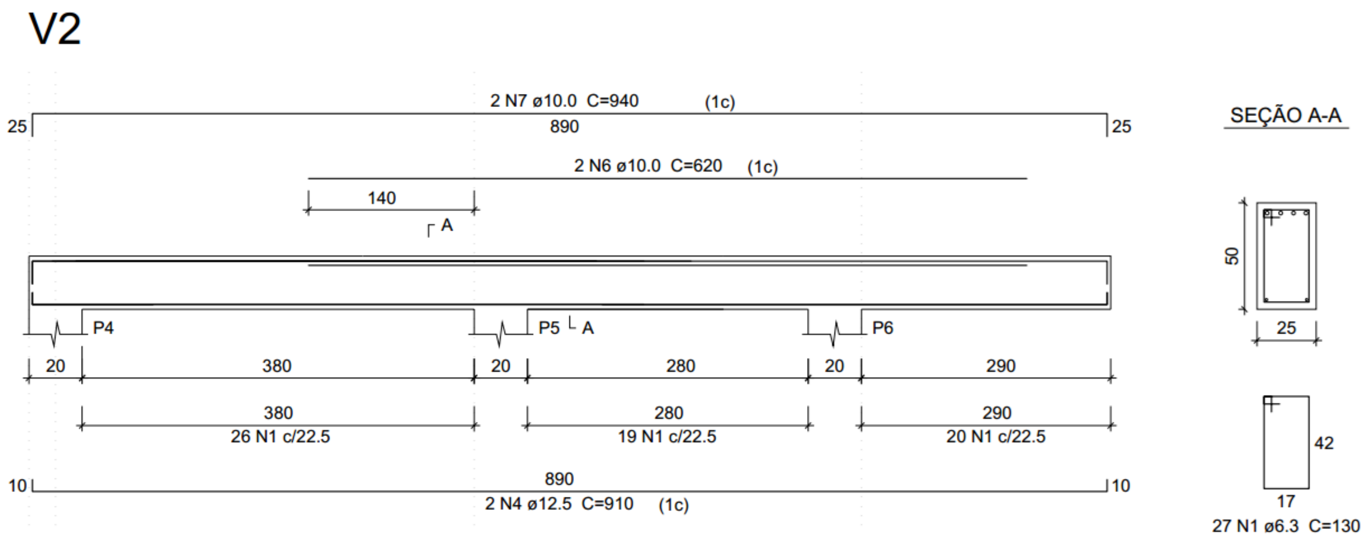

Figure 5. Design 2 – Cantilever Hyperstatic Beam.

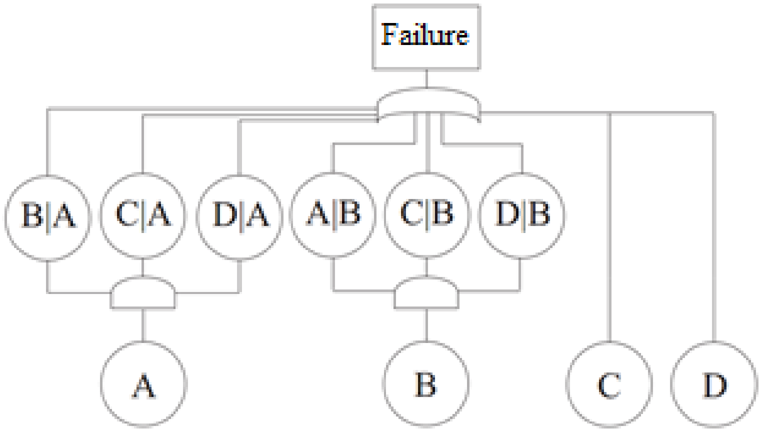

Figure 6. Failure tree 2.

As observed in the other curves of Figure 7, the probability of corrosion initiation grows with the increase of the w/c rate.

In the critical case, with the highest w/c rate and lowest concrete cover, a significant probability of reinforcements' depassivation is observed after 5 years. The corrosion curves present different behaviours due to the distinct corrosion mechanisms: the carbonation is related to the uniform corrosion and the chlorides are associated to the pitting corrosion. The corrosive process due to the chloride ions largely increases in the first years whereas the growth is uniform for carbonation.

Application 1: Hyperstatic Symmetric Beam

As illustrated in Figure 8 and Figure 9, the large increase in the probability of corrosion initiation generates substantial reductions in the rebar' diameters. Such a reduction achieves 90% for corrosion due to the chloride ions. In this corrosion type, higher values for reinforcements' cross section reduction are obtained if compared to the carbonation.

The curves of reinforcements' mass loss present different behaviour according to the aggressive agent. Therefore, environments with high chloride concentration and high porosity concretes, for instance, lead to faster reinforcements' mass loss. Because pit corrosion is localized, only a small region lose the passive film. It generates a major ion concentration, which accelerates the corrosive reactions.

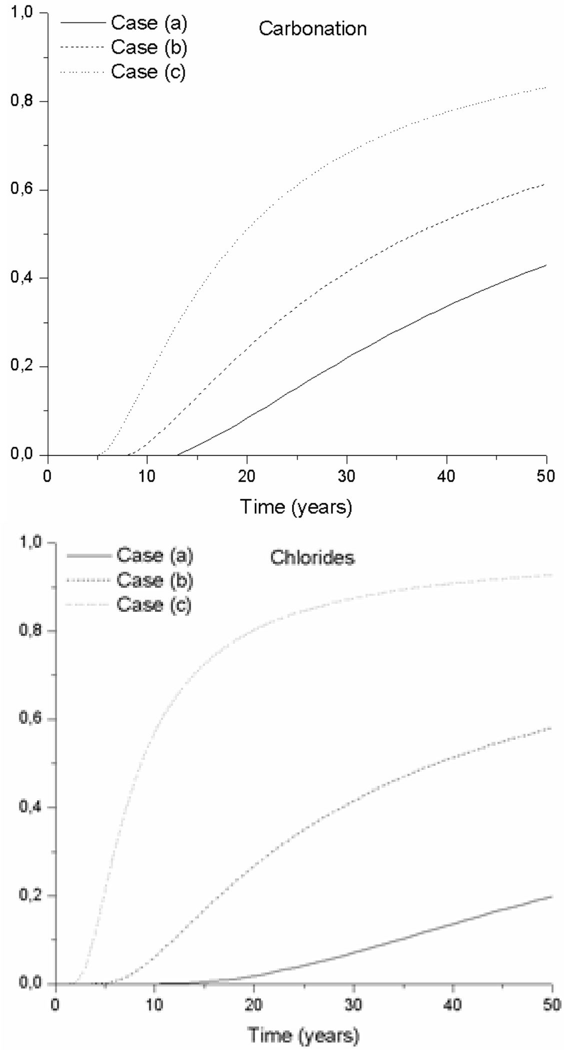

Figure 7. Probability of corrosion initiation.

The velocity of the reinforcements' mass loss influence the increment on the probability of failure along time. The Figure 10 presents the probability of failure along time for carbonation and chloride corrosion cases.

In the carbonation case, high rebar' diameter reduction was observed after 10 years of beam construction. However, substantial effects on the probability of failure were observed only after 20 years. High values of probability of failure were obtained at the end of 50 years. For the worst scenario – case (c) –

the probability of failure equal to 0.032 was obtained. For the chloride corrosion case, the probability of failure highly increases in the first years, where the probability of corrosion initiation and reinforcements' mass loss are accentuated.

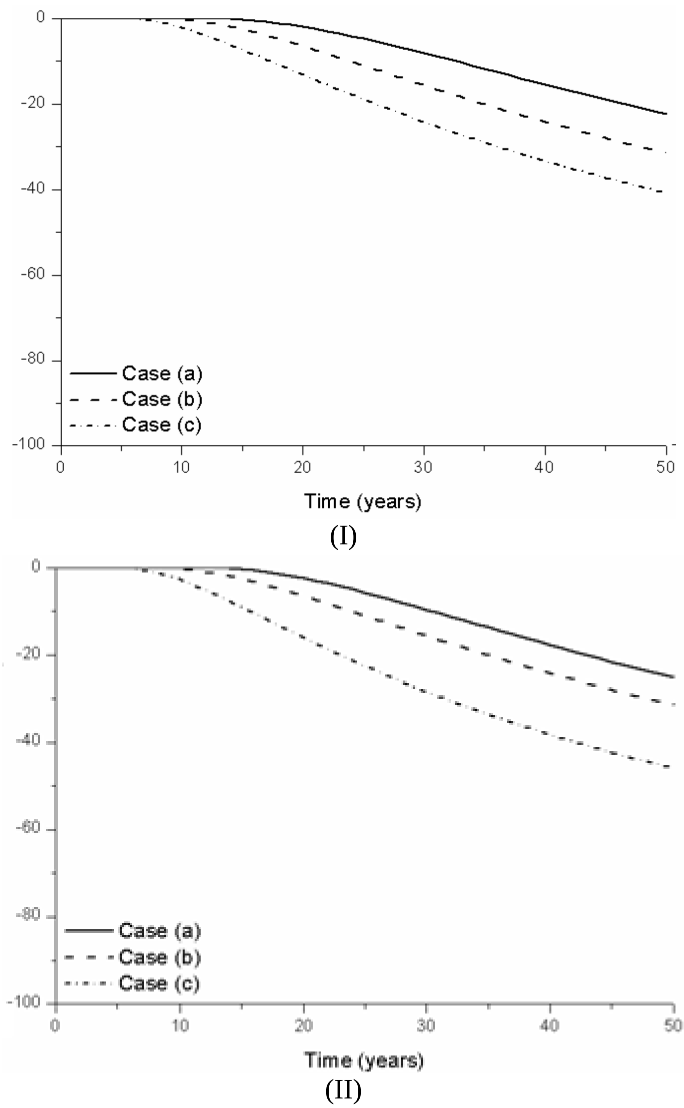

(II)

Figure 8. (Continued)

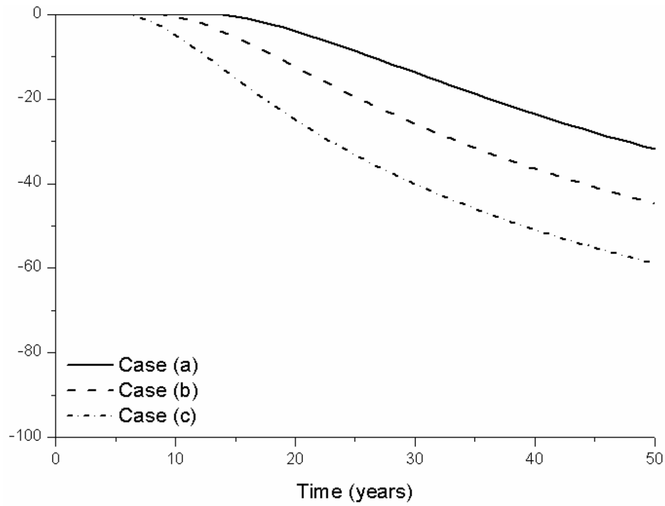

(III)

Figure 8. Percentage reinforcements' mass loss curves for carbonation corrosion: (I) negative reinforcement; (II) positive reinforcement; (III) shear reinforcement.

The analyses for the most probable failure path and the individual probabilities of failure along time were accomplished for carbonation and chloride corrosion cases. The results are presented only for the case (c), since this one has the highest probability of failure.

The analyses of carbonation corrosion show that the main failure mode may change across time. Then, the mechanism of failure observed at the beginning of the corrosive process may not be the same to the observed at the end of the service life. In carbonation case (see Figure 11), the most probable failure mode is the positive bending moment in the beginning of the corrosive process. However, the most probable failure mode changes after 34 years. The negative bending moment becomes the most probable.

This scenario could be explained by analysing the individual probabilities of failure. The positive bending moment is more susceptible to the failure at the beginning of the corrosive process, when the reinforcements' mass loss grow, the failure due to the negative bending moment becomes most significant and had a large increase.

The change on the failure modes is not observed in chloride corrosion case, as observed in Figure 12. It occurs because the reinforcements' mass loss is high in the first years. Then, over 50 years, the collapse mechanism is the first failure due to the negative bending moment (A), following by the failure in the positive (B).

Application 2: Cantilever Hyperstatic Beam

The probability of failure curves are presented in Figure 13 for each of the three cases analysed, for corrosion due to the carbonation and the chloride ingress. The curve of the carbonation corrosion is different from the others. The expected failure curve grows along time. However, for carbonation, a smooth decrease is observed after the peak failure.

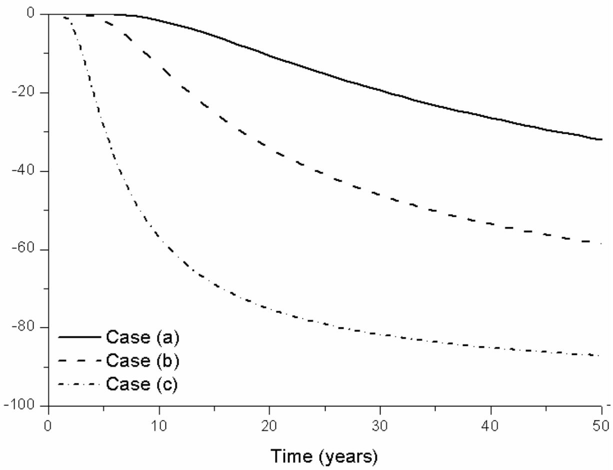

(I)

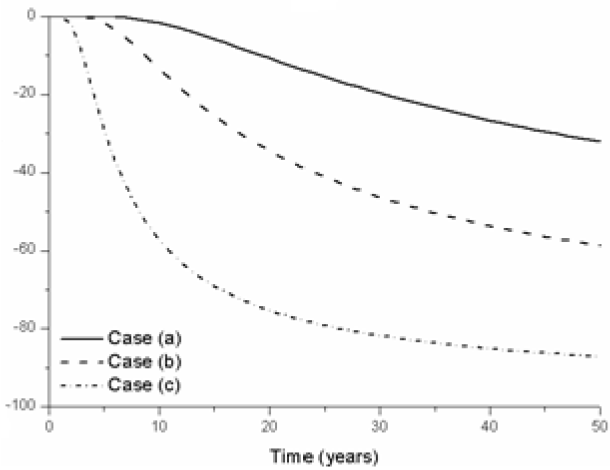

(II)

Figure 9. (Continued)

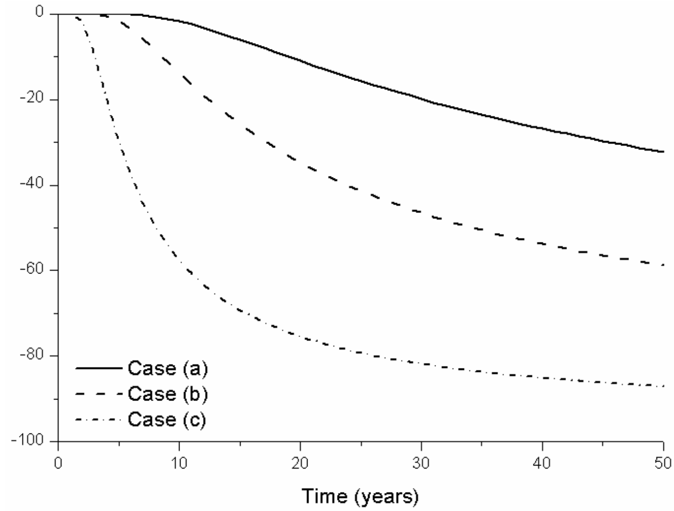

(III)

Figure 9. Percentage reinforcements' mass loss curves for chloride corrosion: (I) negative reinforcement; (II) positive reinforcement; (III) shear reinforcement.

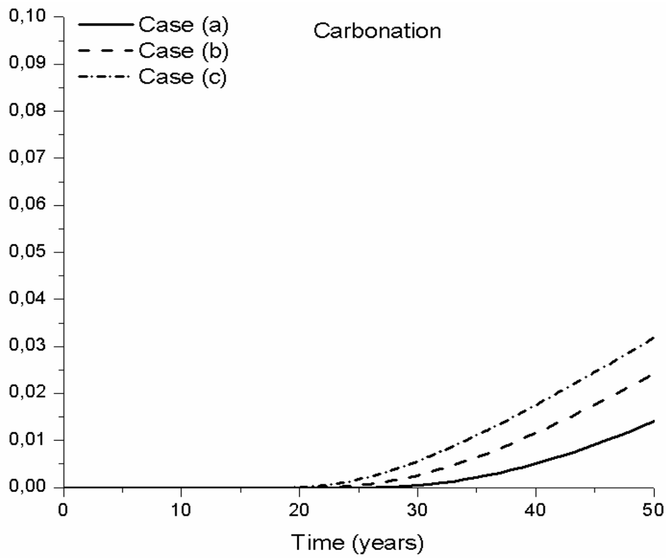

Figure 10. (Continued).

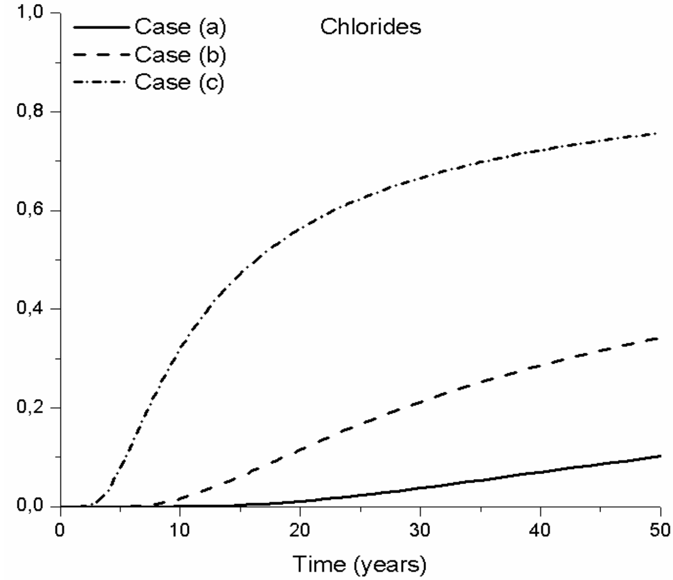

Figure 10. Probability of failure – Application 1.

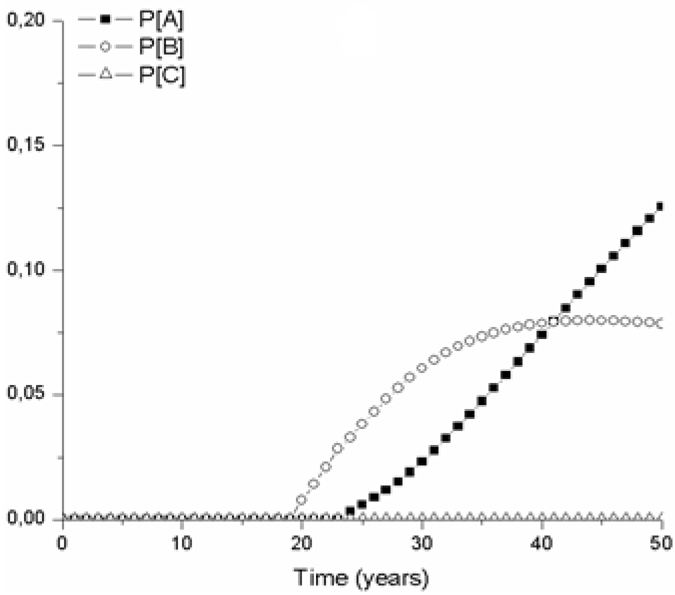

(I)

Figure 11. (Continued)

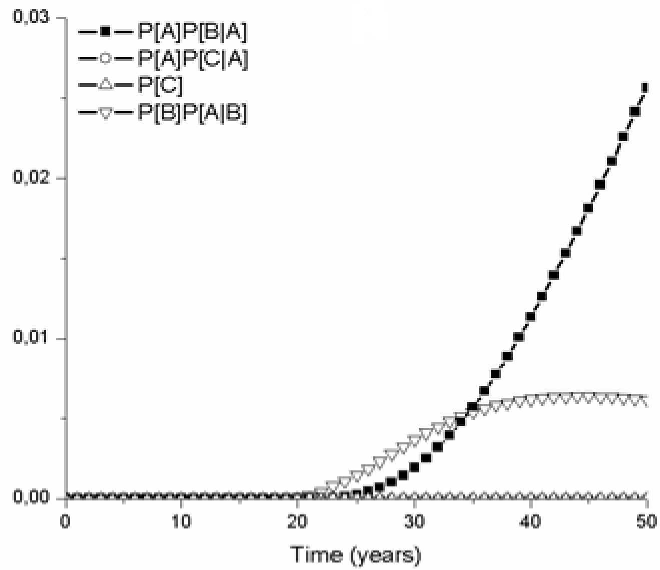

(II)

Figure 11. Failure modes due to the carbonation corrosion – Application 1: (I) individual probabilities; (II) failure paths.

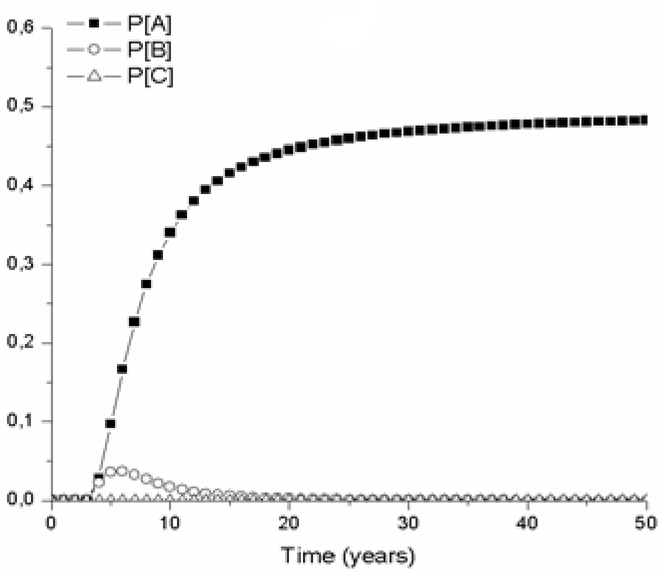

(I)

Figure 12. (Continued).

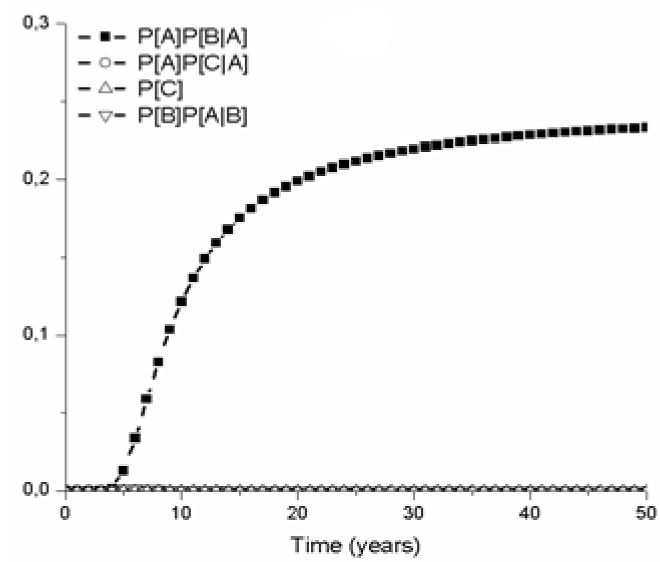

(II)

Figure 12. Failure modes due to the chloride corrosion – Application 1: (I) individual probabilities; (II) failure paths.

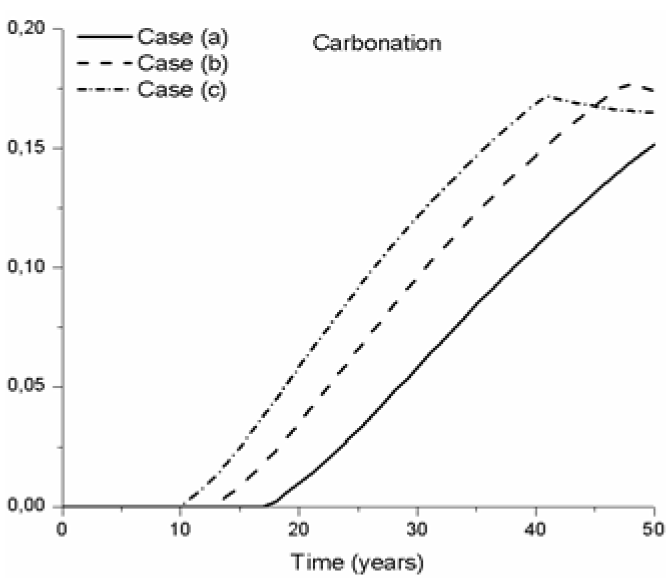

Figure 13. (Continued)

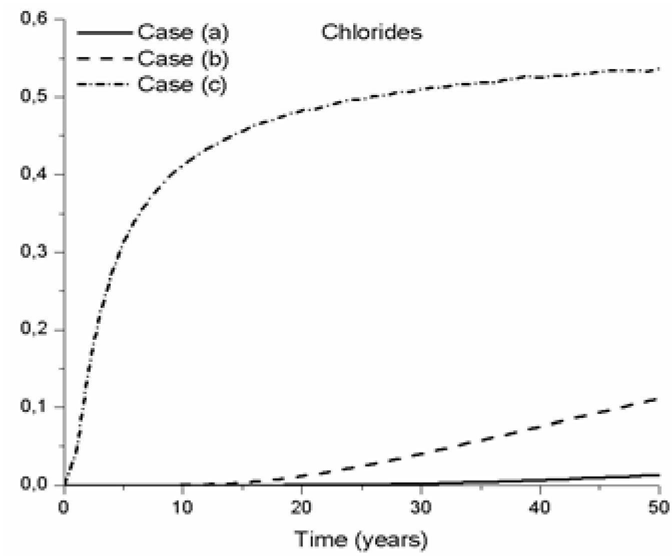

Figure 13. Probability of failure – Application 2.

This atypical behaviour is explained if the failure paths are analysed along time. The probability of failure for the negative bending moment at C has been dominant from the beginning of the analysis until 42 years, Figure 14. This localized failure causes the collapse of the beam, once the cantilever region becomes a hypostatical system. However, the failure path modifies after 42 years, with the increase of the reinforcements' mass loss. Then, the first collapse becomes the negative bending moment at A. Then, it is necessary another failure (B, C or D) calculated by conditional probabilities, for the beam mechanical collapse.

For chloride corrosion case, the curve behaviour is different from the observed in carbonation case. This difference is visualized by the analyses of the individual failure modes. Analogously to the previous application, the reinforcements' mass loss is higher in the first years. Then, the first failure is always the negative bending moment in A.

CONCLUSION

This study presented the mecano-probabilistic analysis of reinforced concrete structures subjected to reinforcements' corrosion. Trees of failures were proposed which enable determining the most probable failure path. The results showed that the most probable failure path could change along time. This information has major importance during a performance analysis once unexpected collapse mechanisms appear.

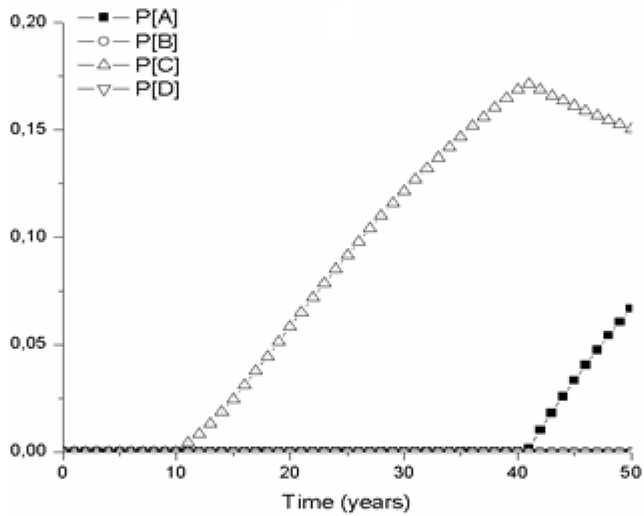

(I)

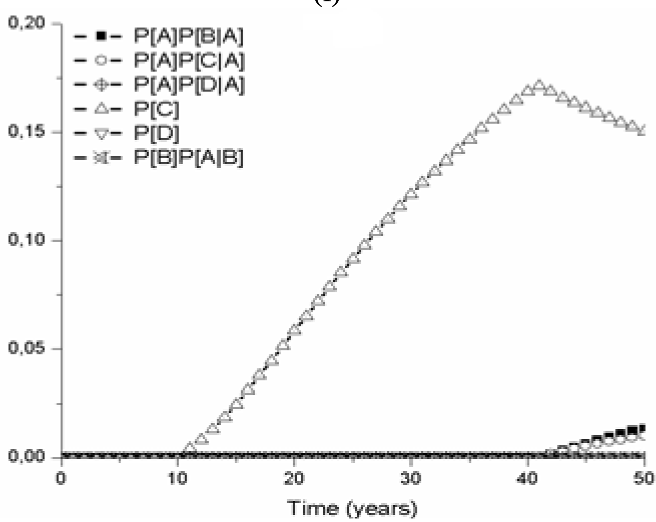

(II)

Figure 14. Failure modes due to the carbonation corrosion – Application 2: (I) individual probabilities; (II) failure paths.

Moreover, the corrosion type, i.e., carbonation or chloride ingress, influences the structural behaviour on the collapse. The critical failure path for chloride corrosion case did not change for the two applications presented. The dependence of this corrosion type on the reinforcements' mass loss explains this behaviour. Then, for other environmental scenarios with lower rebar diameter reduction, these changes could appear.

The corrosion triggered by chlorides has the severe reinforcements' mass loss. The mass loss reached 90% at the end of 50 years for w/c = 0.6. Lower values for carbonation case were obtained. However, the reduction of the carbonation case cannot be disregarded. The reduction of more than a half of the reinforcements' cross section area (58.9%) was observed. These reductions have major importance over the probability of failure. Especially in the chloride corrosion case.

The analyses followed the recommendations of [30]. Then, w/c = 0.45, concrete cover equate to 5cm and f_c equal to 45MPa were adopted. However, high values for the probability of reinforcements' depasstivation were observed before 20 years. Chloride corrosion case presented large sensibility to the increase of w/c rate. For carbonation case, the growth is uniform with the w/c increase.

Acknowledgments

The authors would like to thank the sponsorship of this research project by São Paulo Research Foundation (FAPESP), grant number 2014/18928-2.

References

[1] Gentil, V. Corrosão, Rio de Janeiro: Rio de Janeiro: *LTC – Livros Técnicos e Científicos Editora* [LTC - Technical and Scientific Books Publisher] S.A., 4 ed., 2006, 392p.

[2] Bertolini, L.; Elsener, B.; Pedeferri, P.; Polder, R. P. Corrosion of Steel in Concrete: Prevention, Diagnosis and Repair. Weinheim, WILEY-VCH Verlag GmbH & Co. KGaA, 2004, 381p.

[3] Schmitt, G. Global needs for knowledge dissemination, research, and development in materials deterioration and corrosion control, New York: The World Corrosion Organization, 2009. 44p.

[4] Liberati, E.A.P.; Nogueira, C.G.; Leonel, E.D.; Chateauneuf, A. Failure analysis of reinforced concrete structures subjected to chloride penetration and reinforcements corrosion. In: Abdel Salam Hamdy Makhlouf; Mahmood Aliofkhazraei. (Org.). *Handbook of Materials Failure Analysis with Case Studies from the Chemicals, Concrete and Power Industries*. 1 ed.: Elsevier, 2016, v. 1, p. 93-121.

[5] Mccafferty, E. Introduction to corrosion science, New York: Springer Science & Business Media, 2010. 571p.

[6] Cascudo, O; Carasek, H. Ação da Carbonatação no Concreto. In: ISAIA, G. C. Concreto: Ciência e Tecnologia, São Paulo: Instituto Brasileiro do Concreto – IBRACON [Concrete: Science and Technology, São Paulo: Brazilian Institute of Concrete - IBRACON], 1 ed., 1 v., 2011. p. 849-886.

[7] Figueiredo, E.J.P.; Meira, G. R. *Boletín Técnico*. Corrosión de armadura de estructuras de hormigón, Mérida: Asociación Latinoamericana de Control de Calidad, Patología y Recuperación de la Construcción - ALCONPAT Int. [Technical Bulletin. Corrosion of reinforcement of concrete structures, Merida: Latin American Association of Quality Control, Pathology and Construction Recovery - ALCONPAT Int.], 2013. 30p.

[8] Samson, E.; Marchand, J. Modeling the effect of temperature on ionic transport in cementitious materials. *Cement and Concrete Research*, 2007, 37:455-68.

[9] El Hassan, J.E.; Bressolette, P.; Chateauneuf, A.; El Tawil, K. Reliability-based assessment of the effect of climatic conditions on the corrosion of RC structures subject to chloride ingress. *Engineering Structures*, 2010, 32:3279-3287.

[10] Frangopol, D.M.; Lin, K.; Estes, A.C. Life-cycle cost design of deteriorating structures. *Journal of Structural Engineering*, 1997, 123:1390-1401.

[11] Pellizzer, G.P.; Leonel, E.D.; Nogueira, C.G. Influence of reinforcement's corrosion into hyperstatic reinforced concrete beams: a probabilistic failure scenarios analysis. *Revista IBRACON de Estruturas e Materiais*, 2015, 8:479-490.

[12] Houst, Y.F.; Wittmann, F.H. Depth profiles of carbonates formed during natural carbonation. *Cement and Concrete Research*, 2002, 32:1923-1930.

[13] Yoon, I.S.; Çopuroglu, O.; Park, K.B. Effect of global climatic change on carbonation progress of concrete. *Atmospheric Environment*, 2007, 41:7274-7285.

[14] Park, D.C. Carbonation of concrete in relation to CO_2 permeability and degradation of coatings. *Construction and Building Materials*, 2008, 22:2260-2268.

[15] Sudret, B. Probabilistic models for the extent of damage in degrading reinforced concrete structures. *Reliability Engineering and System Safety*, 2008, 93:410-422.

[16] Saetta, A.V.; Vitaliani, R.V. Experimental investigation and numerical modeling of carbonation process in reinforced concrete structures Part I: Theoretical formulation. *Cement and Concrete Research*, 2004, 34:571-579.

[17] Song, H.W.; Kwon, S.J.; Byun, K.J; Park, C.K. Predicting carbonation in early-aged cracked concrete. *Cement and Concrete Research*, 2006, 36:979-989.

[18] Guzmán S, Gálvez JC, Sancho JM. Cover cracking of reinforced concrete due to rebar corrosion induced by chloride penetration. *Cement and Concrete Research*, 2011, 41:893-902.

[19] Bastidas-Arteaga, E.; Sanchez-Silva, M.; Chateauneuf, A.; Ribas-Silva, M. Coupled reliability model of biodeterioration, chloride ingress and cracking for reinforced concrete structures. *Structural Safety*, 2008, 30:110-129.

[20] Zhao, Y.; Yu, J.; Jin, W. Damage analysis of cracking model of reinforced concrete structures with rebar corrosion. *Corrosion Science*, 2011, 53:3388-3397.

[21] Biondini, F.; Frangopol, D.M. Probabilistic limit analysis and lifetime prediction of concrete structures. *Struct. Infrastructure Eng*., 2008, 4(5):399-412.

[22] Nogueira, C.G.; Leonel, E.D.; Coda, H.B. Reliability algorithms applied to reinforced concrete structures durability assessment. *IBRACON Structures and Materials Journal*, 2012, 5:440-450.

[23] Nogueira, C.G.; Leonel, E.D. Probabilistic models applied to safety assessment of reinforced concrete structures subjected to chloride ingress. *Engineering Failure Analysis*, 2013, 31:76-89.

[24] Liberati, E.A.P.; Nogueira, C.G.; Leonel, E.D.; Chateauneuf, A. Nonlinear formulation based on FEM, Mazars damage criterion and Fick's law applied to failure assessment of reinforced concrete structures subjected to chloride ingress and reinforcements corrosion. *Engineering Failure Analysis*, 2014, 46:247-268.

[25] Papadakis, V.G.; Roumeliotis, A.P.; Fardis, M.N.; Vayenas, C.G. Mathematical modelling of chloride effect on concrete durability and

protection measures. In: Dhir, RK; Jones, MR. *Concrete repair, rehabilitation and protection*. London: E&FN Spon, 1996.
[26] Papadakis, V.G.; Fardis, M.N.; Vayenas, C.G. Effect of composition, environmental factors and cement-lime mortar coating on concrete carbonation. *Materials and Structures*, 1992, 25:293-304.
[27] Vu, K.A.T.; Stewart, M.G. Structural reliability of concrete bridges including improved chloride-induced corrosion models. *Structural Safety*, 2000, 22:313-333.
[28] Wang, X.; Stewart, M.G.; Nguyen, M. Impact of climate change on corrosion and damage to concrete infrastructure in Australia. *Climatic Change*, 2012, 110:941-957.
[29] Du, Y.G.; Clark, L.A.; Chan, A.H.C. Residual capacity of corroded reinforcing bars. *Magazine of Concrete Research*, 2005, 57:135-147.
[30] Associação Brasileira de Normas Técnicas [Brazilian Association of Technical Standards]. NBR 6118: Projeto de estruturas de concreto – Procedimento [NBR 6118: Design of Concrete Structures - Procedure]. Rio de Janeiro, 2014.
[31] Cristensen, P.T.; Baker, M. J. Structural reliability theory and its applications, Berlim: Springer Science & Business Media, 2012. 248p.
[32] Beirlant, J.; Goegebeur, Y.; Segers, J.; Teugels, J. Statistics of extremes: theory and applications. West Sussex: John Wiley & Sons, 2006. 514p.
[33] Angst, U.; Elsener, B.; Larsen, C.K.; Vennesland, Ø. Critical chloride content in reinforced concrete — A review. *Cement and Concrete Research*, 2009, 39:1122-1138.
[34] Albuquerque, A.T.; Otoch, S. Proposta de classificação da agressividade do ambiente na cidade de Fortaleza [Proposal of classification of the aggressiveness of the environment in the city of Fortaleza]. In: Congresso Brasileiro do Concreto [Brazilian Congress of Concrete], 47°, Anais, Olinda, 2005.
[35] Meira, G.R.; Padaratz, I. J. Efeito do distanciamento em relação ao mar na agressividade por cloretos [Effect of distance from sea on aggression by chlorides]. In: Congresso Brasileiro do Concreto, 44°, Anais, Belo Horizonte, 2002 [Brazilian Congress of Concrete, 44th, Anais, Belo Horizonte, 2002].
[36] Alves, A.M.C. Contribuição à análise da perspectiva de vida útil de estruturas em concreto face ao teor de cloreto registrado em Maceió-AL [Contribution to the analysis of the useful life perspective of concrete structures in relation to the chloride content registered in Maceió-AL]. Maceió, 2007, Dissertação (mestrado) - Centro de Tecnologia,

Universidade Federal de Alagoas, 118p [Maceió, 2007, Dissertation (master's degree) - Technology Center, Federal University of Alagoas, 118p].

[37] Schiebl, P.; Lay, S. Statistical models and methodology for durability. In: SARJA, A. Predictive and Optimised Life Cycle Management: Buildings and Intrastructure. New York: Taylor & Francis, 2006.

[38] Mangat, P.S.; Molloy, B. T. Prediction of long term chloride concentration in concrete. *Materials and structures*, 1994, 27:338-346.

[39] Truc, O.; Ollivier, J.P.; Carcasses, M. A new way for determining the chloride diffusion coefficient in concrete from steady state migration test. *Cement and Concrete Research*, 2000, 30:217-226.

[40] Chen, D.; Mahadevan, S. Chloride-induced reinforcement corrosion and concrete cracking simulation. *Cement and Concrete Composites*, 2008, 30:227-238.

[41] Tuuti, K. Corrosion of steel in concrete. Stockholm: Swedish Cement and Concrete Research Institute, 1982.

[42] Helene, P.R.L. Contribuição ao estudo da corrosão em armaduras de concreto armado, 1993, Tese (Livre docência) - Escola Politécnica, Universidade de São Paulo [Contribution to the study of corrosion in reinforced concrete reinforcement, 1993, Thesis (Free teaching) - Polytechnic School, University of São Paulo].

[43] Papadakis, V. G.; VAYENAS, C. G.; FARDIS, M. N. Fundamental modeling and experimental investigation of concrete carbonation. *ACI Materials Journal*, 1991, 88: 363-373.

[44] Yoon, I-S.; Çopuroglu, O; Park, K-B. Effect of global climatic change on carbonation progress of concrete. *Atmospheric environment*, 2007, 41:7274-7285.

[45] Melchers, R. E. *Structural Reliability Analysis and Prediction*, New York: John Wiley & Sons, 2 ed., 1999. 456p.

[46] Santos, K.R.M.; Beck, A.T. A benchmark study on intelligent sampling techniques in Monte Carlo simulation. *Latin American Journal of Solids and Structures*, 2014, 12:624-648.

[47] Lee, W-S.; Grosh, D.L.; Tillman, F.A.; Lie, C.H. *Fault Tree Analysis, Methods, and Applications: A Review*. Reliability, IEEE Transactions, 1985, 34:194-203.

In: Reinforced Concrete
Editor: Sharon Robinson
ISBN: 978-1-53610-752-4

Chapter 4

ATMOSPHERIC CORROSION OF STEEL-REINFORCED CONCRETE IN A COASTAL CITY LOCATED ON A TROPICAL ISLAND

***A. Castañeda*[1], *F. Corvo*[2,*], *J. J. Howland*[3], *R. Marrero*[4] *and D. Fernández*[1]**

[1]Material Protection Group, Environment Division.
National Center for Scientific ResearchHavana, Cuba
[2]Corrosion Research Center(CICORR),
Autonomous University of Campeche, Buenavista,
San Francisco de Campeche, Campeche, México
[3]Technological University of Havana,
Civil Engineering School, Havana, Cuba
[4]Technological University of Havana,
Chemistry Engineering School, Havana, Cuba

ABSTRACT

Studies concerning with atmospheric corrosion of metals have been carried out during many years. Havana City could be considered as one of the zones of higher atmospheric corrosion in the world. In the present

[*] Corresponding Author E-mail: frecorvo@uacam.mx.

chapter, the methodology often used in studies of atmospheric corrosion in metals is applied to study the atmospheric corrosion of steel-reinforced concrete. It is possible to reduce the premature deterioration in the structures in conditions of a coastal city located in a tropical island through the evaluation of the corrosion behavior of different types of concrete and covering thicknesses.

The use of reinforced concrete with water cement ratios 0.5 and 0.6 and covering thicknesses 20 and 40 mm does not assure an adequate durability and useful life for structures submitted to corrosivity categories of the atmospheres very high (C5) and extreme (CX) in a coastal-industrial atmosphere. It is required the use of w/c ratio 0.4 and cover thickness 40 mm to assure an adequate durability.

Keywords: building screening, corrosion aggressivity, reinforcing steel, reinforced concrete, coastal city, chloride deposition, tropical climate.

INTRODUCTION

Atmospheric corrosion of steel-reinforced concrete is the phenomenon that most influence in the deterioration of reinforced concrete structures, principally in coastal cities [1-4]. The costs in maintenance and repair works of structures have been economically very significant worldwide [5-8].

An alternative to assess the durability and useful life of reinforced concrete structures has been the application of computer-processing software. However, most current software does not consider temporary transient processes occurring in the atmosphere such as: marine aerosol penetration caused by chloride deposition $[Cl^{-}DR]$, variations in relative humidity-temperature complex, speed and wind flow direction, as well as the distance from the sea [9-13]. These processes accelerate the phenomenon of atmospheric corrosion not only of steel reinforced concrete, but also in the metallic materials most frequently used in the construction industry, such as: carbon steel, zinc, copper and aluminum.

The application of electrochemical techniques has allowed obtaining featured results about corrosion of steel reinforced concrete in the last years. To predict chloride diffusion coefficient in reinforced concrete an equivalent circuit of the steel/concrete interface was fitted by Electrochemical Impedance Spectroscopy. It is an alternative method [14, 15]. On the other hands, some results suggested that harmonic analysis technique was capable of providing higher degree of accuracy than EIS and Tafel extrapolation in the determination of corrosion current (CR) in steel-reinforced concrete [16]. The influence of cracks on chloride-induced corrosion of steel in the concrete of high performance submitted to different loading conditions was studied from microcell corrosion measuring techniques such as Linear Polarization Resistance (LPR) and potentiodynamic (cyclic) polarization [17]. An Evans diagram representing the corrosion system of the steel corrosion in cracked concrete using the evaluation of macro cell and microcell ratef romTafel polarization response was developed [18]. Free corrosion potential (FCP), EIS and LPR techniques were used in the electrochemical investigation of chloride-induced of black steel rebar under simulated serviced condition [19].

Many interesting results have been obtained in the last years from the analysis of corrosion products in the steel/concrete interface. A relation between the radial pressure induced by the expansion of corrosion products and weight loss percentage of corroded steel was developed [20]. On the other hand, an analytical model based in the mechanical damage and elastic mechanical damage to predict the concrete cracking due to corrosion of steel reinforced concrete was developed too [21]. The use of Gaussian functions to describe the non-uniform spatial of distribution of the corrosion products by chlorides in the reinforced concrete specimen exposed using backscattering electro imaging and image analysis was proposed [22]. Corrosion products can be accumulated at steel/concrete interface, penetrate into cement paste and deposit within hydration products and air voids, where only a small amount of this corrosion products is needed to induce visible cover cracking [23].

Nevertheless, the corrosion of steel reinforced concrete using electrochemical techniques, as well as from corrosion products in the steel/concrete interface have been analyzed under laboratory and outdoors accelerated conditions in the last years. Accelerated conditions simulate higher corrosivity categories due to direct action of chloride ions, without take into account the temporary transient processes occurring in the atmosphere.

Atmospheric corrosion for the metallic materials most frequently used in the construction industry (carbon steel, zinc, copper and aluminium) submitted to outdoor exposure conditions has been studied using statistical regressions. The most used types of regressions are shown (Table 1).

The regression type number 4 has been very often used to analyze the behavior of atmospheric corrosion respecting time of exposure.

Table 1. Statistical regressions most often used in atmospheric corrosion studies

Regression	No.	References
$r_{corr} = a \pm b[Cl^{-}DR] \pm c[SO_x^{-}DR] \pm d[Cl^{-}DR][SO_x^{-}DR] \pm e[Cl^{-}DR]^2 \pm f[SO_x^{-}DR]^2$	1	[24]
$r_{corr} = a \pm b[Cl^{-}DR] \pm c[SO_x^{-}DR] \pm d[W] \pm e[HR] \pm f[T] \pm g[TOW]$	2	[25-27]
$r_{corr} = at^b[Cl^{-}DR]^c[[W]/[D]]^d$	3	[28,29]
$r_{corr} = at^b$	4	[27] [30-38]

Where:
r_{corr}: Corrosion rate by loss mass (g m^{-2}).
$[Cl^{-}DR]$: Chloride deposition rate (mg m^{-2}d^{-1}).
$[SO_x^{-}DR]$: Sulphur compounds deposition rate(mg m^{-2}d^{-1}).
$[W]$: Rainfall amount (mm).
$[HR]$: Relative Humidity (%).
$[T]$: Temperature (°C).
$[[W]/[D]]$: Amount of rainfall/number of rainy days.
$[t]$: Time of exposure (months or years).
a, b, c, d, e, f, g: Constants

Atmospheric corrosion of steel-reinforced concrete has not been frequently studied under outdoor exposure conditions in a coastal city located in a tropical island using statistical regressions (Table 1), taking into account other factors that influence in the phenomenon. These factors are: compressive strength, effective porosity, vacuum effective porosity, ultrasonic pulse velocity and free and total chloride content in the surface and at different penetration depths in the concrete. Others factors to consider are: the time of exposure, distance from the sea, concrete covering thickness, as well as, an important evaluation of the atmospheric environment on different types of concrete.

A detailed parametric study involving the critical chloride concentration, structural configuration, distance from the sea, concrete covering thickness and rebar diameter, to understand their effects on chloride ingress into concrete was carried out. Qualitative comparison of damage induced on concrete covering as a result of non-uniform corrosion layer formation around rebar is presented through time-to-corrosion initiation (TCI) profiles [39].

The influence of the atmospheric environment on different types of concrete was the main study of the CYTED project DURACON, conducted throughout 11 Ibero-American countries (Cuba was not included). The initial results showed that in coastal atmospheres, the chloride content in the environment should be considered a decisive factor when evaluating the probability of corrosion of steel reinforced concrete during the first years of study [40, 41]. Chloride deposition on testing devices is due to the salt particles that impact and remain on the apparatus surfaces during the transport of marine aerosol to the inland. The wet candle device is frequently used for this purpose, as part of standardized procedures for measuring the amount of chloride salts captured from the atmosphere on a given exposed area of the apparatus [42, 43].

Cuba is an archipelago with a climate characterized by annual average values of temperature and relative humidity of 25°Cand 75%, respectively. Due to its shape and geographic location, the chloride deposition $[Cl^{-}DR]$ is the main aggressive agent because the of marine aerosol penetration from the sea occur in almost all the national territory [44, 45]. On the northern coast of Havana, specifically in zones very close to the sea, not characterized by the artificial and natural shielding, dissimilar reinforced concrete structures show damage, due to atmospheric corrosion of steel reinforced concrete [46, 47].

The main objectives of the present chapter are: (1) Study the atmospheric corrosion of steel- reinforced concrete following the methodology established for atmospheric corrosion tests of the metallic materials. (2) Determine the corrosivity categories of the atmospheres in different types of concrete in a coastal city located in a tropical island. (3) Determine other factors influencing on atmospheric corrosion of steel-reinforced concrete under outdoor exposure conditions. All these objectives are important in order to design a correct maintenance and protection program on the northern coast of Havana, specifically in zones very close to the sea, not characterized by the artificial and natural shielding.

EXPERIMENTAL PART

Exposure Sites

Seven outdoor exposure sites located at different distances from the sea (m) in an experimental zone of tropical coastal climate of Havana, Cuba were selected (S1-20 m, S2-170 m, S3-600 m, S4-1 356 m, S5-1 762 m, S6-2 364 m and S7-4 911 m).

Havana is located on the north western coast of Cuba (23°07′00″LN and 82°23′00″WL), and is characterized by shielding condition to marine aerosol penetration due to existence of the great high structures (Figure 1).

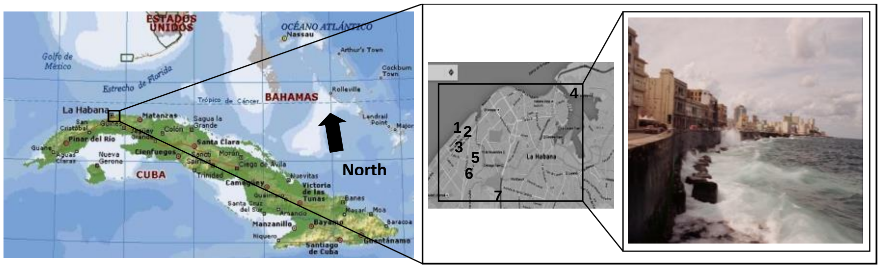

Figure 1. Location of Havana north western coast of Cuban Isle, distribution of outdoor exposure sites in experimental zone. No shielding conditions due to great high structure are present only in the exposure site 1 (S1-20 m).

Every outdoor exposure site was composed by:

- Wooden rack with four atmospheric pollutants devices: Two dry plate devices (150 x 150 mm) for chloride deposition rate determination $[\boldsymbol{Cl^{-}DR}]$ and two cellulose filters plates (150 x 100 mm) for sulphur compounds deposition rate determination $[\boldsymbol{SO_x^{-}DR}]$ (device is sensible to all sulphur compounds presented in air). The wooden racks were oriented toward the sea and were placed at minimum height of 3m from the ground, under a shed to avoid the washing effect of rain.
- Three specimens of reinforced concrete with different water cement ratio (0.4, 0.5 and 0.6) remained for a time of exposure of three years. The first year from October/2007 to September/2008, the second year from October/2008 to September/2009 and the third year from October/2009 to September/2010. Another three probes of each water cement ratio remained in the laboratory with the objective to be used as reference in the comparative analysis of the results.

Outdoor Pollutants

$\boldsymbol{Cl^{-}DR}$ (mg m^{-2} d^{-1}) based on Cuban standard using dry plates device method was determined [48]. Dry plate device consisted in a piece of absorbent cloth of size 150 mm x 150 mm located at 45 degrees to the horizontal and in front to the sea. Two pieces of cloth were used for every site, perfectly cleaned and washed with distilled water. The pieces of cloth were exposed monthly during one year. Chlorides deposited on the pieces of cloth by chemical analysis were determined. The pieces of cloth after retired, were kept into plastic bags up to chemical analysis. Two values of $\boldsymbol{Cl^{-}DR}$ for every month of exposure (in the period October/2007 to September/2008) were obtained: one for device 1 and other for device 2 , for every outdoor exposure site (total = 24). The principle of this method is the same than Wet Candle device described on ISO: 9225:2012 [49]. Outdoor monthly average data (12) were plotted for each month of exposure, as well as annual average data (7 sites) were plotted with respect to distance from the sea.

$\boldsymbol{SO_x^{-}DR}$ (mg m^{-2} d^{-1}) was determined based on Cuban standard using alkaline plates device method [50]. Alkaline plate device consisted in a piece of absorbent cellulose paper of size 150 mm x 100 mm located at 45 degrees to the horizontal and in front to the north direction. Pieces of cellulose paper were immersed in $NaCO_3$ 70% and subsequently dried at a temperature of 60°C on the stove. Two alkaline plates device were used for each test site. After drying, alkaline plates device were exposed on each test site. After retired, alkaline plates device were kept into plastic bags up to chemical analysis. Two data of $\boldsymbol{SO_x^{-}DR}$ for every month of exposure was obtained: one for device 1 and other for device 2for every exposure site, for a total of 24 in one year. The principle of this method is described on ISO: 9225:2012. Outdoor monthly average data (12)were plotted for each month of exposure, as well as annual average data (7 sites) were plotted with respect to distance from the sea.

Annual average deposition rate for both atmospheric pollutants in conjunction with the annual average of relative humidity (RH in %) and temperature (T in °C) to every outdoor exposure site can be used as an indirect estimation of the corrosion rate (r_{corr}in µm y^{-1}) of the metallic materials most used in the construction industry (carbon steel, copper, aluminum and zinc) using dose-response functions established in ISO 9223:2012 standard to estimate corrosivity categories of the atmosphere under outdoor exposure [51].

Meteorological Parameters

Relative humidity and temperature average monthly data determined during three years of study were obtained from the Cuban Meteorological Center, corresponding to exposure site 4 (S4-1 356 m) (Figure1). The wind speed flow was determined from east-northeast to west-northwest directions (wind speed flow coming from the sea).

Reinforced Concrete Specimens

Twenty-four reinforced concrete specimens, eight for each water cement ratio, with straight rectangular prisms form of dimensions 200 mm x 200 mm x 200 mm and concrete mix with water cement ratios of 0.4, 0.5 and 0.6 were elaborated. Two reinforced steel bars with covering thickness of 20 and 40 mm in each probe were placed (Figure 2). Carbon steel molds coupled with screws were used. Molds were previously moistened inside before to pour the mix, and removed it after placed the concrete mix at 24 hours.

Water cement ratios 0.5 and 0.6 and the steel covering thickness of 20 mm are one of the design conditions more frequently used in the construction of reinforced concrete structures in Cuba. The concrete mix used was calculated bearing in mind to obtain a minimum percentage of holes between the fine and coarse aggregates. The composition of the concrete mix was: Ordinary Portland Cement: 365 kg; Havana calcareous sand: 750 kg; Hard limestone gravel (nominal size 19 mm): 1 030 kg. Superplasticizers admix to obtain a concrete mix with fluid consistency and assure a good compaction was used. Abrams cone method for determining the settlement was used. A mix of fluid consistency and good work ability for the three water/cement ratios tested were obtained (Table 2).

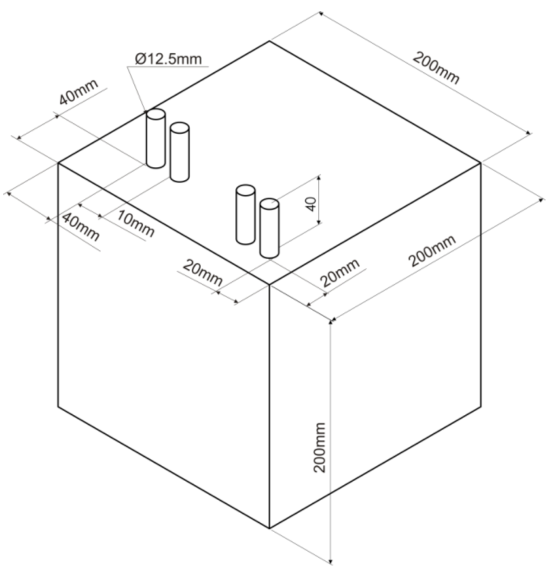

Figure 2. Dimension of reinforced concrete specimen.

Table 2. Water and admix volume used in concrete probes preparation

Water cement ratio	Cone settlement (cm)	Real water volume (l)	Admixure used (%)
0.4	15	148	1.7
0.5	17	186	1.2
0.6	18	222	1.0

Water immersion curing process was used to submit the twenty-four reinforced concrete specimen elaborated during 28 days at room temperature [52].

Carbon steel reinforced bars(d = 12 mm and l = 200 mm) were submitted to chemical cleaning in 36% hydrochloric acid solution to eliminate the poor corrosion products existing on the surface [52]. For a total length of 200 mm, 160 mm were immersed in the concrete mix and the others 40 mm remained in the outdoor exposure conditions to be connected with the instrument and measure the corrosion current intensity. Adhesive tapes as temporal protection against the atmospheric corrosion in outdoor zones were used.

Twenty four single concrete probes in cylindrical form (eight for each water cement ratio d = 150 mm and l = 300mm) and six in straight rectangular form but without steel reinforced bars of the same dimensions (two for each water cement ratio) were elaborated. These specimens were submitted to the same curing process and were used to determine some properties like: compressive strength, effective porosity, vacuum effective porosity and ultrasonic pulse velocity.

Characterization of Concrete Mixes

Concrete mixes with water cement ratios (w c) of 0.4, 0.5 and 0.6 were characterized. The following tests were performed to characterize the concrete mixes physically and mechanically:

Compressive strength (f_{ck} in MPa)-twenty four cylindrical probes (d = 150 mm, l = 300 mm), eight for each w/c ratio [53].

Ultrasonic pulse velocity (*UPV* in m s^{-1})-three concrete specimens (one for each water cement) with straight rectangular prisms form of the same dimensions. The propagation time of the wave transmission was measured using direct method between transmitters [54].

Table 3. Compressive strength (f_{ck}), Ultrasonic pulse velocity (*UPV*), Capillary porosity ($\mathcal{E}_e$) and vacuum capillary porosity ($\mathcal{E}_{ev}$) determined for eight specimens corresponding to three different mixes of w c ratios

w c	$\mathcal{E}_e$ (%)	$\mathcal{E}_{ev}$ (%)	f_{ck} (Mpa)	*UPV* ($m\ s^{-1}$)	**w c**	$\mathcal{E}_e$ (%)	$\mathcal{E}_{ev}$ (%)	f_{ck} (Mpa)	*UPV* ($m\ s^{-1}$)	**w c**	$\mathcal{E}_e$ (%)	$\mathcal{E}_{ev}$ (%)	f_{ck} (Mpa)	*UPV* ($m\ s^{-1}$)
0.4	7.0	16.0	36.8	4 160	0.5	11.6	17.6	30.4	4 109	0.6	19.7	20.4	25.3	3 900
	9.7	16.3	36.7	4 280		9.8	18.0	29.5	4 110		19.9	19.6	25.7	3 910
	7.4	15.9	35.8	4 200		12.3	17.6	30.0	4 170		19.5	20.4	25.8	3 910
	7.2	15.9	36.4	4 290		14.9	19.1	30.3	4 100		21.3	20.0	25.6	3 930
	6.3	16.0	35.3	4 270		15.7	17.5	30.1	4 050		20.6	21.3	25.5	3 930
	6.7	16.1	36.2	4 270		13.5	18.4	31.3	4 070		18.3	20.0	25.8	3 960
	8.6	16.4	36.0	4 240		14.9	17.5	29.8	4 090		17.2	20.8	25.7	3 980
	6.6	16.1	36.5	4 260		14.0	17.8	29.4	4 150		20.2	19.8	25.6	3 970
Av.	*7.4*	*16.1*	*36.2*	*4 246*	*Av.*	*13.3*	*17.9*	*30.1*	*4 106*	*Av.*	*19.6*	*20.3*	*25.6*	*3 936*
S.D	*1.1*	*0.18*	*0.49*	*44.70*	*S.D*	*1.96*	*0.57*	*0.6*	*39.24*	*S.D*	*1.30*	*0.57*	*0.16*	*30.20*
C.V (%)	*14.8*	*1.16*	*1.38*	*1.05*	*C.V (%)*	*14.7*	*3.17*	*1.99*	*0.95*	*C.V (%)*	*6.65*	*20.4*	*0.65*	*0.76*

Capillary porosity ($\mathcal{E}_e$ in %) using Fagerlund procedure [55] and vacuum capillary porosity ($\mathcal{E}_{ev}$ in %). Both procedures described in DURAR Network Members, Manual for Inspecting, Evaluating and Diagnosing Corrosion in Reinforced Concrete Structures [56]. Eight data were obtained for every three different mixes of w/c ratios (Table 3). Capillary porosity and vacuum capillary porosity were determined in specimens of cylindrical form (d = 60 mm, l = 20 mm).

Determination of Chloride Content in Concrete

Determination of chloride content in concrete was carried out only in the exposure site 1 (S1-20 m). Two dust samples weighing 40 g were extracted from the surface, 20 mm and 40 mm of depth. Extraction was carried out for one, two and three years of exposure for each w c ratio (0.4, 0.5 and 0.6). The samples were placed in plastic flasks. The extraction in the surface was made at a depth not lower than 3 mm. A previous cleaning of the drill (diameter of 14 mm) using a synthetic fibers brush was always executed, including changes of probes and changes of depth.

For each dust samples of 40 g, eight values of total and free chloride content (% concrete mass) in 5 g of dust in the surface and for each penetration depth (20 mm and 40 mm) were determined [57, 58]. Solution pH for chloride content determination in concrete always varied between 12.3 and 12.7. Therefore, there was no alteration in pH by the penetration of sulfate ions or carbonation processes that may have occurred within the concrete.

Corrosion Current Intensity

Corrosion current intensity (Ic- μA cm^{-2}) as indicator of the atmospheric corrosion of steel-reinforced concrete, was measured annually; that is to say, the first, second and third year of exposure. Instrument (corrosimeter) GECOR-8TM brand GEOCISA was used, always before the extraction of the dust samples.

The zone of measurement of the reinforced concrete probe that remained in front of the sea was always well moistened. A humidified cloth was placed between the surface of the probe and the sensor of the instrument (guard ring), with the purpose to improve the electric conductivity of the measurement system. The sensor of the instrument was pressed with the hand on the probe in the zone where the reinforced steels bars are located at 20 and 40 mm of covering thickness (Figure 3). The instrument uses the LPR technique with potential range of ±20 mV and sweep speed of 12 mV s^{-1}. The polarization area introduced to the instrument was 65.25 cm^2.

Four data of the corrosion current intensity for each reinforcement steel bar with 20 and 40 mm of covering thickness in the three probes with water cement of 0.4, 0.5 and 0.6 ratio were obtained. Eight data of the corrosion current intensity obtained for each covering depth were plotted versus the time of exposure in the exposure site 1 (S1-20 m).

Annual average data obtained from eight values of the corrosion intensity for each covering depth were plotted at different distances from the sea for third year of exposure.

Data of corrosion current intensity were classified using the intervals established in the DURAR Network in order to determine the initiation time (Ti) and propagation (Tp) of corrosion [56]. The sum of both times allowed to know the useful life for reinforced concrete structures submitted to coastal tropical climate of Havana.

Figure 3. Measurement system used to determine the corrosion current intensity in the reinforced concrete probes.

Scanning Electron Microscopy (SEM)

Scanning electron microscopy tests in two hardened cement paste samples for each water cement ratio, were carried out. Small samples of hardened paste cement, separated mechanically without polishing, were introducing into the microscope camera. Samples were dried first with a manual desiccator and coated with a metallic gold film in ionic gold electron equipment of SPI MODULE SPUTTER COATER of US-made for better scanning electronic. Environmental scanning electron microscope secondary electron of PHILIPS XL 30 ESEM mark of Dutch made was used.

RESULTS AND DISCUSSION

Characterization of the Atmospheric Environment

Analysis of the Relative Humidity-Temperature Complex

The relative humidity and temperature were recorded during the three years of the study. Lower values of relative humidity (RH) and temperature were observed during the months corresponding to winter season. Higher $[Cl^{-}DR]$ is determined during winter season due to entry of cold fronts.

Nevertheless, monthly and annual average data for relative humidity (RHa) and temperature (Ta) are higher than 74% and about 25.0°C respectively (Figure 4).

Zezza and Macri [70] established that after marine aerosol generation, drops equilibrate with the environment and, depending on the temperature and the conditions of RH, these drops can be composed by salt solution having different concentrations or salt crystals when RH falls below 70–74%. Therefore $Cl^{-}DR$and maybe $SO_x^{-}DR$are deposited as salt solutions. Thus, corrosivity categories of the atmospheres increase in the coastal tropical climate in Havana.

Time of wetness data for three years of the study obtained from analysis of the relative humidity-temperature complex were: 3 408 h y^{-1}, 3 120 h y^{-1} and 3 072 h y^{-1} respectively. They classified in the rank 2 $500 < \varepsilon_4 \leq 5\ 000$, as an example of occurrence of outdoor atmospheres in all climates (except for dry and cold climates) ventilated sheds in humid conditions; unventilated sheds in temperate climates. As it is known, the time of wetness is underestimated by the time that the temperature exceeds 0°C and 80% RH.

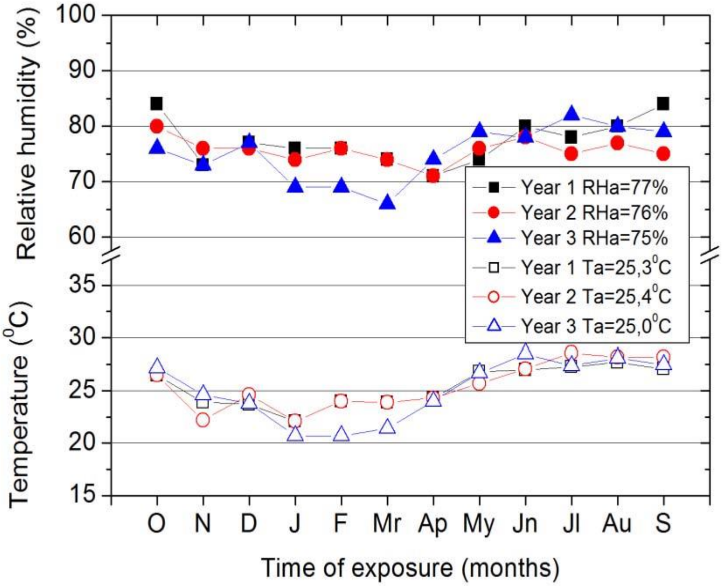

Figure 4. Behavior of monthly RH and temperature during three years of study.

Hence, the environment shall have high (C4), very high (C5) and extreme (CX) corrosivity categories of the atmosphere, particularly for structures located a short distances from the sea without shielding conditions in the city.

Comparative Behavior of $Cl^{-}DR$ and $SO_x^{-}DR$ versus Time of Exposure

$Cl^{-}DR$ and $SO_x^{-}DR$ data show a similar behavior respecting time of exposure.$Cl^{-}DR$on site 1 was analyzed separately due to the large difference between this site and the others (S1-20 m). Higher deposition for both aggressive agents was obtained in the outdoor exposure site 1 (S1-20 m) during the winter season in Cuba (November to March), see Figure 5 a) and b) and Figure 6).

According to relevant data obtained in the Cuban Meteorological Center, corresponding to outdoor exposure site 4 (S4-1 356 m), it is valid to highlight that during the winter season, a total of 17 frontal systems (cold fronts) penetrated in Havana City. Of these fronts, seven were classified as moderate intensity because the maximum wind speed flow sustained was over 9 m s^{-1}.

Thus, the higher deposition for both aggressive agents was obtained precisely during the winter months.

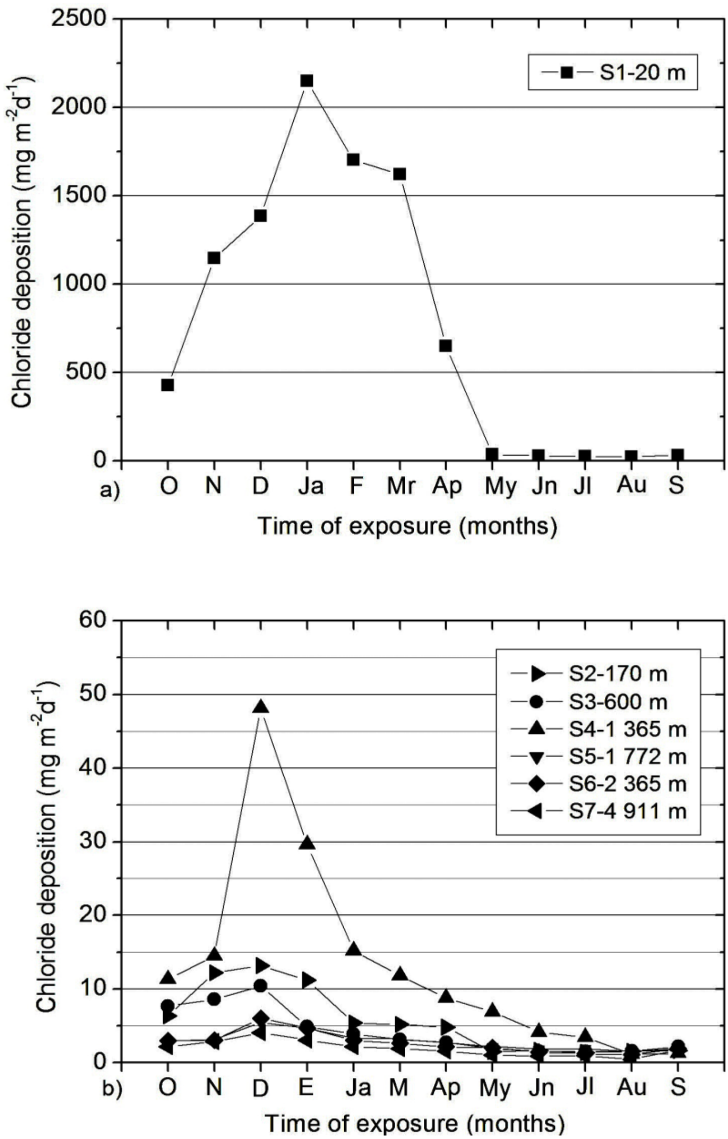

Figure 5. $Cl^{-}DR$ (b) Behavior respect to time of exposure in the summer and winter seasons. $Cl^{-}DR$ (a and b)in the exposure site at 20 m and remaining at different distances from the sea respectively.

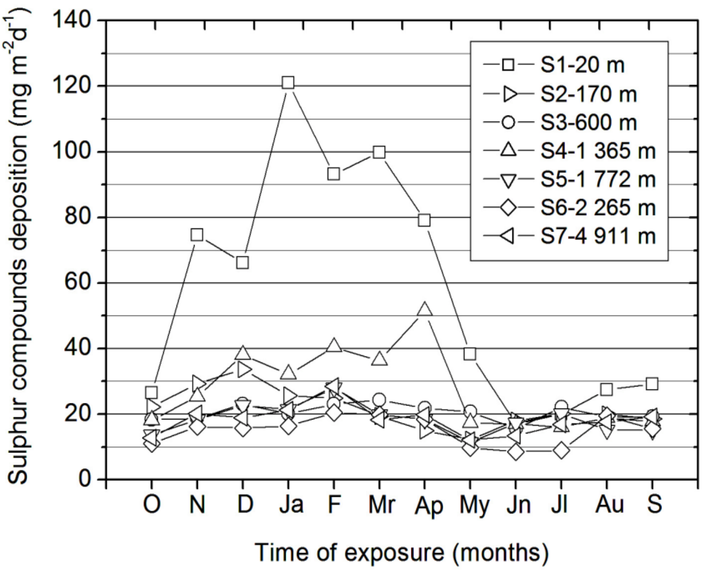

Figure 6. $SO_x^- DR$ (b) Behavior respecting time of exposure in the summer and winter seasons.

Considering the linear regression established by Corvo [31] in the coastal tropical climate of Cuba between dry plate and wet candle test devices for annual average of$Cl^- DR$:

$$[Cl^- DR]_{W.C} = -54.5 + 1.6[Cl^- DR]_{D.P}\ r = 0.98\ p < 0.005 \qquad (1)$$

where:

$[Cl^- DR]_{W.C}$ = annual average determined using wet candle method
$[Cl^- DR]_{D.P}$= annual average determined using dry plate method.

Annual average of $Cl^- DR$ estimated from wet candle method using linear regression (1) in the exposure site 1 (S1-20 m) was1 176.58mg m^{-2}d^{-1}. Annual average determined using Dry plate method was 769.43 mg m^{-2}d^{-1}. Thus for both methods, annual average $Cl^- DR$ is in the range between 300 < S3 ≤ 1 500 according to the classification category established by the ISO 9223-2012 standard. $Cl^- DR$ during the winter months in Cuba was over 1 500 mg m^{-2}d^{-1}respecting dry plate method (Figure 5 a).

The ISO 9225-2012 standard establishes: "Chloride deposition rates determined by the dry plate method and by the wet candle method differ because the kind and shape of deposition surface are different (wet/dry surfaces, cylindrical/plate format of the deposition surface). There is little difference in the deposition rates determined by the two methods at locations with very low deposition rates, i.e., <10 mg $m^{-2}d^{-1}$. On the other hand, at higher chloride deposition rates, the wet candle method gives deposition rates that are approximately twice as high as those given by the dry plate method. Both these measurements give values with low correlation for monthly sampling periods due to the great variation in weather characteristics. A high correlation exists for annual average values ($[Cl^{-}DR]_{W.C} = 2.4[Cl^{-}DR]_{D.P}$)".

Considering the latter correlation, annual average $Cl^{-}DR$from wet candle test device was 1 799.11 mg $m^{-2}d^{-1}$. Data is over 1 500 mg $m^{-2}d^{-1}$according to classification category established by the ISO 9223-2012 standard.

Only in five (>1 176.58 mg $m^{-2}d^{-1}$)and six (>1500 mg $m^{-2}d^{-1}$)outdoor exposure sites in cities having coastal tropical climates around the world, average annual $Cl^{-}DR$was over threshold obtained by the criteria established in ISO 9223-2012, as well as the obtained by linear regression (1) respectively (Table 4).

Table 4. Annual average values of $Cl^{-}DR$ and $SO_x^{-}DR$ in cities with coastal tropical climates around the world

Chloride deposition rate		
Exposure site/Country	**$Cl^{-}DR$ (mg $m^{-2}d^{-1}$)**	**References**
Veracruz/Mexico	1 483.0	[27]
Tuxtla/Mexico	3 378.0	
Cabo Raso/Portugal	1 392,0	[40, 41]
Sriharikota/India	5 000.0	[59]
Cabo Vilano/Spain	1 905.0	[60]
Sulphur compounds deposition		
Exposure site/Country	**$SO_x^{-}DR$ (mg $m^{-2}d^{-1}$)**	**References**
Minatitlan/Mexico	76.35	[27]
Puebla/Mexico	64.6	
Quintero/Mexico	155.0	
Puerto Chaca/Chile	58.0	[61, 62]
Isla Pascua/Chile	73.0	
Petrox/Chile	65.2	
Arica/Chile	99.0	
Leixões/Portugal	69.2	[63]
Bilbao/Spain	81.0	
Alicante/Spain	126.0	

Regarding to $SO_x^- DR$, only in ten outdoor exposure sites located at longer distances from the sea, data was higher in comparison with the outdoor exposure site close to the sea without shielding conditions. Annual average $SO_x^- DR$ in the outdoor exposure site 1 (S1-20 m) was 57.5 mg m^{-2}d^{-1}. Therefore, the northern coastline of Havana without shielding conditions, due to the abundance of high structures, could be considered one of the areas showing most corrosive category of the atmosphere around the world. A significant deterioration is observed, not only in reinforced concrete structures due to atmospheric corrosion on steel reinforced concrete, but also in the structures built with metallic materials more often used in the construction industry (carbon steel, zinc, copper and aluminum).

Comparative Behavior of $Cl^- DR$ and $SO_x^- DR$ Annual Average at Different Distances from the Sea

$Cl^- DR$ and $SO_x^- DR$ annual average versus distance from the sea is represented in Figures. 7 a) and b) as a way to show the significant corrosion aggressivity in the northern coastline of Havana. Datas were fitted to the models: ($Cl^- DR = Cl^- D_0 R + Ae^{-b(x)}$) and ($SO_x^- DR = SO_x^- D_0 R + Ae^{-b(x)}$) respectively. These models are based on a decreasing exponential function of deposition versus distance from the sea. When $Cl^- D_0 R = 0$ in case of chloride deposition, it means that big salt particles originated in the breaking wave's zone are deposited at short distances from the sea in the region under study (Figure7a). It also means that small particles formed in the ocean can travel longer distances and deposited in the land. The parameter A can be considered as $Cl^- DR$in the breaking wave zone, in the coastline.

Similar results respecting $Cl^- DR$ versus distance from the sea have been reported in several coastal zones in the world [64-68]. They did not establish corrosivity categories of the atmosphere to steel reinforced concrete, as well as to metallic materials more used in the construction industry.

According to $Cl^- DR$ annual average (Figure7 a), deposition in the outdoor exposure site 1 (S1-20 m) represents 88% of the total deposited chloride in all exposure sites at different distances from the sea. Therefore, deposition of big salt particles originated in the breaking waves occurs at short distances from the sea. In this region many reinforced concrete structures without shielding conditions are damaged by atmospheric corrosion of steel-reinforced concrete.

On the others hands, it is noteworthy how the value of the exponent b in the model corresponding to $Cl^{-}DR$ annual average was higher (Figure 7 a) and b) respecting $SO_x^{-}DR$. This means that $SO_x^{-}DR$ salt particles coming from the sea and transported in the marine aerosol could settle at higher distances from the sea. The inverse value of b could represent the distance from the sea to which big salt particles were deposited; $b \approx 32$ m and 50 m, for the $Cl^{-}DR$ and $SO_x^{-}DR$ annual average respectively. In the exposure site 1, for the last aggressive agent, deposition is the 32% of the total.

Considerable decrease of$Cl^{-}DR$occurred at a distance from the sea much lower than established by Corvo [31] and Morcillo [69] (between 150 and 200 m) in coastal zones of Cuba and Spain without shielding condition and without fitting models based on a decreasing exponential function of deposition versus distance from the sea.

$SO_x^{-}DR$ is usually produced by industrial or urban sources (mainly composed by SO_2, very aggressive acid gas). Dependence between $SO_x^{-}DR$ and distance from the sea is not obtained frequently. No reports have been found on this subject. It means that one of the main sources of $SO_x^{-}DR$ is the sea (mainly composed by sulphate aerosol). In case of this type of pollutant (Sulphate, SO_2, SO_3, SH_2 and other Sulphur compounds can be included in $SO_x^{-}DR$) sulphate ions can be produced by the sea. When $SO_x^{-}D_0R = 19.95$ it could mean that it is the average deposition determined at a distance starting from 170 m from the sea (Figure 7b). It also implies that sulphate coming from the sea is an important contribution to Sulphur compounds deposition determined in the zone. Really what happens is the incorporation of sulphur compounds to horizontal flow of marine aerosol coming from the sea. sulphate particles show a lower weight and size respecting chloride. It causes them to travel and settle at higher distance from the sea respecting chloride particles.

The device used is sensitive to sulphate deposition from marine aerosol and other sulfur compounds coming from other sources like industry and urban activity. Some industries are located outside the city, as well as the intense automobile traffic.

According to classification ranges of $SO_x^{-}DR$ presented in ISO 9223-2012 standard, it is possible to classify the type of atmosphere at different distances from the sea. The outdoor exposure site close to the sea (S1-20 m) is classified as coastal-industrial (Table 5). This type of atmospheres exercises a high influence on the atmospheric corrosion, not only on steel-reinforced concrete, but also in the metallic materials more use in the construction industry, such as: carbon steel, zinc, copper and aluminum.

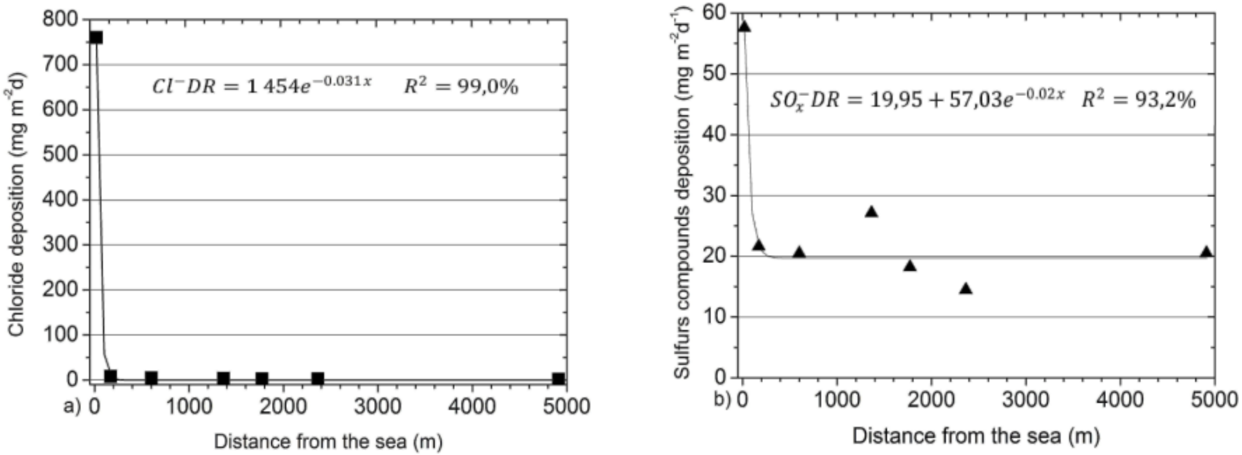

Figure 7. $Cl^{-}DR$a) and $SO_x^{-}DR$ b) annual average behavior respect to distance from the sea.

For the rest of the outdoor exposure sites, the most predominant type of atmosphere was urban due to $SO_x^- D_0 R = 19.95$. Nevertheless, in the outdoor exposure site 4 (S4-1 365 m), the atmosphere is classified as industrial-coastal. Annual average of $SO_x^- DR$= 27.7 mg $m^{-2}d^{-1}$. The outdoor exposure site was located near from Havana Bay where a significant number of industries related to oil refining processes exist (Figure 1).

Corrosivity Category Classification

Corrosivity categories of the atmospheres at different outdoor exposure sites estimated according to dose-response functions presented in ISO 9223-2012 standard and type of atmosphere classification are shown (Table 5).

Table 5. Corrosivity categories estimated for different exposure sites using dose-response functions established by ISO 9223:2012

Exposure site	Carbon steel		Zinc		Copper		Atmospheres
	r_{corr} (µm y^{-1})	Categories (C)	r_{corr} (µm y^{-1})	Categories (C)	r_{corr} (µm y^{-1})	Categories (C)	
S1-20 m	407.16	CX Extreme	21.81	CX Extreme	4.52	C5 Very high	Coastal-industrial
S2-170 m	35.49	C3 Medium	1.84	C3 Medium	1.02	C3 Medium	Urban
S3-600 m	32.24	C3 Medium	1.63	C3 Medium	0.92	C3 Medium	Urban
S4-1 365 m	50.31	C4 High	2.80	C4 High	1.38	C4 High	Industrial-coastal
S5-1 772 m	28.31	C3 Medium	1.36	C3 Medium	0.79	C3 Medium	Urban
S6-2 365 m	26.09	C3 Medium	1.18	C3 Medium	0.71	C3 Medium	Urban
S7-4 911 m	25.48	C3 Medium	1.17	C3 Medium	0.78	C3 Medium	Urban

Corrosivity categories were estimated using the values $Cl^{-}DR_{wc}$ obtained from the relationship already established on ISO 9225-2012 [49] between $Cl^{-}DR$ determined by dry plate and wet candle methods. To use the dose-response functions presented in ISO 9223-2012 standard, data of annual average $Cl^{-}DR$ should be obtained by wet candle method [1].

Aluminum is not included on ISO 9223-2012 standard to calculate the corrosion rate from dose-response functions. Aluminum experiences uniform and localized corrosion. The corrosion rates shown are calculated as uniform corrosion. Maximum pit depth or number of pits can be a better indicator of potential damage. It depends on the final application.

Corrosivity category classification ranges from C3 Medium to C5 Very High (Copper) and from C3 Medium to CX Extreme (Carbon steel and Zinc) are shown. For the outdoor exposure site located at 20 m from the sea (S1-20 m) without shielding conditions, corrosivity categories estimated were C5 Very High for Copper and CX Extreme for Carbon Steel, and Zinc (Table 5).

ISO 9223-2012 standard establishes the parameters used in the derivation of dose-response functions where annual average $Cl^{-}DR$ must fall between 0.4 and 760.5 mg $m^{-2}d^{-1}$. Annual average determined using dry plate method was 769.43 mg $m^{-2}d^{-1}$.

On the other hand, in spite of the large difference of the uncertainty level between estimation (-33% to 55%) and determination (±2%) of corrosivity categories for carbon steel, zinc and copper, the results obtained coincide with those obtained by Corvo [31, 32]. The annual average of corrosion rate in the other outdoor exposure site located at a distance from the sea of 10 m in Havana City and very close to the one selected in this study (S1-20 m) was: for the carbon steel 3 487.7 g m^{-2} (CX Extreme), for zinc 84.3 g m^{-2} (CX Extreme) and for copper 38.8 g m^{-2} (C5 Very High). Therefore, for coastal tropical climate in Havana particularly on the northern coast without shielding conditions, under coastal-industrial atmosphere, corrosivity categories of the atmospheres obtained from estimation and evaluation for the metallic material more used in the construction industry coincide. Hence, a high level of deterioration in the reinforced concrete structures, as well as in the structures built with the metallic material more used in the construction industry from atmospheric corrosion phenomenon exists.

From the outdoor exposure site located at a distance from the sea of 170 m (S2-170 m), corrosivity category estimated was C3 Medium, except for outdoor exposure site located a distance from the sea of 1 365 m (S4-1 365 m) where corrosivity categories estimated was C4 High. Annual average of corrosion rate to carbon steel was 512.6 g m^{-2} (C4 High) for the last outdoor exposure site.

There is a sudden change of corrosivity category of the atmosphere between outdoor exposure site 1 (S1-20 m) and 2 (S2-170 m) (Table V). Higher corrosivity category of the atmospheres from the exposure site 2 and maybe 3 (S3-600 m) was expected, but it did not happen.

The zones of corrosivity categories of the atmospheres CX and C5 (S1-20 m) are shorter in comparison with data reported for zones without shielding condition up to a distance from the sea of 1 km in the north shoreline (Atlantic Ocean) in the coastal tropical climate of Cuba [71, 72]. The specifications related with the Map of corrosion aggressivity of the atmosphere in Cuba were taken into account in the elaboration of Cuban Standards to establish the requirements of durability and useful life of the reinforced concrete structures in order to ensure adequate primary protection provided by the concrete cover to steel reinforcement.

Nevertheless, as result of this study, it seems that shielding conditions in coastal tropical climate in Havana influences on decrease of corrosivity categories of the atmospheres, aspect that must be included in the standards by durability and useful life in any coastal city around the world of high constructive potential.

Analysis of the atmospheric corrosion versus time of exposure the outdoor exposure site 1 (S1-20 m) for covering thickness of 20 mm, atmospheric corrosion of steel -reinforced concrete increases slightly versus time of exposure for water cement ratio 0.4. The increase in atmospheric corrosion rate was higher for concretes of water cement ratio 0.5 and 0.6 (Figure 8a).

Atmospheric corrosion of steel-reinforced concrete increase was less significant for covering thickness of 40 mm. In the case of concrete of water cement ratio 0.4, atmospheric corrosion did not increase with time of exposure up to three years (Figure 8 b).

Atmospheric corrosion rate versus time of exposure was higher when covering thickness was20 mm. No reports have been found about the influence of covering thickness, water cement ratio and time of exposure in atmospheric corrosion of steel-reinforced concrete under outdoor exposure conditions in coastal tropical climate, in a coastal-industrial atmosphere, without shielding conditions and under corrosivity categories of the atmospheres C5 and CX (obtained from estimation and evaluation of corrosion). An early deterioration in reinforced concrete structures due to atmospheric corrosion on steel-reinforced concrete could be expected.

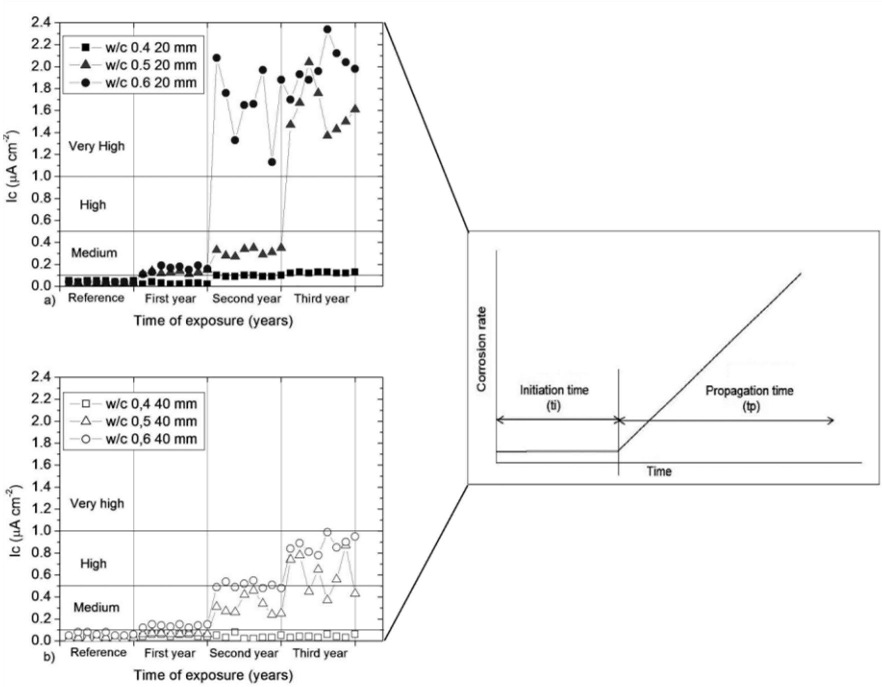

Figure 8. Behavior of atmospheric corrosion of reinforced steel vs the time of exposure and water cement ratio. Covering thickness of 20 mm a). Covering thickness of 40 mm b). Tutti's model c).

Table 6. Fitted regressions for values of atmospheric corrosion in the time of exposure

Covering thickness 20 mm n = 24					Covering thickness 40 mm n = 24			
w c	**Regression** $r_{corr} = at^b$	**r**	**R^2 (%)**	**p**	**Regression** $r_{corr} = at^b$	**r**	**R^2 (%)**	**p**
0.4	$r_{corr} = 0.02t^{1.49}$	0.95	91.0	0.0000	-	-	-	-
0.5	$r_{corr} = 0.11t^{2.15}$	0.94	98.0	0.0000	$r_{corr} = 0.06t^{1.72}$	0.99	98.0	0,0000
0.6	$r_{corr} = 0.18t^{2.43}$	0.94	81.0	0.0000	$r_{corr} = 0.14t^{2.01}$	0.99	98.0	0,0000

Atmospheric corrosion rate and time of exposure data was fitted to regression equation $r_{corr} = at^b$. It has been used in several atmospheric corrosion researches [27] [30-38]. Good fitness was obtained for all water cement ratio (w c) excepting 0.4 at covering thickness 40 mm (Table 6). It is very interesting to note the value of *b* coefficient.

Morcillo et al. [73], states that when b coefficient is close to 0.5 it could be related to an ideal diffusion controlled mechanism when all the corrosion products remain on the metal surface. This situation seems to occur in slightly polluted inland atmospheres. On the other hand, b values higher than 0.5 arise due to acceleration of the diffusion process (e.g., as a result of rust detachment by erosion, dissolution, flaking, cracking, etc.). This situation is typical of marine atmospheres, even those with low chloride contents. Conversely, b values lower than 0.5 could be interpreted as a decrease in the diffusion coefficient with time through recrystallisation, agglomeration and compaction of the rust layer. In the special case when $b = 1$, the mean atmospheric corrosion rate for 1-year exposure is equal to a, the intersection of the line on the bilogarithmic plot with the abscissa for $t = 1$ year. There is no physical sense in $b > 1$, as $b = 1$ is the limit for unimpeded diffusion (high permeable corrosion products or no layer at all). Values of $b > 1$ occur practically as exceptions, for example, due to outliers in the weight loss determinations. As a rule, $b < 1$, b coefficient could be used as an indicator of the physicochemical behavior of the corrosion layer and hence its interactions with the atmospheric environment. The value of b would thus depend both on the metal concerned, the local atmosphere and the exposure conditions.

If $b > 1$ (Table 6), it indicates a marked acceleration of atmospheric corrosion of steel reinforced concrete versus time of exposure according to the fitted regression. The values of b were higher than those usually obtained for atmospheric corrosion of carbon steel ($b = 1.10$) under heat trap conditions [74, 75], as well as for the same metallic material ($b = 1.09$, $b = 1.98$, $b = 1.38$) in outdoor exposure conditions, in both cases in coastal tropical climate of Cuba [28, 31-33]. Values of b coefficient were higher also than those obtained for atmospheric corrosion of carbon steel in outdoor exposure conditions in coastal tropical climate of India ($b = 0.49$) [34].

Values of b have been also higher in the evolution of atmospheric corrosion of carbon steel with exposure in severe marine atmospheres in: Wanning, China ($b = 1.79$) [77], Arraialdo Cabo, Brazil ($b = 1.76$) [33].

However, values of b in atmospheric corrosion of carbon steel were very similar in a tropical marine environment of China [35]($b = 2.15$, b = 2. 43) for water cement ratio 0.5 and 0.6 for covering thickness 20 mm and water cement ratio 0.6, covering thickness 40 mm (Table 6).

Values of $b > 1$, indicating a marked acceleration of atmospheric corrosion of carbon steel due to high amount of $Cl^{-}DR$in coastal exposure site.

The marked acceleration of atmospheric corrosion on steel-reinforced concrete could be due to electrochemical corrosion process itself under the influence of a high $Cl^{-}DR$in coastal tropical climates like Cuba, under coastal-industrial atmosphere and corrosivity categories of the atmospheres C5 and CX. An electrochemical mechanism that has been widely accepted is the following [56]:

(a) Dissolution of iron at the anodic sites (anodic half-cell)

$$2Fe + 6Cl^{-} \rightarrow 2FeCl_3 + 4e^{-} \tag{I}$$

$$FeCl_3^{-} + 2OH \rightarrow Fe(OH)_2 + 3Cl^{-} \tag{II}$$

(b) Reaction of dissolved oxygen in the pore water with the electrons on the cathode (cathodic half-cell)

$$2H_2O + O_2 + 4e^{-} \rightarrow 4OH^{-} \tag{III}$$

Due to Cl^{-} ion remain unchanged in this process and corrosion does not halt by the high iron content in the carbon steel vicinity, the process can continue by itself autocatalytically. The presence of water depends on concrete manufacturing processes (curing water), as well as its exposure in coastal climate. It is characterized by high relative humidity, particularly in concrete of wc ratios 0.5 and 0.6 which are characterized by high effective porosity [76] (Table 3).

It seems that atmospheric corrosion of steel reinforced concrete can be studied following the methodology based in fitting to equation regression $r_{corr} = at^{b}$always when corrosivity categories of the atmospheres are C5 and CX under coastal-industrial atmosphere.

Atmospheric corrosion of steel reinforced concrete increases with the time of exposure, allowing to establish the useful life of the project for structures that are intended to build under outdoor exposure conditions for coastal tropical climate of Cuba without shielding condition under coastal-industrial atmosphere and corrosivity categories of the atmospheres C5 and CX.

Useful life was calculated taking into account the sum of initiation time (t_i) and propagation time (t_p) of atmospheric corrosion of steel reinforced concrete in years according to specifications of Tutti´s model (Figure 8c).

Initiation time was considered when atmospheric corrosion current falls in the range 0.1-0.5 µA cm^{-2}, corresponding to medium level. Propagation time was considered when atmospheric corrosion current falls in the range 0.5-1.0 µA cm^{-2}, linked to high corrosion level and data above this value (> 1.0 µA cm^{-2}) indicates a very high corrosion level (Figure 5 a) and b), according to ranges established in DURAR Network. Initiation time (t_i), propagation time (t_p) and useful life (U_L) for different concrete and covering thickness are shown (Table 7).

Useful life of reinforced concrete structures built with water cement ratio 0.5 and 0.6 does not exceed the five years for both covering thickness in coastal tropical climate of Cuba without shielding conditions, under coastal-industrial atmosphere and corrosivity categories of the atmospheres C5 and CX.

The end of useful life of project for reinforced concrete structure considered in Cuba is five years, the times after are called: service useful life, last useful life and residual useful life. Intensive and costly repair works are executed with the purpose of return the esthetics, functionality and especially security to reinforced concrete structures.

Table 7. Initiation time (t_i), propagation time (t_p) and useful life (U_L) for different concrete and covering thickness

water cement ratio	Covering thickness 20 mm			Covering thickness 40 mm		
	t_i (years)	t_p (years)	U_L (years)	t_i (years)	t_p (years)	U_L (years)
0.4	3	< 20	±23	-	-	-
0.5	1	3	4	2	3	5
0.6	1	2	3	1	2	3

Results were somewhat similar to those obtained in the CYTED project DURACON, conducted throughout 11 Ibero-American countries (without Cuba) [40, 41]. Initiation time of the atmospheric corrosion of steel- reinforced concrete for water cement ratio 0.65 was one year at a covering thickness 20 mm in the exposure site located in Cabo Raso Portugal at a distance from the sea about 20 m without shielding conditions. Corrosivity categories of the atmospheres were very high for the metallic materials more used in the construction study.

Initiation time for water cement ratio 0.4 and covering thickness 20 mm was reached at three years; however, there is a high probability that propagation time could be reached before 20 years because b values were higher to 1 in the fitted regression $r_{corr} = at^b$. A useful life ± 20 years could be expected. Initiation time was not reached for covering thickness40 mm during the three years of study (Table 7). Therefore, reinforced concrete structures submitted to corrosivity categories of the atmospheres C5 and CX under coastal-industrial atmospheres without shielding condition should be built tacking account as requirements for durability and useful life water cement ratio equal or less 0.4 for minimum covering thickness 40 mm. Thus, costly maintenance and repair works are extended in the time of exposure. The guarantee of a good placement, compaction and curing of concrete it must be considered on site.

The rapid appearance of initiation time is indicative of Cl^{-}arrival to reinforcement steel causing the breakdown of the passive layer, as well as, the start of maintenance works in order to prevent that atmospheric corrosion of steel reinforced concrete increase its development over time of exposure.

On the other hand also confirms the poor quality of concrete for water cement ratios 0.5 and 0.6 where values of porosity ($\mathcal{E}_e$) were higher than 10% (13.3% and 19.6% respectively) although values of ultrasonic pulse (UPV) have indicated a high concrete quality (4 106 m s^{-1} and 3 936 m s^{-1} respectively) according to ranges established in DURAR Network.

Visual Observation of Reinforced Concrete Probes in the Outdoor Exposure Site 1

During the third year of exposure, in the outdoor exposure site 1 (S1-20 m), fissures and cracks are observed in the reinforced concrete probes of water cement ratios 0.5 and 0.6, caused by atmospheric corrosion of steel reinforced concrete. The cracks caused by oxides expansion perpendicularly to reinforced concrete probes surface was higher for covering thickness 20 mm (Figure 9).

Visual observation confirms that crack propagation time in reinforced concrete probes of water cement ratio 0.5 and 0.6, exposed during two and three years, respectively, for both covering thicknesses, corresponds with the cracks appearance in outdoor exposure conditions.

No formation of fissures and cracks in the reinforced concrete probes of water cement ratio 0.4 confirm the propagation time estimated in20 years for covering thicknesses 20 mm and 40 mm under outdoor exposure conditions for coastal tropical climate of Cuba without shielding conditions, in a coastal-industrial atmosphere and under corrosivity categories of the atmospheres C5 and CX.

A higher penetration of aggressive agents like Cl^{-}occurs due to cracks. Thus, atmospheric corrosion of steel reinforced concrete increases (values of b > 1) accelerating the deterioration of reinforced concrete structure. A good protection as physical barrier between atmospheres and reinforced steel is not guaranteed using concrete having water cement ratios 0.5 and 0.6 for both covering thickness tested. The cracks appearance also confirm that reinforced concrete structure built with concrete of water cement ratio 0.5 and 0.6 does not exceed five years of useful life. Reinforced concrete structures begin to lose its features and initial design conditions like aesthetics, functionality and security. The cracks presence is a direct indicator of the end of useful life project. A period of residual life is initiated. Thus costly repairs works are increased.

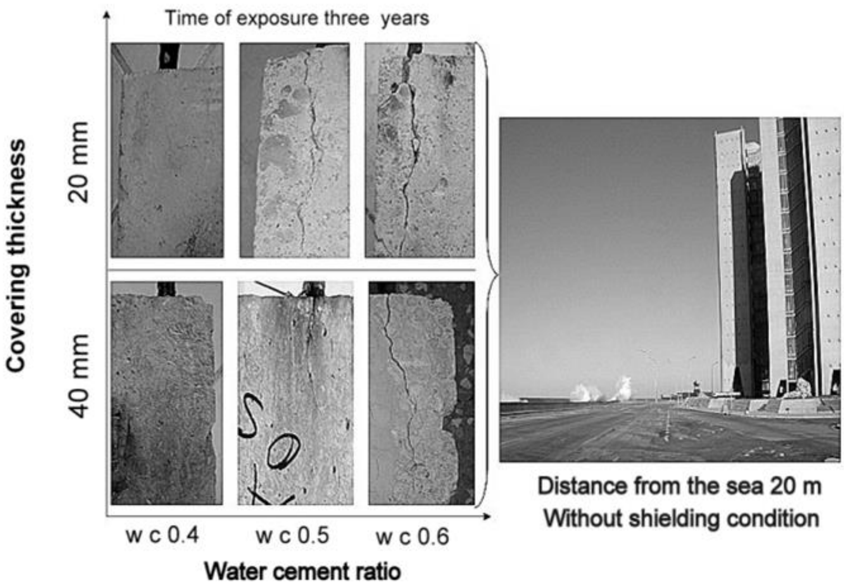

Figure 9. Visual observation of reinforced concrete probes in the outdoor exposure site 1.

Factors Influencing in Atmospheric Corrosion of Steel Reinforced Concrete

It is interesting to show the influence of other physico-mechanical, physico-chemical and chemical factors (directly linked with the increase of water cement ratio) in the atmospheric corrosion of steel reinforced concrete exposed in Cuban outdoor conditions.

These factors are:

- Compressive strength [f_{ck}in MPa] and Ultrasonic pulse speed [UPV in m s^{-1}] decreases as physicomechanical and physicochemical factors also decrease (Table 3).
- Capillary porosity [$\varepsilon_e$in %] using Fagerlund procedure and capillary porosityvacuum [ε_{ev}in %] increase as physicochemical factorsalso increase (Table 3).
- Total [Cl_{ts}] and free [Cl_{fs}]chloride content increase in the surface; total chloride content at 20 mm and 40 mm of depth (Cl_{t20-40}) increase and free chloride content increase too at the same depth (Cl_{f20-40}), all in % concrete mass.

The influence of all factors was shown through multiple regressions (Table 8). The influence of physico-mechanical and physico-chemical factors on atmospheric corrosion of steel reinforced concrete was demonstrated by the following multiple regression:

$$I_c = a \pm b[f_{ck}] \pm c[\varepsilon_e] \pm d[\varepsilon_{ev}] \ \pm e[UPV] \tag{2}$$

On the other hand, the influence of chemical factors was demonstrated through the following multiple regression:

$$I_c = a \pm b\left[Cl_{fs}\right] \pm c[Cl_{ts}] \pm d[Cl_{t20-40}] \ \pm e\left[Cl_{f20-40}\right] \tag{3}$$

The sum of both regression models (3) permits to show if atmospheric corrosion of steel reinforced concrete in a coastal city located in a tropical island without shielding conditions could be influence by chemical, physico-chemical and physico-mechanical factors or a synergistic effect as happened in the atmospheric corrosion research for the metallic materials more used in the construction industry:

$$I_c = a \pm b[f_{ck}] \pm c[\varepsilon_e] \pm d[\varepsilon_{ev}] \ \pm e[UPV] \pm f\left[Cl_{fs}\right] \pm g[Cl_{ts}] \pm \ h[Cl_{t20-40}] \pm \ i\left[Cl_{f20-40}\right] \tag{4}$$

It is valid to reiterate that the analysis was carried out for each year of exposure (first year, second year and third year) in function of an increase in water cement ratio.

The three models in function of water cement ratio increase were fitted for each year of study. It was necessary the simplification of each models (Table 8) for the purpose to show the factors having more influence in the atmospheric corrosion of steel reinforced concrete in outdoor exposure conditions, for coastal tropical climate without shielding conditions (S1-20 m), under coastal-industrial atmosphere and corrosivity categories of the atmospheres C5 and CX (obtained from estimation and evaluation) for the metallic materials more commonly used in the construction industry.

It can be appreciated, in relation to regression2, how compressive strength $[f_{ck}]$decrease was the main factor influencing in the atmospheric corrosion of steel reinforced concrete, principally to covering thickness of 20 mm followed by the effective porosity $[\varepsilon_e]$ increase for both covering thickness. Ultrasonic pulse velocity $[UPV]$ increases too, during the three years of study (Table 8).

It is important to obtain concretes with a good compaction and compressive strength high ($f_{ck} \geq 35$ Mpa) before undergoing environmental exposure conditions principally for coastal tropical climate without shielding conditions (S1-20 m) under coastal-industrial atmosphere and corrosivity categories of the atmospheres C5 and CX in order to obtain terms of useful life higher than 50 years. If no, an increase in time of costly maintenance and repair works in the structures takes place. The fact to have a concrete with a compressive strength about 30 Mpa (water cement ratio 0.5) does not ensure adequate durability, as well as, terms of useful life higher than50 years (Figures 8 and 9). Concrete with water cement ratio 0.5 could present average values of effective porosity around 13% (Table 3). As is well known, quality of reinforced concrete is moderate if effective porosity values are over 10%. The need to obtain concretes of water cement ratio 0.4 with effective porosity below 10% (7%) and compressive strength equal and or perhaps slightly higher than 35 Mpa is confirmed. It is very necessary to consider as fundamental elements onsite the warranty of good placement, compaction, vibration, projection and curing of concrete.

The fact that ultrasonic pulse speed is included in the regression (1) fitted at covering thicknesses of 20 and 40 mm in the second and third years of study does not mean that this factor or parameter is reliable to establish terms of useful life higher than 50 years (Table VII). Although average data of this important parameter indicated generally high and durable qualities of concrete due to the average higher than 3 000 m s^{-1} (Table III), a notable atmospheric corrosion of steel reinforced concrete in probes of water cement ratio 0.5 and 0.6 for both covering thicknesses is observed (Figure 9).

Table 8. Multiple and linear regression where factor most influence in atmospheric corrosion of steel reinforced concrete are showed

First year n = 24				
Covering thickness 20 mm			Covering thickness 40 mm	
No.	**Regression**	**R^2 (%)**	**Regression**	**R^2 (%)**
1	$I_c = 0.49 - 0.012[f_{ck}]$	84	$I_c = 0.01 + 0.006[\varepsilon_e]$	82
2	$I_c = 0.08 + 0.76[Cl_{t20}] + 1.88[Cl_{f20}]$	89	$I_c = 0.09 + 0.93[Cl_{t40}] + 1.79[Cl_{f40}]$	92
3	$I_c = 0.08 + 0.76[Cl_{t20}] + 1.88[Cl_{f20}]$	90	$I_c = 0.09 + 0.93[Cl_{t40}] + 1.79[Cl_{f40}]$	92
Second year				
1	$I_c = 0.49 + 0.012[\varepsilon_e]$	91	$I_c = 3.58 - 0.02[f_{ck}] + 0.0003[UPV]$	93
2	$I_c = 2.84 + 1.92[Cl_{t20}] + 2.84[Cl_{f20}]$	97	$I_c = -0.64 + 7.13[Cl_{t40}] + 2.37[Cl_{f40}]$	92
3	$I_c = 3.48 - 0.14[f_{ck}] + 2.99[Cl_{t20}]$	97	$I_c = 1.60 + 0.01[\varepsilon_e] + 0.66[Cl_{t40}]$	95
Third year				
1	$I_c = 0.49 - 0.012[f_{ck}] - 0.002[UPS]$	86	$I_c = 2.93 - 0.07[f_{ck}]$	91
2	$I_c = -1.81 + 0.87[Cl_{fs}] + 3.49[Cl_{t20}]$	96	$I_c = -0.66 + 2.83[Cl_{ts}] + 1.73[Cl_{f40}]$	89
3	$I_c = 1.89 - 0.08[f_{ck}] + 2.54[Cl_{t20}]$	97	$I_c = 2.93 - 0.07[f_{ck}] + 1.08[Cl_{t40}]$	91

No report have been found showing the influence of physico-mechanical, physico-chemical and chemical factors on atmospheric corrosion of steel reinforced concrete in outdoor exposure conditions for coastal tropical climate without shielding conditions. However, strength and durability characteristics of reinforced concrete structures are seriously affected by the action of environmental factors such as acid rain, alternate wetting and drying, temperature variations and ground moisture. Considering the fall in compressive strength from 32.1 N mm^{-2} to 23.35 N mm^{-2} corresponding to the second and final coring tests, up to 27.6% strength loss could therefore be registered in the concrete of an exposed structure within a period of 5 years. A 7% ultimate strength loss in exposed steel reinforcement may occur within similar years of exposure [78].

On the others hand, an experimental work was dedicated to characterize the porosity of the concrete covering zone using the capillary absorption test, and establishing the links between open porosity characterized by the initial absorption, the compressive strength and carbonation depth. The correlations obtained between the amount of water absorbed in 1 h, the carbonation depth at 180 days and the compressive strength at 28 days were acceptable [79].

In order to total $[Cl_{ts}]$ and free $[Cl_{fs}]$ chloride content increase in the surface, as well as, total chloride content at 20 mm and 40 mm depth (Cl_{t20-40}) increase and free chloride content increase too at the same depth (Cl_{f20-40}) (regression 3) it is noteworthy how atmospheric corrosion of steel-reinforced is not only influenced by an increase in free chloride content (Cl_{f20-40}), but also by total chloride content (Cl_{t20-40}) increase at 20 mm and 40 mm depth, during the three years of study (Table 8).

A marked difference between free chloride content (Cl_{f20-40}) increase and total chloride content (Cl_{t20-40}) increase at 20 mm and 40 mm depth in atmospheric corrosion of steel reinforced concrete was not showed. The free chloride content has been considered as one of the main factors in the atmospheric corrosion of steel reinforced concrete mainly under laboratory and outdoor accelerated conditions.

It is confirmed, that total chloride content (Cl_{t20-40}) increases in function of water cement ratio, it is a very reliable indicator about the initiation and propagation of atmospheric corrosion in steel reinforced concrete under outdoor exposure condition. The local pH decrease in the pore solution (up to 9) is linked to localized corrosion (pitting corrosion) due to electrochemical reaction between free chlorides and ferric ions (I) results in the break of the ionic bond between the chlorides bonded chemically with the chemical compounds of cement. Therefore, these chloride ions (in the pore solution) are included in the total chloride content determined in the whole mass of the concrete.

On the others hand, the presence of an increase in total $[Cl_{ts}]$ and free $[Cl_{fs}]$ chloride content in the surface during the third year of study is observed (Table 8). Therefore, the need to apply secondary protection systems of high efficiency to increase de durability and the useful life of the reinforced concrete structure is showed. The secondary protection systems based on acrylic paintings have showed a high efficiency in the reinforced concrete structure undergoing environmental exposure, conditions occurring principally for coastal tropical climate without shielding conditions [46].

From the sum of both regression models (regression 4), it is seen how the free chloride content (Cl_{f20-40}) increase and total chloride content (Cl_{t20-40}) increase were the most influential factors in the atmospheric corrosion of steel reinforced concrete during the first years of study (Table 8). This result is equivalent to the rapid arrival of chloride ions at the surface of reinforcing steels located in the built structure having concrete of high water cement ratio (between 0.5 and 0.6).

However, a combination between physico-mechanical and chemical factors, as well as, between physico-chemical and chemical factors begins at the second year of study (Table VII). Atmospheric corrosion of steel reinforced concrete not only is influenced by an increase in total chloride content at 20 mm and 40 mm depth (Cl_{t20-40}). Compressive strength [f_{ck}in MPa] decreases for covering thickness 20 mm and Capillary porosity [$\varepsilon_e$in %] increase using Fagerlund procedure.

A combination between compressive strength [f_{ck}in MPa] decrease and total chloride content (Cl_{t20-40}) increase for both covering thickness tested influenced in the atmospheric corrosion of steel reinforced concrete during three year of study.

No report have been found showing the influence of total and free chloride content increase and compressive strength [f_{ck}in MPa] decrease for covering thickness 20 mm and 40 mm in the atmospheric corrosion of steel reinforced concrete at three years of exposure.

Regarding regression (2) and (4), compressive strength [f_{ck} in MPa] decrease has been the most influencing factor in the atmospheric corrosion of steel reinforced concrete. Compressive strength [f_{ck}in MPa] decrease is a factor to take into account before building a structure under coastal-industrial atmosphere and corrosivity categories of the atmospheres C5 and CX (obtained from estimation and evaluation) for the metallic materials more commonly used in the construction industry. Hence, the importance of obtaining concretes of water cement ratio 0.4 with compressive strength 35 Mpa or higher.

Behavior of Atmospheric Corrosion of Steel Reinforced Concrete at Different Distances from the Sea

Annual average data obtained from eight values of atmospheric corrosion of steel reinforced concrete (corrosion intensity) for each covering thickness were plotted at different distances from the sea after three years of exposure (Figure 10). The behavior to annual average $Cl^{-}DR$versus distance from the sea is similar. No reports have been found about the behavior of atmospheric corrosion of steel-reinforced concrete at different distances from the sea considering the water cement ratio and covering thickness.

Atmospheric corrosion of steel-reinforced concrete showed a considerable decrease between the exposure site 2 (170 m) and 3 (600 m) mainly for concretes of water cement ratio 0.5 and 0.6 for both covering thickness tested.

Steel-reinforced concrete keeps in its passive state at a distance from the sea of 170 m. Atmospheric corrosion of steel reinforced concrete did not increased with the time of exposure mainly for reinforced concrete of water cement ratio 0.5 and 0.6 in both covering thickness tested (Figure 10).

Annual average of atmospheric corrosion rate remained below 0.1 µA cm^2 for reinforced concrete probes having water cement ratio 0.4 and covering thickness 40 mm for all exposure sites located at different distance from the sea. Annual average determined for references probes of water cement ratio 0.4 is also shown (Figure 10).

The placement of reinforcing steel at covering thickness 40 mm in reinforced concrete with water cement ratio 0.4 assures a better primary protection against atmospheric corrosion under coastal-industrial atmosphere and corrosivity categories of the atmospheres C5 and CX.

The primary protection of reinforced steel based on the quality of the concrete covering thickness is the most employed in the world. The primary protections lead to very favorable economical results in the durability and useful life increase in the reinforced concrete structures. Concretes as primary protection must possess a good placement, compaction, vibration, projection and curing. The combination between a good primary protection and secondary protection systems based on acrylic paintings have showed a high efficiency in the reinforced concrete structure undergoing environmental exposure conditions principally for coastal tropical climate without shielding conditions [46].

The behavior of atmospheric corrosion of steel-reinforced concrete at different distances from the sea allows showing that reinforced concretes of water cement ratios 0.4, 0.5 and 0.6 for both covering thickness tested show resistance to high (C4, industrial-coastal atmosphere)and medium (C3, urban atmospheres) corrosivity categories of the atmospheres(Table 5). Chlorides ions do not reach reinforcing steels to start and develop the atmospheric corrosion.

Another deterioration phenomenon such as efflorescence have been the main cause of steel reinforced concrete corrosion in the structure at 170 m of distance from the sea in Havana City [46]. The use of sea sand has also been another factor in the corrosion of steel reinforced concrete.

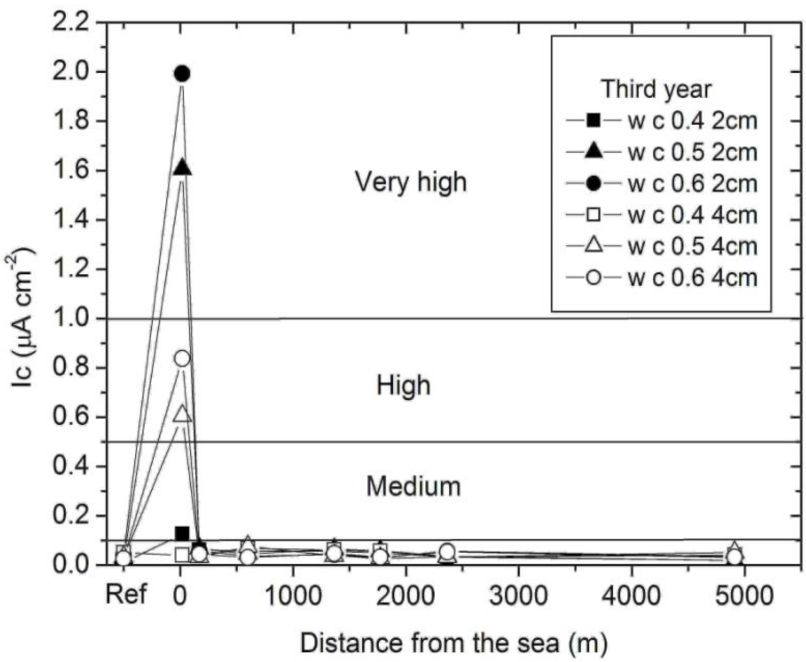

Figure 10. Behavior of atmospheric corrosion of steel reinforced concrete at different distances from the sea after three years of exposure.

Corrosivity Categories of the Atmospheres at Different Types of Concrete in Havana City

Behavior of atmospheric corrosion of steel reinforced concrete in the time of exposures and at different distances from the sea, as well as the behavior of $Cl^{-}DR$ at different distance from the sea and confirmed with visual observation of reinforced concrete probes, allowed determining corrosivity categories of the atmospheres at different types of concrete in Havana City (Table 9).

Corrosivity categories of the atmospheres extreme (CX) for the metallic materials more commonly used in the construction industry in the exposure site 1 (S1-20 m without shielding condition)should be considered for reinforced concrete of water cement ratio 0.5 and 0.6 and covering thickness tested during three years of exposure. Corrosivity categories of the atmospheres very high (C5) for reinforced concrete of water cement ratio 0.4 and covering thickness 20 mm should also be considered (Table 9).

Corrosivity categories of the atmospheres regarding reinforced concrete having water cement ratio 0.4 and covering thickness 40 mm can be considered low (C2). Initiation time of atmospheric corrosion of steel reinforced concrete was not reached after three years of exposure.

Corrosivity category of the atmosphere low (C2) is expected at a distance from the sea of 170 m for reinforced concrete having water cement ratios of 0.4, 0.5 and 0.6 for both covering thickness tested (Table 9).

Table 9. Corrosivity categories of the atmospheres at different types of concrete in Havana City

Exposure site (m)	Water cement ratio					
	0.4		0.5		0.6	
	Covering thickness					
	20 mm	40 mm	20 mm	40 mm	20 mm	40 mm
S1-20	C5	**C2**	CX	CX	CX	CX
S2-170	C2	C2	C2	C2	C2	C2
S3-600	C2	C2	C2	C2	C2	C2
S4-1 365	C2	C2	C2	C2	C2	C2
S5-1 772	C2	C2	C2	C2	C2	C2
S6-2 365	C2	C2	C2	C2	C2	C2
S7-4 911	C2	C2	C2	C2	C2	C2

Corrosivity categories of the atmosphere obtained for the metallic materials more commonly used in the construction industry differs (Table V) in comparison of corrosivity categories determined for different types of concrete in Havana City at a distance from the sea of 170 m (Table 9). A good primary protection against atmospheric corrosion for concrete of water cement ratio 0.5 and 0.6 for both covering thickness tested is insured.

There is a sudden change of corrosivity category of the atmosphere between exposure site 1 (S1-20 m) and 2 (S2-170 m) (Table 9) as happened for the metallic materials more commonly used in the construction industry (Table 5). The shielding conditions also influence on corrosivity categories of the atmospheres decrease for reinforced concrete. This aspect must also be included in the durability standards respecting useful life in any coastal city around the world of high constructive potential with shielding conditions.

Scanning Electron Microscopy Observation

Observations in the hardened concrete paste samples by SEM confirmed that when water cement ratio increases, the number of capillary pores increases too (Figure 11 a), b) and c).

It was appreciated how in concrete with water cement ratio 0.4 there was no appreciable capillary pores formation. It was necessary to increase magnification during the test performance (Figure 11 a). However, in concretes with water cement ratio 0.5 and 0.6 it was easily observed capillary pores formed around 175 μm and 250 μm long respectively (Figure 11 b and c).

The observed microstructure of concrete elaborated with water cement ratios 0.5 and 0.6 does not show the required quality to ensure proper values of durability and useful life when submitted to corrosivity categories of the atmospheres very high (C5) and extreme (CX) under coastal-industrial atmosphere.

This result, based in the concrete quality assessment is matches with the effective percentages of capillary porosity values (Table 3) determined by capillary flow of water absorption method. Therefore, to concrete quality assessment before submitting to outdoor exposure conditions in Cuba or in other coastal zones of high constructive potential in the world, in addition to compressive strength and ultrasonic pulse velocity testing, capillary flow of water absorption testing is very necessary to carried out.

Capillary pores are uniformly distributed in the hardened cement paste and concrete mass mainly at water cement ratios 0.5 and 0.6 (Figure 11 b and c).

wc 0.4

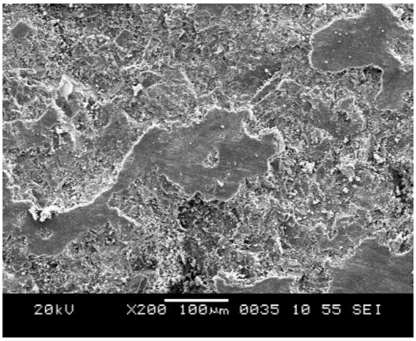

a)

wc 0.5

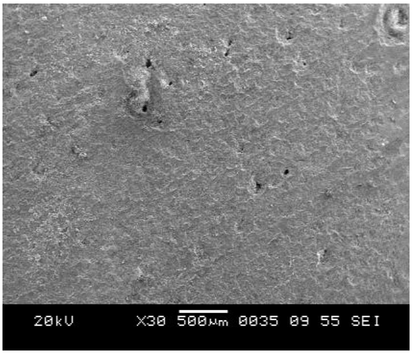

b)

wc 0.6

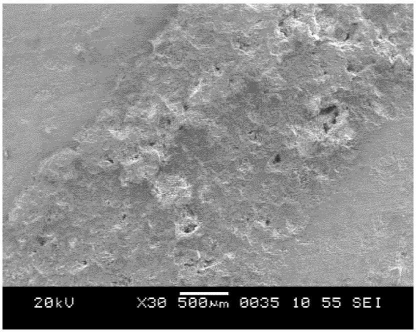

c)

Figure 11. SEM images of the hardened concrete paste samples at different water cement ratios.

CONCLUSION

The following are the most relevant conclusions of this work:

1) Atmospheric corrosion of steel-reinforced concrete can be studied following the methodology established for atmospheric corrosion tests of metallic materials in a coastal city located in a tropical island.
2) Determination of corrosivity categories of the atmosphere of different types of concrete and covering thicknesses showed that it is possible to reduce premature deterioration in structures in conditions of a coastal city located in a tropical island, particularly for structures that are intended to be built in the area closest to the sea without the effect of artificial and natural shielding.
3) Atmospheric corrosion of steel-reinforced concrete increases in the time of exposure. Reinforced concrete with water cement ratios of 0.5 and 0.6 and covering thickness of 20 and 40 mm did not guarantee adequate durability and useful life under corrosivity categories of the atmospheres very high (C5) and extreme (CX) and coastal-industrial atmosphere. It was confirmed with visual observation in reinforced concrete probes, as well as in SEM images of the hardened concrete paste samples at different water cement ratios.
4) According to the behavior of Chloride deposition rate and Sulfur compounds deposition rate at different distances from the sea, Havana City (without shielding conditions) could be considered one of the zones of higher atmospheric corrosivity category in the world.
5) Compressive strength decrease was the factor showing more influence in the atmospheric corrosion of steel reinforced concrete. An effect between compressive strength decrease and total chloride content increase at 20 mm and 40 mm covering depth also influences in the phenomenon.

REFERENCES

[1] Chunhua, L; Weiliang, J. Reinforcement corrosion-induced cover cracking and its time prediction for reinforced concrete structures. *Revista Corrosion Science*., 53, (2011), pp. 1 337–1 347.

[2] Abosrra, L; Ashour, AF; Youseffi, M. Corrosion of steel reinforcement in concrete of different compressive strengths. *Revista Construction and Building Materials*., 25, (2011), pp. 3915–3925.

[3] Luca, B; Matteo, G; Maria-Pia, P. Prevention of steel corrosion in concrete exposed to seawater with submerged sacrificial anodes. *Revista Corrosion Science*., 44, (2002), pp. 1497-1513.

[4] Miranda, J; Gonzáles, JA. Several questions about electrochemical rehabilitations methods for reinforced concrete structure. *Revista Corrosion Science*, 48, (2006), pp. 2172-2188.

[5] Feliu, S; González, JA; Miranda, JM; Feliu, V. Possibilities and problems of in situ techniques for measuring steel corrosion rates in large reinforced concrete structures. *Revista Corrosion Science*, 47, (2005), pp. 217-238.

[6] Abdulrahman, A; Raja, Rizwan H; Rajeh, A; Abdulaziz, A. Investigation of severe corrosion observed at intersection points of steel rebar mesh in reinforced concrete construction. *Revista Construction and Building Materials*., 37, (2012), pp. 67–81.

[7] Pradhan, B; Bhattacharjee, B. Corrosion zones of rebar in chloride contaminated concrete through potentiostatic study in concrete powder solution extracts. *Corrosion Science*., 49, (2007), pp. 3935-3952.

[8] Las pérdidas económicas causadas por el fenómeno de la corrosión atmosférica del acero de refuerzo embebido en el hormigón armado. Resultados preliminares. Abel Castañeda, Manuel Rodríguez. REVISTA CENIC, EBSCO, *CIENCIAS QUÍMICCAS*, Vol. 45, No. 1, pp. 52-59. LA HABANA, CUBA, 2014.

[9] John, A. Mullard1 and Mark G. Stewart2 Life-Cycle Cost Assessment of Maintenance Strategies for RC Structures in Chloride Environments. *JOURNAL OF BRIDGE ENGINEERING* © ASCE/MARCH/APRIL 2012/pp. 353-362.

[10] Silva, MG; Saade, MRM; Gomes, V. Influence of service life, strength and cement type on life cycle environmental performance of concrete. Volume 6, Number 6 .2I013) p. 844-853 • ISSN 1983-4195. *IBRACON STRUCTURES AND MATERIALS JOURNALS*.

[11] Al-Tamimi, AK; Mortula, M; Abu-Lebdeh, G; Beheiry, S. Evaluations of Sustainable Concepts in Civil Engineering Program. The Built & Human Environment Review, Volume 4, Special Issue 1, 2011, pp. 1-12.

[12] Beheshti Nezhad, H; Nariman-Zadeh, N; Ranjbar, MM. Multi Objective Optimization of Concrete Mix Design in Persian Gulf With Gmdh-type

Neural Networks. *2nd International Conference on Engineering Optimization*, September 6 - 9, 2010, Lisbon, Portugal.

[13] Kim, Hong-Sam; Ahn, Tae-Song; Kim, Cheol-Ho; Jeon, Byung-Sub. Quality Control of Chloride Diffusivity of the High Durable Concrete for Approaching Road of Incheon Bridge. *International Commemorative Symposium for the Incheon Bridge,* Korea, 23 Sep., 2009.

[14] Kolluru, V. Subramaniam, Mingdong Bi. Investigation of the local response of the steel–concrete interface for corrosion measurement. *Corrosion Science*, 51, (2009), 1976–1984.

[15] Vedalakshmi, R; Saraswathy, V; Ha-Won Song, N. Palaniswamy. Determination of diffusion coefficient of chloride in concrete using Warburg diffusion coefficient. *Corrosion Science*, 51, (2009), 1299–1307.

[16] Vedalakshmi, R; Manoharan, SP; Ha-Won Song, N. Palaniswamy. Application of harmonic analysis in measuring the corrosion rate of rebar in concrete. *Corrosion Science*, 51, (2009), 2777–2789.

[17] Jaffer, SJ; Hansson, CM. The influence of cracks on chloride-induced corrosion of steel in ordinary Portland cement and high performance concretes submitteded to different loading conditions. *Corrosion Science*., 50, (2008), pp. 3 343-3 355.

[18] Kolluru, V. Subramaniam, Mingdong Bi. Investigation of steel corrosion in cracked concrete: Evaluation of macrocell and microcell rates using Tafel polarization response. *Corrosion Science*, 52, (2010), 2725–2735.

[19] Ghods, P; Isgor, OB; McRae, GA; Gu, GP. Electrochemical investigation of chloride-induced depassivation of black steel rebar under simulated service conditions. *Corrosion Science*, 52, (2010), 1649–1659.

[20] Chunhua, Lu; WeiliangJin, Ronggui Liu. Reinforcement corrosion-induced cover cracking and its time prediction for reinforced concrete structures. *Corrosion Science*, 53, (2011), 1337–1347.

[21] Zhao, Y; Jiang, Y; Weiliang, J. Damage analysis and cracking model of reinforced concrete structures with rebar corrosion. *Corrosion Science*, 53, (2011), pp. 3388-3397.

[22] Zhao, Y; et al., Comparison of uniform and non-uniform corrosion induced damage in reinforced concrete based on a Gaussian description of the corrosion layer. *Corrosion Science*, 53, (2011), pp. 2803–2814.

[23] Wong, HS. *y col*., On the penetration of corrosion products from reinforcing steel into concrete due to chloride-induced corrosion. *Revista Corrosion Science*., 52, (2010), pp. 2469-2480.

[24] Corvo, F; Betancourt, N; Mendoza, A. The influence of airborne salinity on the atmospheric corrosion of steel. *Revista Corrosion Sicience,* 37, (1995), pp. 1889-1901.
[25] Antonio, R Mendoza; Francisco, Corvo. Outdoor and indoor atmospheric corrosion of carbon steel. *Corrosion Science*, 41, (1999), 75-86.
[26] Antonio, R Mendoza; Francisco, Corvo. Outdoor and indoor atmospheric corrosion of no-ferrous metals. *Corrosion Science*, 42, (2000), 1, 143-1 127.
[27] Liboria, Mariaca; Carmina, Menchaca; Estela, Sarmiento; Oscar, Sarmiento; Jose Luis, Ramirez; Jorge, Uruchurtu. Atmospheric Corrosion Dose/Response Functions from Statistical Data Analysis for Different Sites of Mexico. *Innovations in Corrosion and Materials Science*, 2014, 4, 11-20.
[28] Corvo, F; Minotas, J; Delgado, J; Arroyave, C. Changes in atmospheric corrosion rate caused by chloride ions depending on rain regime. *Corrosion Science*, 47, (2005), 883–892.
[29] Cole, IS; Ganther, WD; Furman, SA; Muster, TH; Neufeld, AK. Pitting of zinc: Observations on atmospheric corrosion in tropical countries. *Corrosion Science*, 52, (2010), 848–858.
[30] Nuñez, L; Reguera, E; Corvo, F; González, E; Vazquez, C. Corrosion of copper in seawater and its aerosols in a tropical island, *Corrosión Science*, 47, (2005), 461–484.
[31] Corvo, F; Pérez, T; Dzib, LR; Martín, Y; Castañeda, A; González, E; Pérez, J. Outdoor-Indoor corrosion of metals in tropical coastal atmospheres. *Revista Corrosion Science*., 50, (2008), pp. 220 – 230.
[32] Corvo, F; Pérez, T; Martin, Y; Reyes, J; Dzib, LR; González-Sánchez, J; Castañeda, A. Time of wetness in tropical climate: Considerations on the estimation of TOW according to ISO 9223 standard, *Corrosion Science*., 50, (2008), 206–219.
[33] Morcillo, M; Díaz, I. Marine atmospheric corrosion of carbon steels. *ARTICLE in REVISTA DE METALURGIA*, JUNE 2015.
[34] Natesan, M; Venkatachari, G; Palaniswamy, N. Kinetics of atmospheric corrosion of mild steel, zinc, galvanized iron and aluminium at 10 exposure stations in India. *Corrosion Science*, 48, (2006), 3584–3608.
[35] Yuantai, Ma; Ying, Li; Fuhui, Wang. The atmospheric corrosion kinetics of low carbon steel in a tropical marine environment. *Corrosion Science*, 52, (2010), 1796–1800.

[36] Junhua, Dong; Enhou, Han; Wei, Ke. Introduction to atmospheric corrosion research in China. *Science and Technology of Advanced Materials*, 8, (2007), 559–565.
[37] Yuantai, Ma; Ying, Li; Fuhui, Wang. Corrosion of low carbon steel in atmospheric environments of different chloride content. *Corrosion Science*, 51, (2009), 997–1006.
[38] Farro, NW; Veleva, L; Aguilar, P. Copper Marine Corrosion: I. Corrosion Rates in Atmospheric and Seawater Environments of Peruvian Port. *The Open Corrosion Journal*, 2009, 2, 130-138.
[39] Muthulingam, S; Rao, BN. Non-uniform time-to-corrosion initiation in steel reinforced concrete under chloride environment. *Corrosion Science*, 82, (2014), 304–315.
[40] Trocónis, O. Duracon Collaboration. Durability of concrete structures: DURACON, an iberoamerican project. Preliminary results. *Revista Building and Environment*., 41, (2006), pp. 952–962.
[41] Trocónis, O. Duracon Collaboration. Effect of the marine environment on reinforced concrete durability in Iberoamerican countries: DURACON project/CYTED. *Corrosion Science*., 49, (2007), pp. 2832–2843
[42] American Society of Testing and Materials; Standard test method for determining atmospheric chloride deposition rate by wet candle method, ASTM G-140, Annual Book of ASTM Standard: Philadelphia, 1996.
[43] Meira, GR. y col., Modelling sea-salt transport and deposition in marine atmosphere zone - A tool for corrosion studies. *Revista Corrosion Science*, 50, (2008), 2724–2731.
[44] Corvo, F; Pérez, T; Martin, Y; Reyes, J; Dzib, LR; González, AJ; Castañeda, A. Corrosion Research Frontiers. Atmospheric corrosion in tropical climate. On the concept of Wetness and its interaction with contaminants deposition. Electroanalytical Chemistry: New Research. Nova Science Publishers. Chapter 2. New York. EE. UU. Año 2008.
[45] Corvo, F; Pérez, T; Martin, Y; Reyes, J; Dzib, LR; González-Sánchez, J; Castañeda, A. Atmosphericcorrosion in tropical humidclimates. Environmental Degradation of Infrastructure and Cultural Heritage in Coastal Tropical Climate. *Transworld Research Network*. Kerala, India. Año 2009.
[46] Castañeda, A; Rivero, C; Corvo, F. Evaluación de sistemas de protección contra la corrosión en la rehabilitación de estructuras construidas en sitios de elevada agresividad corrosiva en Cuba. *Revista de la Construcción de Chile*., 11, (2012), pp. 49-61.

[47] Castañeda, A; Corvo, F; Howland, JJ; Pérez, T. Corrosion of steelreinforced concrete in tropical coastal atmosphere of Havana City. *Revista Química Nova*., 36, (2013), pp. 220-229.

[48] Cuban Standard NC 12-01-09: 1988. Determinación del contenido de cloruros en la atmósfera.

[49] ISO 9225:2012. Corrosion of metals and alloys – Corrosivity of atmospheres – Measurement of environmental parameters affecting corrosivity of atmospheres.

[50] Cuban Standard NC 12-01-09: 1989. Determinación de compuestos de azufre en la atmósfera.

[51] ISO 9223:2012. Corrosion of metals and alloys – Corrosivity of atmospheres – Classification determination and estimation.

[52] NC ISO-1920-3 (2010). Norma Cubana. Ensayos de hormigón. Parte 3: Elaboración y curado de probetas para ensayos. La Habana, Cuba.

[53] Norma Cubana NC-724:2009. Ensayos al hormigón. Resistencia del hormigón endurecido.

[54] NC 231 (2002). Determinación, interpretación y aplicación de la velocidad de pulso ultrasónico en el hormigón.

[55] Fagerlund, G. On the Capillarity of Concrete, *Nordic Concrete Research*, No. 1, Oslo, Paper No. 6, 1986.

[56] Troconis de Rincon, O. DURAR Network Members, Manual for Inspecting, Evaluating and Diagnosing Corrosion in Reinforced Concrete Structures. CYTED.ISBN 980-296-541-3 Maracaibo, Venezuela., 1997/ 1998/2001 (1st Edition, 2nd Edition and 3rd Edition in Spanish). 2000 (1st Edition in English).

[57] NC 272 (2003). Norma Cubana. Hormigón endurecido, cemento y áridos. Determinación del cloruro total por valoración potenciométrica, La Habana, Cuba.

[58] ASTM C-1218/M (2008). Standard Test Method for Water-Soluble Chloride in Mortar and Concrete, Barr Harbor Drive, USA.

[59] Natesan, M; Venkatachari, G; Palaniswamy, N. (2005) *Corrosivity and durability maps of India*. Corrosion Prevention and Control. pp. 43-54.

[60] Alcántara, J; Chico, B; Díaz, I; de la Fuente, D; Morcillo, M. Airborne chloride deposit and its effect on marine atmospheric corrosion of mild steel. *Corrosion Science*, 97, (2015), 74–88

[61] Rosa, Vera; Diana, Delgado; Raquel, Araya; Mónica, Puentes. Construcción de Mapas de Corrosión Atmosférica de Chile. Resultados Preliminares. *Rev. LatinAm. Metal. Mat.*, 2012, 32, (2), 269-276

[62] Morcillo, M; Chico, B; De la Fuente, D; Simancas, J. Looking Back on contribution in the field of Atmospheric Corrosion Offered by the MICAT Ibero-American Testing Network, Hindawi Publishing Corporation, *International Journal of Corrosion.*, 2012, (2011), 1-24.
[63] de la Fuente, D; Díaz, I; Simancas, J; Chico, B; Morcillo, M. Long-term atmospheric corrosion of mild steel. *Corrosion Science*, 53, (2011), 604–617.
[64] Feliu, S; Morcillo, M; Chico, B. Effect of distance from sea on atmospheric corrosion rate, *Corrosion*., 55, (1999), 883–891.
[65] Lee, J; Moon, H. Salinity and distributions on seashore concrete structure en Korea, *Building and Environment*., 41, (2006), 1447–1453.
[66] Meira, GR; Padaratz, IJ; Alonso, C; Andrade, C. Efecto de la distancia al mar en la agresividad por cloruros en estructuras de hormigón en la costa brasileña, *Revista Materiales de Construcción*., 271 – 272, (2003), 175 – 189.
[67] Meira, GR; Andrade, MC; Padaratz, IJ; Alonso, MC; Borba, Jr. JC. Measurement and modelling of marine salt transportation and deposition in a tropical region in Brazil, *Atmospheric Environment*., 40, (2006), 5 596–5 607.
[68] Gustafsson, ER; Franzén, G. Island transport of marine aerosol in southern Sweden, *Atmospheric Environment*., 34, (2000), 313-325.
[69] Morcillo, M., Chico, B., Mariaca, M., Otero., E. Salinity in marine atmospheric corrosion: Its dependence on the wind regime existing in the site. *Revista Corrosion Science*, 42, (2000), pp. 91-104.
[70] Zezza, F; Macri, F. Marine aerosol and stone decay, *Science of Total Environment*, 167, (1995), 123–143.
[71] Corvo, F. *y col*. Distribución regional de la salinidad de la atmósfera en Cuba y su influencia sobre la corrosión del acero al carbono. Proceedings. Primer Taller Internacional de Corrosión, CONACYT-CINVESTAV, Mérida, Yucatán, México, 23-28 marzo, 1992.
[72] Corvo, F; Betancourt, N; Díaz, JC; Lariot, C; Leon, Y; Pérez, J; Rodríguez, O; Bricuyet, E; Catala, F; Castro, M; González, R; Echevarria, C; Lorente, M; Ladrón de Guevara, ME. Segunda variante del mapa regional de agresividad corrosiva de la atmósfera de Cuba, in: Proc. Primer Taller Internaciónal de Corrosión, CONACYT-CINVESTAV, Merida, Yucatan, Mexico, 1992.
[73] Morcillo, M; de la Fuente, D; Díaz y H, I. Cano. Atmospheric corrosion of mild steel. *Revista de Metalurgia*, 47 (5) Septiembre-Octubre, 426-444, 2011.

[74] Martín, Y; Ledea, O; Corvo, F; Lariot, C. Indoor atmospheric corrosion of copper and steel under heat trap conditions in Cuban tropical climate Corrosion Engineering, *Science and Technology*, 46, (2011), 624-633.
[75] Corvo, F; Torrens, AD; Martín, Y; González, E; Pérez, J; Valdés, C; Castañeda, A; Portilla, C. Corrosión atmosférica del acero en interiores. Sus particularidades en el clima tropical de Cuba, *Revista de Metalurgia*., 44, (2008), 1-9.
[76] Kenneth Hover, C. The influence of water on the performance of concrete. *Construction and Building Materials*, 25 (2011), 3003–3013.
[77] Hou, W; Liang, C. (1999). Eight-year atmospheric corrosion exposure of steels in China. *Corrosion*, 55, (1), 65–73.
[78] Ismail, M; Muhammad, B; ElGelany Ismail, M. Compressive strength loss and reinforcement degradations of reinforced concrete structure due to long-term exposure. *Construction and Building Materials*, 24, (2010), 898–902.
[79] Rabehi, M; Mezghiche, B; Guettala, S. Correlation between initial absorption of the cover concrete, the compressive strength and carbonation depth. *Construction and Building Materials*, 24 (2010) 898–902. *Construction and Building Materials*, 45, (2013), 123–129.

BIOGRAPHICAL SKETCH

Abel Castañeda Valdés

Affiliation: National Center for Scientific Researches
Education: Chemistry Engineer
Business Address: 25th and 158th avenues, Cast Cubanacan, Municipality Playa, Havana, Cuba.

Research and Professional Experience: He has worked on six research projects, as well as more than 20 technical scientific services related to the specialties of Atmospheric corrosion, Durability of structures in tropical coastal climates and Application of electrochemical techniques in corrosion studies. He has published 15 articles in the web of sciences journals, as well as, others 19 in high international prestige journals.

Professional Appointments: Philosophical Doctor of Technical Sciences, Master in Materials Science and Technology, Assistant Researcher in National

Center for Scientific Researches and Auxiliary Professor of Technological University of Havana.

Honors: Award of the Academy of Sciences of Cuba in two occasions (Years 2009 and 2014), Special distinction of the Minister of Higher Education in Cuba (Year 2008), Provincial Award for Technological Innovation in Cuba (Year 2015), Relevant awards in the Science and Technology forums in Cuba (Year 2015).

Publications from the Last Three Years:

[1] Estudio de la corrosión atmosférica del acero de refuerzo en La Habana, Cuba. REVISTA DE LA CONSTRUCCIÓN DE CHILE. **A. Castañeda**, Juan José Howland Albear, Francisco Corvo, Rigoberto Marrero. Volumen 143. No. 1, pp. 32-40. 2014.

[2] Estudio de la agresividad corrosiva de la atmósfera para el acero de refuerzo embebido en el hormigón armado en La Habana. REVISTA LATINOAMERICANA DE METALURGIA Y MATERIALES. **A. Castañeda**, Juan José Howland Albear, Francisco Corvo, Rigoberto Marrero. Volumen 35. No. 2, pp. 173-188. 2014.

[3] Outdoor-indoor atmospheric corrosion in a coastal wind farm located in a tropical island. REVISTA ENGINEERING JOURNALS. TAILANDIA. Vol. -, No.-.(pruebas de galeras). **A. Castañeda,** F. Corvo, D. Fernández, C. Valdés.

In: Reinforced Concrete
Editor: Sharon Robinson
ISBN: 978-1-53610-752-4

Chapter 5

EXPERTISE OF REINFORCED CONCRETE STRUCTURES BY NON-DESTRUCTIVE METHODS

Malek Jedidi[1,2,*] and Anis Abroug[1]
[1]Institut Supérieur des Etudes Technologiques de Sfax,
Département de Génie Civil, Sfax, Tunisie
[2]Université de Tunis El Manar, Ecole Nationale d'Ingénieurs de Tunis,
Laboratoire de Génie Civil, Tunis, Tunisie

ABSTRACT

The reinforced concrete structures must beings able to absorb the forces applied to them throughout their lives and support the alterations over time and the environment to which they are exposed. In this context, an experimental study was conducted on a public-use building which has structural disorders using non-destructive testing (NDT). The rebound hammer test, the ultrasonic device and the chemical test are used in the field of non-destructive tests to determine respectively the compression strength, the ultrasonic pulse velocity (UPV) and the rebar corrosion in the concrete. Indeed, the test results were analyzed to identify the different disorders in order to offer adequate compensation method and protection against future attacks. Test results have shown that the concrete exhibits good compressive strength. The steel was completely corroded as a result of a chemical attack. The method of jacketing has been proposed for strengthening of building columns.

Keywords: non-destructive testing, diagnosis, repair, rebound hammer test, pulse ultrasonic test, chemical test, jacketing

INTRODUCTION

Nondestructive testing (NDT) is the process of inspecting, testing, or evaluating materials, components or assemblies for discontinuities, or differences in characteristics without destroying the serviceability of the part or system. In other words, when the inspection or test is completed the part can still be used.

These destructive tests are often used to determine the physical properties of materials such as impact resistance, ductility, yield and ultimate tensile strength, fracture toughness and fatigue strength, but discontinuities and differences in material characteristics are more effectively found by NDT.

Strengthening of existing structures has become a major part of the construction activity in many countries. This can be attributed to the problems of concrete structures aging, steel corrosion, variations in temperature, freezing-thawing cycles and exposure to elevated heat (Fukuyama et al. 2000).

The susceptibility of the existing buildings to structural damages largely depends on the quality of design, detailing and construction. The engineer in many cases can extend the life span of a building by utilizing a simple repair or strengthening technique (Frangou et al. 1995). The choice of repairing or strengthening technique becomes therefore the decisive factor as the high cost would prevent many building owners from executing essential repair works (Sheikh 2002; Vandoros and Dritsos 2006).

Non-destructive methods of investigation are used for the control of the size of the members, the establishment of certain characteristics of the concrete (strength, density, module of elasticity, a.o.), verifying the position of the reinforcement and/or the presence of metallic pieces, embedded in the concrete, detection of hidden defects in the concrete or the reinforcement (segregations, cracks, etc.), and for determining the condition and risk of corrosion of the reinforcement embedded into concrete (Sanayei et al. 2012; Almir and Protasio 2000; Rens and Kim 2007; Jedidi and Machta 2014; Dias and Jayanandana 2003).

When making a diagnosis concerning intervention measures for the rehabilitation of the structures exposed to aggressive environments, one must consider not only the effect on the building materials, but also the on the broader issues of design and execution of intervention works for different categories of structures (Kamal and Boulfiza 2011; Shiotani et al. 2009; Terzic and Pavlovic 2010; Shah and Hirose 2010; Ervin et al. 2009).

This paper presents state-of-the-art non-destructive methods for the diagnostic testing of building structures and examples of their application. Jacketing of the columns is the method of repair and reinforcement which was chosen based on the nature and degree of importance of disorders recorded during diagnosis.

NDT METHODS

Figure 1 shows a proposal of general division of the non-destructive test methods useful in assessing the durability of structures made of concrete. The classification is based on (ACI 1998;Bungey et al. 2006; Carino 1999; Davis 2003; Drobiec 2010).

1. Investigation of the Reinforced Concrete Structures

The investigation of the damage state of the structure in service is made by means of the following investigation methods:

- The visual examination;
- The use of non-destructive testing methods;
- The use of methods that require the taking of samples, but which do not endanger the service safety of the structure.

The visual examination of the state of the structure, and of the anticorrosive protection applied on their surfaces, includes: the appreciation of aspect changes of the concrete and the reinforcement surfaces; the presence of degradation due to corrosion; the evaluation of the changes in condition of the anticorrosive protection. The results of the visual examination are registered in the form of surveys of degradations on the lay-outs and sections of the construction, with details on the investigated members, indicating their position and the extent of the damage, in order to provide their identification on the structure.

A detailed list of equipment is necessary to perform a visual examination. Depending on the structures this list may be supplemented, but also reduced.

The most important equipment for measurements are: double meter stencil to cracks, graduated magnifying glass, etc. and for document auscultation: record, writing materials including marking chalk, camera flash, etc.

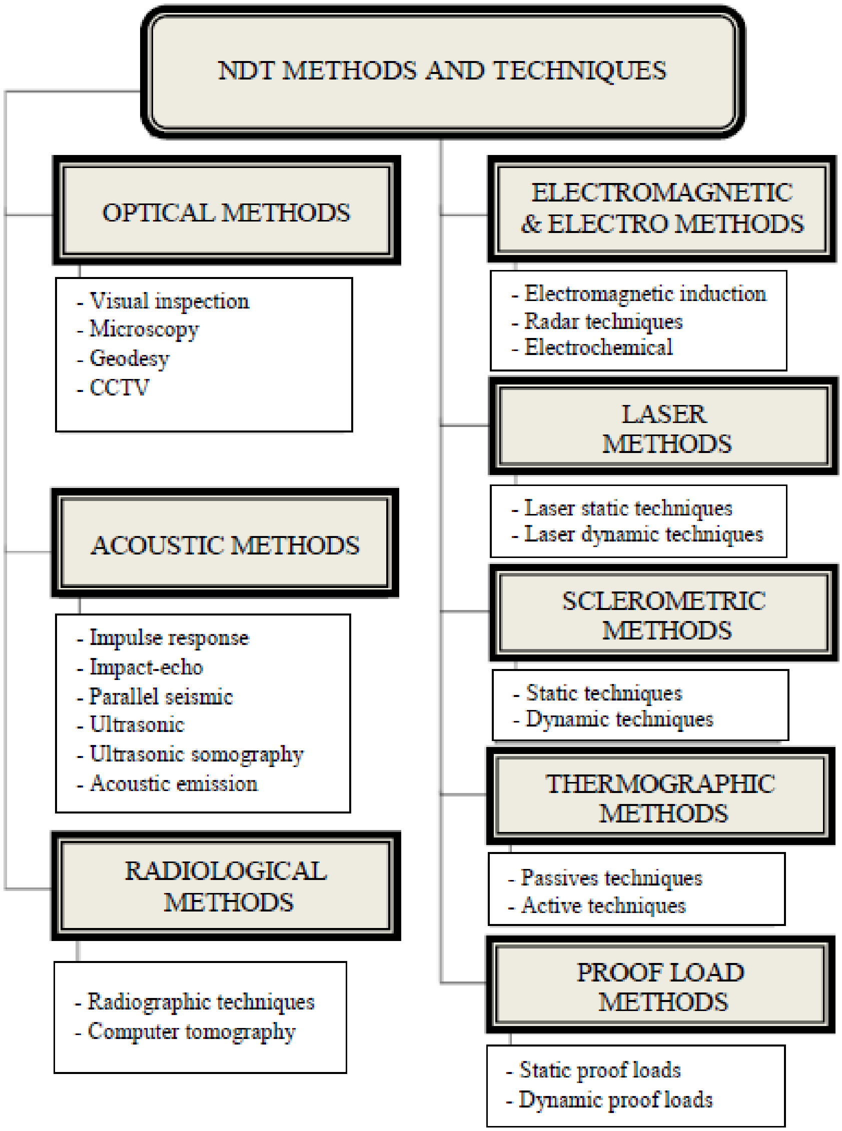

Figure 1. Non-destructive methods for diagnostic testing of building structures.

2. Diagnosis of the Reinforced Concrete Structures

The diagnosis is the result of investigation and represents the basis for adopting intervention measures.The diagnosis concerns first evaluation of the damage state induced by corrosion, specific to the analysed environments, and second, the initial defects and the degradations induced by other causes.

The main steps which lead to the establishment of a diagnosis are:

1) The preliminary examination of the construction and its project, consisting mainly of the visual analysis of the bearing members of the construction and the engineer evaluation of their state in the context of the knowledge of their general structural construction. As result of the preliminary examination conclusions can be drawn up for temporary measures, in order to prevent imminent or potential accidents.
2) The detailed investigation by means of measurements and both in situ and laboratory tests, aimed to point out: defects and damages, other than the ones induced by corrosion, with an explanation of their causes; defects of the technological installations, which are one of the major causes of corrosion induced degradations; other defects, on ventilation, exhaust and waste water sewage equipment, waterproofing.
3) Data processing and analysis of the safety degree of the construction by interpreting the data, estimation of loads on the service time of the construction.
4) The establishment of the diagnosis and proposals concerning intervention measures.

All the information above concerning the investigation, analysis and diagnosis will be centralized in a written report drawn up by the experts who performed these activities.

TEST PROCEDURES

1. Schmidt Rebound Hammer Test

The Schmidt rebound hammer is principally a surface hardness tester. It works on the principle that the rebound of an elastic mass depends on the hardness of the surface against which the mass impinges. There is little apparent theoretical relationship between the strength of concrete and the rebound number RN of the hammer (Figure 2).

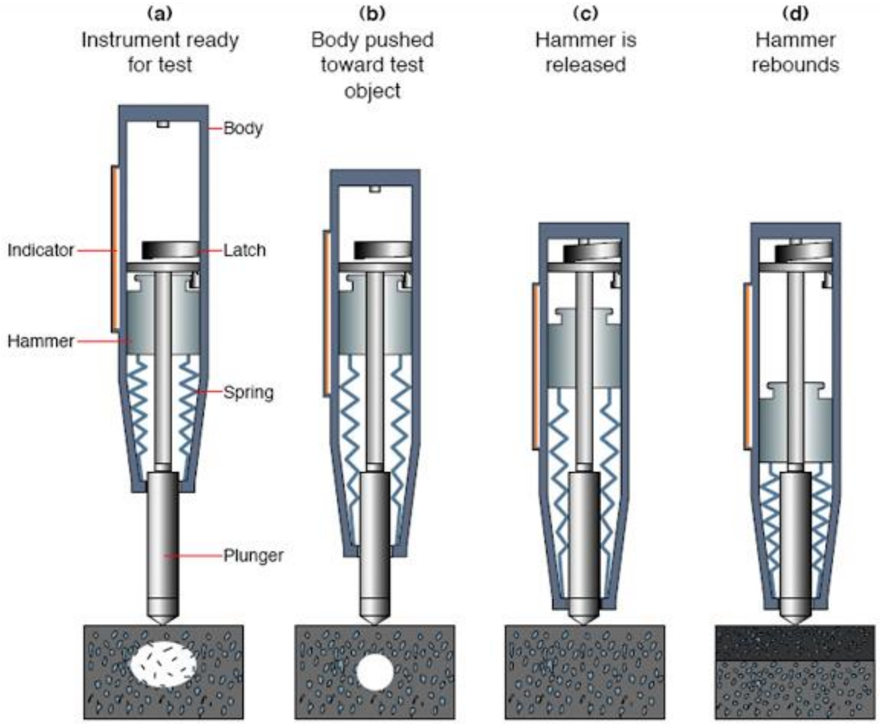

Figure 2. Principal schema of Schmidt rebound hammer.

This test was performed on the specimens according to standards EN 12504-2 (EN 12504-2 2001) and EN 12309-3 (EN 12309-3 2003). Schmidt rebound hammer test gave values of RN. The compressive strength of the concrete was derived using the chart provided with the device (Aydin and Saribiyik 2010). No action has been located within 40 mm of the flat faces of the specimen. The hammer has to be used against a smooth surface, preferably a formed one. Open textured concrete cannot therefore be tested. If the surface is rough, e.g., a trowelled surface, it should be rubbed smooth with a carborundum stone. RN was equal to the median of 27 measures spread over the three generators of the specimen tested (Figure 3).

a

b

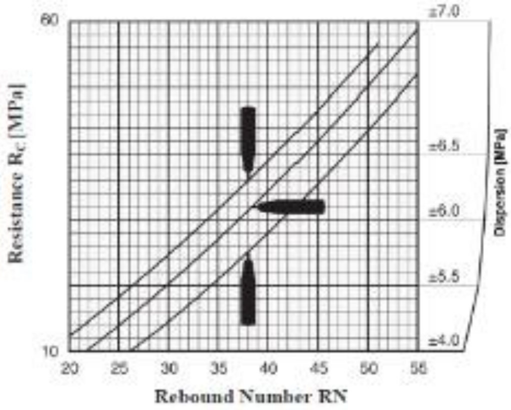

c

Figure 3. Schmidt rebound hammer test. (a) Schmidt rebound hammer, (b) Carborundum stone, (c) Chart for determining the resistance as a function of RN.

2. Pulse Velocity Test

The equipment consists essentially of an electrical pulse generator, a pair of transducers, an amplifier and an electronic timing device for measuring the time interval between the initiation of a pulse generated at the transmitting transducer and its arrival at the receiving transducer (Figure 4).

Figure 4. Ultrasonic pulse velocity tester with microprocessor.

The pulse velocity test was determined in accordance with the requirements of EN 12504-4. The device used was an electronic tester with microprocessor in a portable case. It is capable of measuring transit time over path lengths ranging from about 100 mm to the maximum thickness to be inspected to an accuracy of ±1%. The transducers used were in the range of 50 to 60 kHz. Calibration using a calibration bar (known in time course) was carried out before the measurements and after an hour of use as recommended by the manufacturer.

A pulse of longitudinal vibrations is produced by an electro-acoustical transducer, which is held in contact with one surface of the concrete under test. When the pulse generated is transmitted into the concrete from the transducer using a liquid coupling material such as grease or cellulose paste, it undergoes multiple reflections at the boundaries of the different material phases within the concrete. A complex system of stress waves develops, which includes both longitudinal and shear waves and propagates through the concrete. The first waves to reach the receiving transducer are the longitudinal waves, which are converted into an electrical signal by a second transducer. Electronic timing circuits enable the transit time T of the pulse to be measured. Longitudinal ultrasonic pulse velocity is given by:

$$UPV = \frac{L}{T} \tag{1}$$

where, L is the distance between two probes and T is the time required to travel the distance between two transducers.

Pulse velocity measurements made on concrete structures may be used by placing the two transducers on either (Figure 5):

- Opposite faces (direct transmission);
- Adjacent faces (semi-direct transmission); or
- The same face (indirect or surface transmission).

Since the maximum pulse velocity is transmitted at right angles to the face of the transmitter, the direct method is the most reliable one from the point of view of transit time measurement. Also, the path is clearly defined and can be measured accurately, and this approach should be used wherever possible for assessing concrete quality.

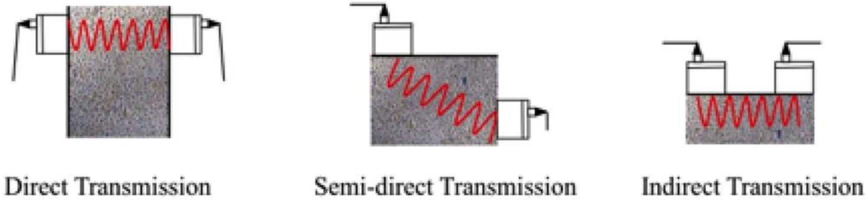

Figure 5. Ultrasonic pulse velocity test methods.

3. Chemical Analysis

Reinforcing steel bars embedded in concrete depassivate when a certain amount of chlorides is built up in their surrounding, being the risk for reinforcement corrosion related to the chloride content in the concrete. Therefore, reliable chloride analysis in hardened concrete becomes a key parameter in the evaluation of existing structures and in the prediction of future service life. Drill dust samples are collected from various pre-determined points in the structure, generally from different depths, for chloride content determination. The samples are investigated in a laboratory to determine the chloride content in accordance with theEN 14629 standard (EN 14629 2007)using the chemical analysis apparatus.

EXPERIMENTAL RESULTS AND DISCUSSION

1. Compressive Strength

Table 1 gives the results of the compressive strength (Rc) measurements determined by the rebound hammer test on the first meters of the columns, stringers and soles witch exhibit some cracks and corrosion. According to the calculations of reinforced concrete, the minimum acceptable value of the compressive strength of concrete is 22 MPa. According to the results of the table 1, we note low values of the Rc for the columns (Rc = 17.7 MPa), but acceptable results for stringers and soles (respectively 22.8MPa and 22.2MPa). The outer surfaces of the stringers and soles do not show cracks or deterioration. Indeed, during the foundation work, the company has used a mix concrete with HRS cement, which has better resistance to aggressive agents and chemical attacks such as chloride and using a greater coating distance equal to 4 cm.

Table 1. Rc of the columns, stringers and soles

Tested element	Columns	Stringers	Soles
1	17.3	22.7	22.5
2	18.1	22.5	22.3
3	17.7	23.2	21.8
Mean value (MPa)	17.7	22.8	22.2

2. Pulse Velocity Test

The object of this method is basically to measure the velocity of the pulses of longitudinal waves passing through concrete. The velocity of an ultrasonic pulse is influenced by the properties of concrete which determine its elastic stiffness and mechanical strength. Thus the variations in the pulse velocity values reflect a corresponding variation in the state of concrete under test. There is a reduction in the pulse velocity if the concrete under test has low compaction, voids or damaged material. The pulse velocity increases or decreases as the concrete matures or deteriorates or changes with time. Table 2 gives the concrete quality accordingly to pulse velocity.

Table 2. Concrete quality accordingly to pulse velocity

UPV (m/s)	Concrete quality garding
Above 4500	Excellent
3500 to 4500	Good
3000 to 3500	Medium
Below 3000	Doubtful

The results of Table 3 show the ultrasonic pulse velocity values (UPV value) for some RC columns of the structure. It can be observed that the values are between 3000 m/s and 3500 m/s. However, based on the pulse velocity values and Table 2, the columns present a medium quality of concrete.

Table 3. UPV values of the RC columns

Columns	L (m)	T (s)	UPV (m/s)
C1	0.30	$9.15\ 10^{-5}$	3280
C2	0.30	$8.80\ 10^{-5}$	3410
C3	0.30	$8.95\ 10^{-5}$	3350
C4	0.30	$8.85\ 10^{-5}$	3390
C5	0.30	$9.40\ 10^{-5}$	3190

3. Chemical Analysis

Table 4 gives the values of the chemical analysis of concrete relative to the cement mass. It is recommended that average values of chloride ion diffusion coefficient are calculated from three specimens. The concrete was wet and oxygenated; the allowable threshold corresponds very roughly to a rate of 0.40% compared to the weight of cement. The result of the chemical analysis of the specimens gives a rate of 0.90% of chloride contents which is well above the permitted level.

Table 4. Result of the chemical analysis

Specimens	Chloride contents (%)
1	0.90
2	0.92
3	0.88
Average value	0.90

Chloride attack or chloride induced rebar corrosion is a process that aims the steel on the concrete composite. This could lead the reduction of tensile strength, aesthetic defects; also, it could create moisture, oxides points that could accelerate the corrosion.The chloride could penetrate through the concrete until rebar bars by pore spaces and micro cracks (Shi 2012). The sources of chlorides is vast, this could be derivate of paste composition, sea environments and contaminated aggregates (Broomfield 1997). The mechanism consists of chlorine ions breaking the passive layer and corroding the mild steel in pitting form.

On the other hand, water infiltration from the drain of waste water under the building was detected. The corrosion of steel in contact with concrete is a problem that should be avoided.Concrete is a porous material with high concentration of soluble calcium, sodium and potassium.These elements, in presence of water, form hydroxides, responsible for maintaining the pH of the area in around 12. In this situation, a passive layer is formed in the steel. It consists of a dense and impenetrable thin film, which protects the steel from further corrosion.

Table 5 gives the values of the chemical analysis of water sample. The results have shown that it is acid waste water as the pH varies from 4 to 5.

Table 5. Result of the chemical analysis of water

	Water sample
PH	4 – 5

Repair of Concrete Elements in the Structure

The intervention measures on the bearing structure of the construction are proposed in correlation to the nature and degree of the damage, presented by the members of the investigated construction.

In our case the diagnosis of the building, we opted for jacketing of the columns because the building is in operation at the floor. Moreover, the mechanical characteristics of the structural elements must be improved so that they provide better strength serviceable and ultimate resistance state. The jacketing process could start by the following steps:

1) Adding steel connectors into the existing column in order to fasten the new stirrups of the jacket in both the vertical and horizontal directions at spaces not more than 50cm.Those connectors are added into the column by making holes 3-4mm larger than the diameter of the used steel connectors and 10-15cm depth.
2) Filling the holes with an appropriate epoxy material then inserting the connectors into the holes.
3) Adding vertical steel connectors to fasten the vertical steel bars of the jacket following the same procedure in step 1 and 2.
4) Installing the new vertical steel bars and stirrups of the jacket according to the designed dimensions and diameters.
5) Coating the existing column with an appropriate epoxy material that would guarantee the bond between the old and new concrete.
6) Pouring the concrete of the jacket before the epoxy material dries. The concrete used should be of low shrinkage and consists of small aggregates, sand, cement and additional materials to prevent shrinkage.

The previous steps are illustrated inFigure 6.

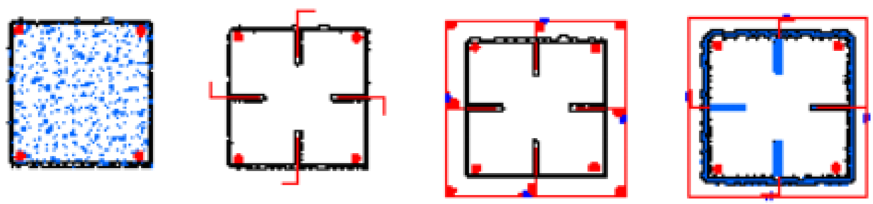

Step 1	**Step 2**	**Step 3**	**Step 4**
Cleaning and roughening the surface	Installing dowels for fastening the stirrups	Installing the new stirrups and steel bars	Coating the surface with epoxy

Figure 6. The jacketing process of column.

It is noted that the strengthening of an element by increasing its concrete section (Figure 7) directly influences the mass of the structure compared to other means of reinforcements, which are characterized by their relative lightness. That is why the structure of the soles was checked and jacketing has been achieved.

Figure 7. Increasing the section of column by reinforced concrete jacketing.

CONCLUSION

The present paper has presented results of an experimental study conducted on a public-use building having disorders located in Sfax, south of Tunisia. The investigation used non-destructive testing (NDT) to determine respectively the compression strength and the rebar corrosion in the concrete. The test results were analyzed to identify the different disorders in the construction. The following conclusions have been drawn from the investigation:

1) The visual inspection of the state of the structure was performed to quickly assess the damage and determine the appropriate way of expedient examinations.
2) The results of the visual inspection were registered in the form of surveys of degradations on the lay-outs and sections of the construction, with details on the investigated members, indicating their position and the extent of the damage, in order to provide their identification on the structure.
3) The results of the measurements determined by the rebound hammer test showed low compressive strength values for columns (RC = 17.7 MPa) but acceptable values for stringers and soles (respectively 22.8MPa and 22.2MPa).

4) The ultrasonic pulse velocity values (UPV value) for some RC columns of the structure showed that the columns present a medium quality of concrete.
5) The result of the chemical analysis of the concrete specimens gave a rate of 0.90% of chloride contents which is well above the permitted level. The steel was completely corroded as a result of chemical attack.
6) The jacketing techniques was used to improve the mechanical characteristics of the structural elements in order to provide better strength serviceable and ultimate resistance state.

REFERENCES

Almir, P. F. and Protasio, F. C. (2000). "Application of NDT to concrete strength estimation,"*NDT.Net*, vol. 5, no. 2, pp. 1–6.

American Concrete Institute Report ACI 228.2R-98. (1998). Non-destructive test methods for evaluation of concrete in structures, *ACI.* Farmington Hills, Michigan.

Aydin, F., and Saribiyik, M. (2010). "Correlation between Schmidt hammer and destructive compressions testing for concretes in existing buildings." *Sci. Res. Essays,* 5, 1644-1648.

Broomfield, J. P. (1997). Corrosion of steel in concrete: understanding, investigation, and repair, *E & FN Spon,* New York; London.

Bungey, J., Millard, S., Gratham, M. (2006). Testing of concrete in structures, Taylor & Francis, London and New York.

Carino, N. J. (1999). Nondestructive test methods, *Concrete Construction Engineering Handbook,* CRC Press.

Davis, A. G. (2003). The non-destructive impulse response test in North America: 1985–2001, NDT&E International, Vol. 36.

Dias, W. P. S. and Jayanandana, A. D. C. (2003). "Condition assessment of a deteriorated cement works," *Journal of Performance of Constructed Facilities,* vol. 17, no. 4, pp. 188–195.

Drobiec, Ł., Jasiński, R., and Piekarczyk, A. (2010). Diagnostic testing of reinforced concrete structures. Methodology, field tests, laboratory tests of concrete and steel (in Polish), Wydawnictwo Naukowe PWN, Warsaw, Vol. 1.

EN 12309-3. (2003).Testing hardened concrete — Part 3: Compressive strength of test specimens.

EN 12504-2. (2012). Testing concrete in structures. Non-destructive testing. Determination of rebound number.

EN 14629. (2007). Products and systems for the protection and repair of concrete structures. Test methods. Determination of chloride content in hardened concrete.

Ervin, B. L., Kuchama, D. A., Bernhard, J. T. and Reis, H. (2009). “Monitoring corrosion of rebar embedded in mortar using high frequency guided ultrasonic waves,” *Journal of Engineering Mechanics*, vol. 135, no. 1, pp. 9–18.

Frangou, M., Pilakoutas, K., and Dritsos, S. (1995). Structural repair/ strengthening of RC columns, *Construction and Building Materials*, Vol. 9, No. 5, pp. 259-266.

Fukuyama, K., Higashibata, Y., and Miyauchi, Y. (2000). Studies on repair and strengthening methods of damaged reinforced concrete columns,‖ *Cement and Concrete Composites* 22, pp. 81-88.

Jedidi, M. and Machta, K. (2014). “Destructive and Non-destructive Testing of Concrete Structures,” Jordan Journal of Civil Engineering, Vol. 8, no. 4, pp; 432-441.

Kamal, A. S. M. and Boulfiza, M. (2011). “Durability of GFRP Rebars in simulated concrete solutions under accelerated aging conditions,” *Journal of Composites for Construction*, vol. 15, no. 4, pp. 473–481.

Rens, K. L. and Kim, T. (2007); “Inspection of Quebec street bridge in Denver, Colardo: destructive and nondestructive testing,” *Journal of Performance of Constructed Facilities*, vol. 21, no. 3, pp. 215–224.

Sanayei, M., Phelps, J. E., Sipple, J. D., Bell, E. S., and Brenner, B. R. (2012). “Instrumentation, nondestructive testing, and finite element model updating for bridge evaluation using strain measurements*,” Journal of Bridge Engineering*, vol. 17, no. 1, pp. 130–138.

Shah, A. A. and Hirose, S. (2010). “Nonlinear ultrasonic investigation of concrete damaged under uniaxial compression step loading,” *Journal of Materials in Civil Engineering*, vol. 22, no. 5, Article ID 007005QMT, pp. 476–483.

Sheikh, S. A. (2002). Performance of concrete structures retrofitted with fibre reinforced polymers, *Engineering Structures* 24 pp. 869-879.

Shi, X., Xie, N., Fortune, K. and Gong, J. (2012). “Durability of steel reinforced concrete in chloride environments: An overview,” *Construction and Building Materials*, vol. 30, no. 1, pp. 125-138.

Shiotani, T., Aggelis, D. G. and Makishima, O. (2009). “Global monitoring of large concrete structures using acoustic emission and ultrasonic techniques: case study," *Journal of Bridge Engineering*, vol. 14, no. 3, pp. 188–192.

Terzic, A. M. and Pavlovic, L. M. (2010). "Application of results of nondestructive testing methods in the investigation of microstructure of refractory concretes," *Journal of Materials in Civil Engineering,* vol. 22, no. 9, pp. 853–857.

Vandoros, K. J., and Dritsos, S. E. (2006).Concrete jacket construction detail effectiveness when strengthening RC columns, *Construction and Building Materials,* doi:10.1016/j.conbuildmat.2006.08.019.

INDEX

D

E

F

G

H

I

J

K

L

M

N

O

P

R

S

T

U

V

W

Y

Z